APPENDIX D

DETAILS OF CASK RESPONSE TO FIRE ACCIDENTS

D.1 Introduction

For this study, researchers performed thermal analyses of Rail-Steel, Rail-Lead, and Truck-DU cask types to obtain the thermal response of these casks to the fire accident scenarios described in Chapter 4. The approach used to model these casks is similar to the ones used in the following:

- HI-STAR 100, NAC-STC, and GA-4 safety analysis reports (SARs) (Holtec International, 2000; NAC International, 2004, General Atomics, 1998)
- a combination of one-dimensional thermal resistance analysis (Incropera and Dewitt, 1996)
- two- and three-dimensional finite element modeling

Thermal resistances are used to obtain effective thermal properties for several geometrically complex regions of the casks. These homogenized regions are then added back to the finite element model with the equivalent effective properties. This process eliminated some of the finite element discretization complexities inherent in the models, while at the same time it kept the essential thermal response of the casks.

For the Rail-Steel and Truck-DU casks, thermal resistance analysis reported in the Rail-Steel cask SAR (Holtec International, 2000) and in the Truck-DU cask SAR (General Atomic, 1998), respectively, are used but modified where necessary to reflect the current study. This appendix discusses these modification in more detail in later sections. The approach used to model the Rail-Lead cask is similar to the approach used in the Rail-Lead cask SAR (NAC International, 2004). The only exception is in how the contents of the cask are modeled. In the Rail-Lead cask SAR, the fuel-basket region and the rest of the overpack are modeled explicitly using a three-dimensional, quarter section of the cask to obtain a steady-state solution. The maximum temperature difference between the center of the fuel-basket region and the inner wall of the overpack obtained in the steady-state solution is then used to calculate the fuel-basket cladding temperature for the regulatory uniform heating flux (see Title 10 of the *Code of Federal Regulations* (10 CFR) 71.73, "Hypothetical Accident Conditions"), which did not include a fuel-basket region.

In this study, a three-dimensional, quarter section of the fuel basket is used to obtain effective thermal properties for the Rail-Lead cask and fuel basket. The fuel-basket region is replaced in the full-scale, three-dimensional finite element model using effective properties for the homogenized basket region. With the exception of the fuel basket region, results in the Rail-Lead cask SAR are used to obtain the thermal response of this cask, with minor changes to reflect the current study. Results taken from the Rail-Steel and Rail-Lead cask SARs and from the Truck-DU cask SAR are checked where possible using formulas taken directly from these reports or using formulas derived from independent analysis.

Some boundary conditions and material properties differ slightly from those used in the Rail-Steel and Rail-Lead cask SARs and in the Truck-DU cask SAR. The intent of this thermal analysis is to determine the temperature of critical components during and after a hypothetical fire accident using material properties and boundary conditions that closely resemble the conditions in a real fire accident. Since actual boundary conditions related to a severe fire are

sometimes difficult to implement using available data or current analysis tools, researchers had to make some simplifications. For example, they assumed the insulation material used in the neutron shields of both casks decomposes completely when its operational temperature limit is reached. In such cases, researchers made conservative assumptions to maximize heat input to the casks, as is done in both SARs cited above. In the case of material properties, those presented in the SARs are preferred, followed by those in standard thermal textbooks and journals. For some materials, properties are available, but only over a limited temperature range. In such cases, the value available at the highest temperature is used for higher temperatures.

As mentioned in Chapter 4, MSC Software Corporation's (MSC's) Patran/Thermal (P/Thermal) (MSC Software Corporation, 2008) is the finite element heat transfer code used to solve the internal thermal response of the Rail-Steel and Rail-Lead casks in the regulatory uniform heating scenario. This scenario effectively simulates fire conditions using a spatially uniform radiation flux over the external surfaces of the casks as established in 10 CFR 71.73. The container analysis fire environment (CAFE) is the computational fluid dynamics code used to generate the fire environment for the CAFE regulatory and CAFE nonregulatory scenarios described in Chapter 4. For these scenarios, CAFE and P/Thermal are coupled together to obtain the thermal response of the Rail-Steel and Rail-Lead casks. CAFE generates more realistic fire conditions on the external surfaces of the casks, as opposed to spatially uniform heating conditions. P/Thermal uses CAFE-predicted, external conditions to calculate the internal thermal response of the casks.

Researchers analyzed three fire accident scenarios different from the hypothetical accident condition (HAC) regulatory fire configuration for the rail casks and one fire accident scenario—the most severe configuration of the rail cask analysis—for the truck cask with a fire lasting 1 hour, as described in Chapter 4. These scenarios represent the accident case in which the fuel pool and the cask are concentric with each other (fully engulfing) or separated by one railcar width or one railcar length.

In the following sections, the geometry, material properties, and boundary conditions used to model the Rail-Steel, Rail-Lead, and Truck-DU casks are described and results are shown that supplement discussions in Chapter 4. The three-dimensional domain and the boundary conditions used in the CAFE runs are described first, followed by the geometry and boundary conditions used in the Rail-Steel and Rail-Lead cask analyses utilizing the P/Thermal finite element models. Finally, this report presents and discusses the results from two CAFE runs used to benchmark the code to demonstrate the validity of the CAFE code for these types of analyses.

D.2 Container Analysis Fire Environment Finite Volume Domain and Boundary Conditions

CAFE (Suo-Antilla et al., 2005) uses the finite volume approach with orthogonal Cartesian discretization to solve (1) the three momentum equations for predicting the velocity and momentum field, (2) the mass continuity equation, (3) the energy equation for predicting the temperature field, (4) the equation of state, (5) a number of scalar transport equations for tracking the flow of species, and (6) two transport equations to solve thermal radiation within and external to the fire. CAFE uses a variable density algorithm (pressure implicit, split operator) to obtain a velocity field that satisfies both the momentum and continuity equations. CAFE has a

number of turbulence models, but for this study a large eddy simulation formulation is used. Thermal radiation transport within and near the fires is split into two types: diffusive radiation inside the flame zone and clear air radiation outside the flame zone. Diffusive thermal radiation transport is modeled with the Rosseland approximation. Clear air radiation outside the flame zone is modeled using view factor methods.

CAFE is coupled to P/Thermal through a set of user-supplied subroutines that pass temperature and thermal heat flux data between both codes. CAFE uses a specialized scheme to map the temperature and heat fluxes to the exterior surfaces of the finite element model (Suo-Antilla et al., 2005). MSC Patran is the front-end code employed to generate the material database, the finite element discretization, and the boundary conditions used by P/Thermal. It is through a special boundary condition, set up in Patran, that CAFE and P/Thermal are able to exchange data.

Figure D-1 illustrates the domain configurations used in the CAFE fire scenarios discussed in Chapter 4. Figure D-1 (a) shows the computational fluid dynamics domain used for the CAFE regulatory run, and Figures D-1 (b) through D-1 (d) show the domain for the CAFE nonregulatory runs. As explained in Chapter 4, all nonregulatory CAFE runs for rail casks were determined based on a 113,562-liter (30,000-gallon (gal)) fuel spill. A rectangular pool is used to ensure that the specifications from 10 CFR 71.73 are met in the case of regulatory fires. For consistency, the pool remained rectangular in all other cases. The pool edges remained 3 meters (m) (9.8 feet) away from the surface of the cask in all configurations.

The pool area is 9.25×13.80 m (30.35×45.28 feet) in the Rail-Steel cask configurations, and 9.14×12.42 m (29.99×40.75 feet) in the Rail-Lead cask configurations. These pool areas correspond to a fully loaded rail tank car burning over a period of 3 hours, the maximum burn time based on 113.6 cubic meters (m^3) (30,000 gal) of fuel.

The pool area is 8.3×12 m (27.2×39.3 feet) in the Truck-DU cask configuration. This area corresponds to a fully loaded fuel tanker truck burning over a period of 1 hour, the maximum burn time based on 34.1 m^3 (9,000 gal) of fuel. Only the scenario depicted in Figure D-1 (b), the most severe fire scenario in the analysis of the rail casks, was analyzed for the Truck-DU cask.

An appropriate domain size is determined from del Valle et al. (2007) and del Valle (2009), in which thermal analyses were conducted with CAFE using a calorimeter the size of a rail cask. In these studies, results of CAFE runs were compared to experiments and showed good agreement. In the current study, the ground dimensions varied between cases since a larger domain is required for the cask offset cases, but they were at least 25×15×25 m (82×49×82 feet), about the size of the domain used in del Valle et. al. (2007) and del Valle (2009). A mesh refinement study was conducted to assess the sensitivity of the cask external temperatures to mesh size and to determine an appropriate mesh size. Based on this study, a mesh with approximately 90,000 finite volumes was deemed acceptable for both casks. As observed in Figure D-1, the mesh is finer in the region near the pool. All CAFE scenarios used calm wind conditions; the velocity at the boundaries and inside the domain are originally set to zero, but are allowed to float as the fire develops.

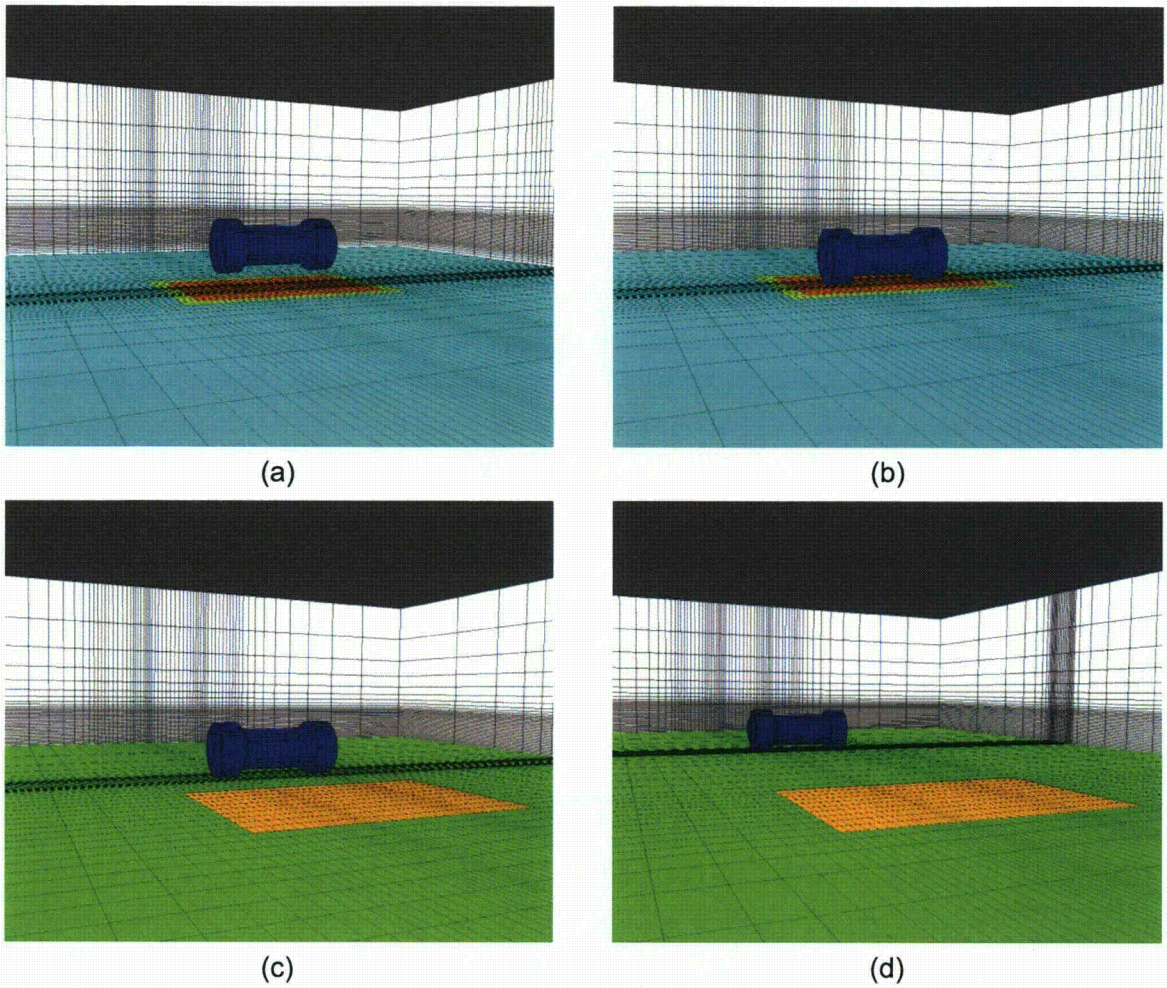

Figure D-1 CAFE three-dimensional domain: (a) CAFE regulatory fire, (b) cask on ground and at the center of the pool, (c) cask on the ground and 3 m (10 feet) from the edge of the pool, and (d) cask on the ground and 18.3 m (60 feet) from the edge of the pool

D.3 The Rail-Steel Cask

The Rail-Steel cask is designed for transportation of a variety of spent fuel assemblies and is intended to fit horizontally on a railcar bed (see Figure D-2). Therefore, the Rail-Steel cask system is assumed to be in the horizontal position in all CAFE runs (see Figure D-1), as it would be after derailment if the flatbed railcar overturned or if the cask detached from a railcar after an accident. This thermal analysis only considers the thermally relevant components of the Rail-Steel cask. As stated in the introduction, this analysis uses some results reported in the Rail-Steel cask SAR (Holtec International, 2000). Values taken from the SAR were checked where possible to assess validity of assumptions and to verify results.

D.3.1 Geometric Consideration

The Rail-Steel cask consists of an overpack, a multipurpose canister (MPC), and two impact limiters; these components fit together as shown in Figure D-3. The MPC stores the nuclear spent fuel material, and the lid is seal welded to prevent the contents from leaking into the overpack cavity. The MPC is the first containment barrier in the Rail-Steel cask. The overpack is designed to temper both the heat and the neutron and gamma rays generated inside the MPC. The overpack is secured with a seal to prevent the contents from a breached canister from further leaking into the external environment. Thus, the overpack forms the second containment barrier in the Rail-Steel cask. During transportation, the overpack ends are fitted with impact limiters that, besides absorbing most of the impact energy during an impact, add another thermal insulation layer to the extreme ends of the overpack.

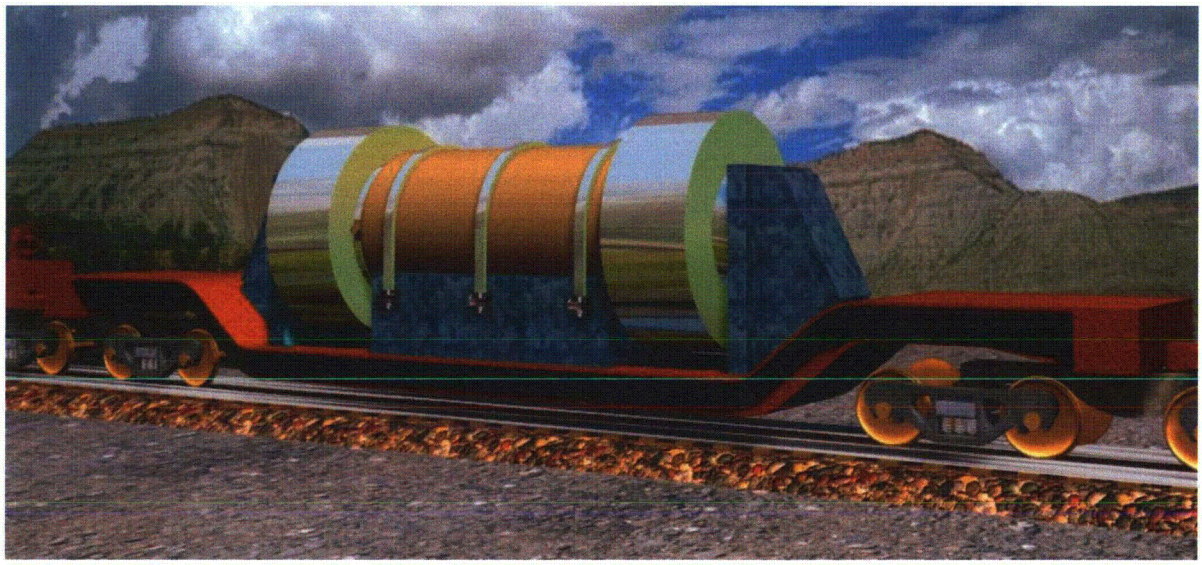

Figure D-2 Rail-Steel cask transportation system

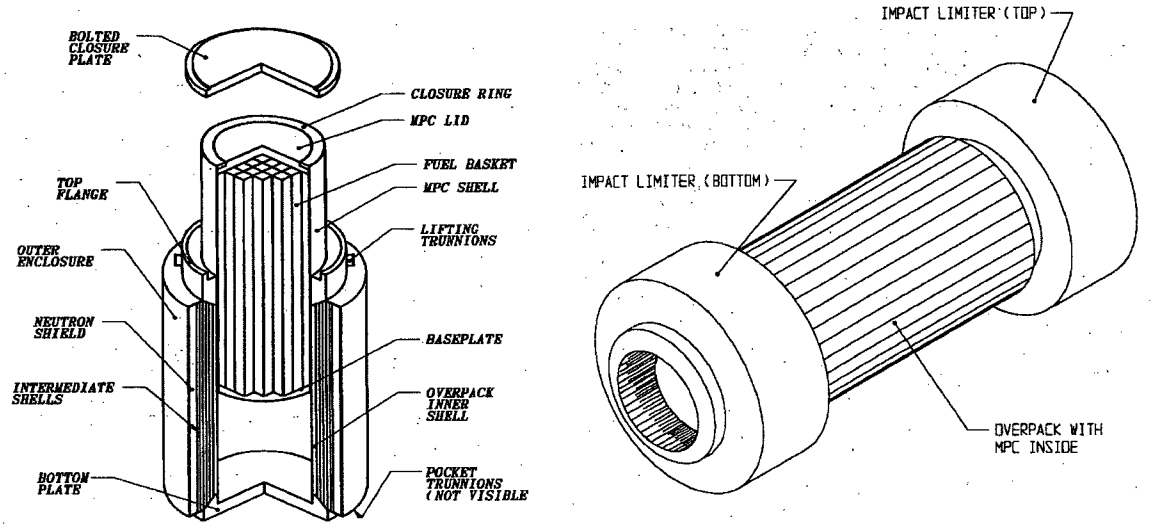

Figure D-3 Rail-Steel cask: (a) assembly of MPC and overpack and (b) cask with limiters (from Holtec International, 2000)

D.3.1.1 The Overpack

The Rail-Steel overpack is a multilayered cylindrical vessel approximately 2.11 m (83.3 inches (in.)) in diameter and 5.16 m (203.1 in.) in length. The inner cavity of the overpack is approximately 1.75 m (64.7 in.) in diameter and 4.85 m (191.1 in.) in length. The inner cavity is formed by (1) welding a thick wall cylinder, called the inner shell, to a metal base cup at the bottom and to a large diameter flange at the top and (2) bolting a closure plate onto the flange as shown in Figure D-4.

Five thin-wall cylinders, tightly fitted to one another and to the inner shell, form the next structural layer of the overpack, strengthening the overpack against puncture or penetration. These cylinders are jointly referred to as the intermediate shells and act as the gamma shield. Channels welded to the outermost intermediate shell extend radially outward and delimit the last layer of the overpack. These channels act as fins, enhancing conduction to the periphery of the overpack. Plates welded between the ends of each successive channel complete the outer enclosure shell of the overpack. The cavities formed between the channel walls and between the outermost intermediate shell and the outer enclosure plates are filled with a neutron shield material that provides thermal insulation, in addition to neutron attenuation. The outermost intermediate shell, the neutron shield region, and the outer enclosure shell effectively extend the diameter of the overpack an additional 32.3 centimeters (cm) (12.7 in.) beyond the perimeter of the flange and the metal base cup.

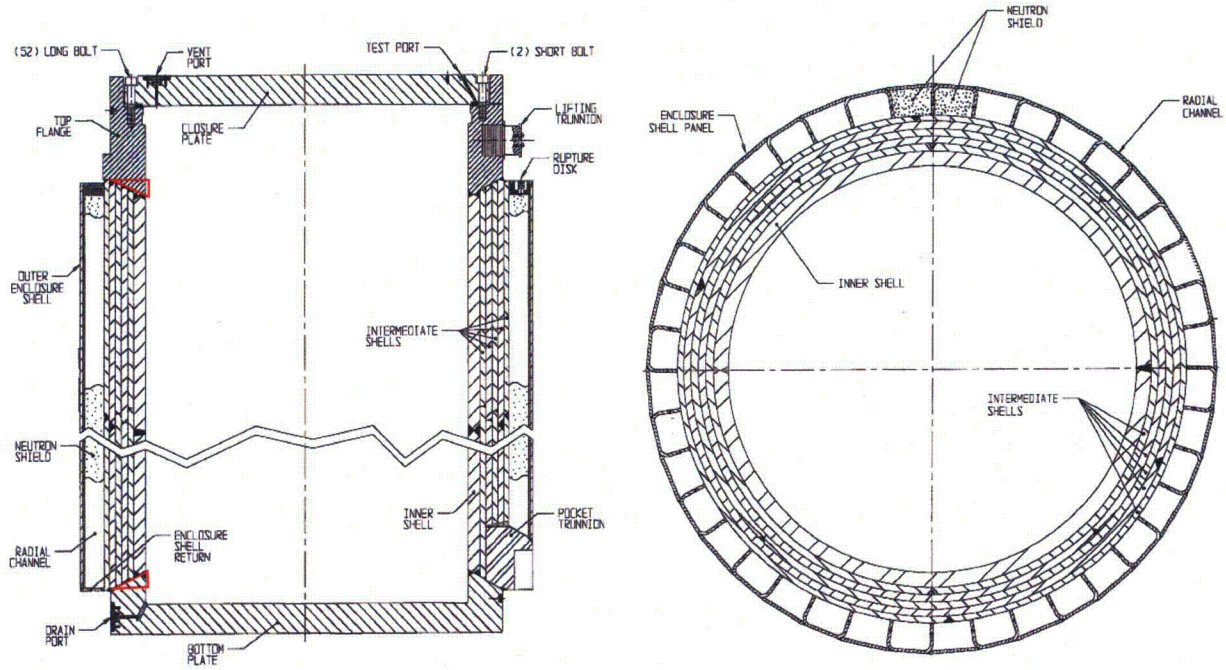

(a) (b)

Figure D-4 Rail-Steel cask overpack: (a) cross-sectional view through the center of the cask, (b) cross-sectional view through the midplane of the overpack (from Holtec International, 2000)

The overpack shells, metal base cup, flange, closure plate, and neutron shield region are the major components of the overpack; together they comprise most of its volume. The thermal modeling explicitly represents the overpack shells, metal base cup, flange, and closure plate, with minor alterations to simplify the solid modeling and meshing process. The most significant change extends the length of the overpack shells to the length of the outer enclosure shell. This change impacts the regions outlined in red in Figure D-4(a). As observed, the regions affected are where the overpack shells meet the metal plate cup and flange. Note that these length changes are more pronounced near the inner shell and gradually diminish radially outward. At most, the total length in question is less than 10 percent of the total length of the outer shell. The materials used for the metal plate cup and flange (cryogenic steel) and the overpack shell (carbon steel) have nearly the same thermal properties. There are contact gap regions between shells that are not present in the metal plate cup and flange. Therefore, these changes are expected to have some effect on the overall thermal response of the overpack, but only in the radial direction and limited to the region in question. The intermediate shells and the neutron shield region are each represented as a single volume to minimize geometric complexity; however, their thermal properties are accounted for in the thermal model using the techniques described in Sections D.3.3.3 and D.3.3.4.

The overpack contains additional components used to service the overpack during normal operations or designed to function only during abnormal ambient conditions, such as fires. These features include seals, gas ports, rupture disks, and lifting and pocket trunnions, as

shown in Figure D-4. The model does not include these components because their effects are assumed to be either (1) negligible because of their small volume and mass relative to the other components in the overpack or (2) highly localized, with no effect to the overall thermal performance of the cask at locations of interest or (3) both.

D.3.1.2 Multipurpose Canister

The MPC is a cylindrical vessel approximately 1.73 m (68.3 in.) in diameter (outside) and 4.83 m (190.3 in.) in length. The MPC is made from a cylindrical shell 1.2 cm (0.5 in) thick and 4.76 m (187.4 in) in length, a circular baseplate 6.35 cm (2.5 in.) thick, and a circular plate lid 24.1 cm (9.5 in.) thick (see Figure D-5a). The baseplate is welded to the bottom of the MPC shell, and this shell is in turn welded to the exterior surface of the lid. At the top, the MPC shell is flushed against a large groove on the end perimeter of the circular plate lid. An annular closure ring welded on the groove and to the top of the shell seals the contents of the MPC. In the horizontal position, the shell and the base plate rest on the inner shell of the overpack. Drain and vent ports on the MPC lid are used to evacuate and fill the MPC with an inert gas (generally helium). With the exception of the closure ring and drain ports, all these components are modeled explicitly. The closure ring is assumed to be part of the lid.

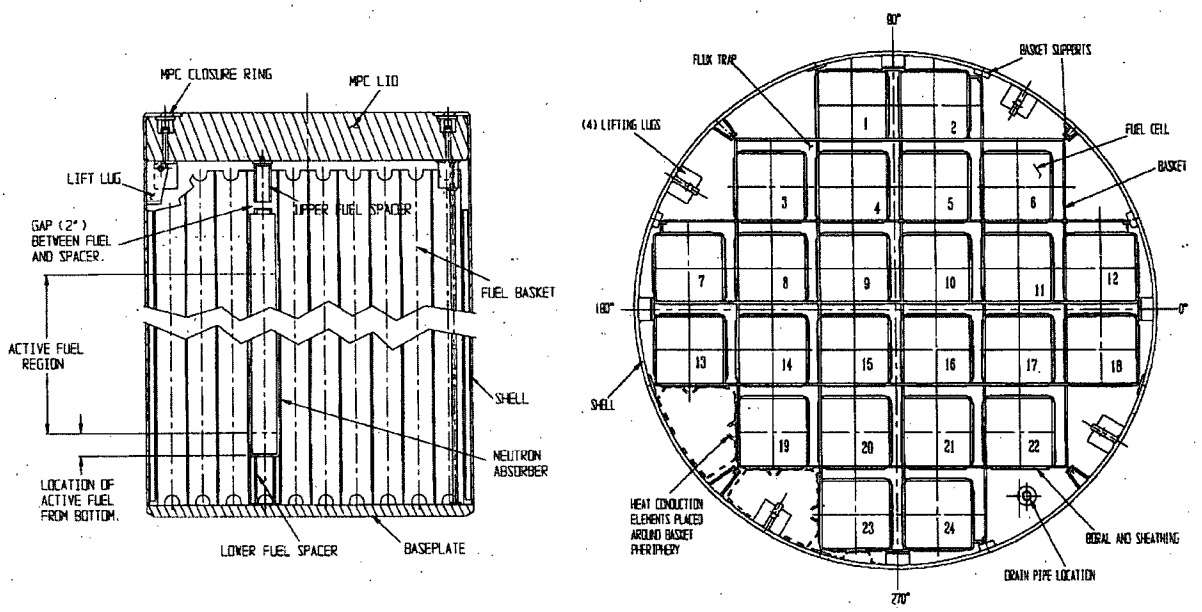

Figure D-5 Rail-Steel cask MPC: (a) cross-sectional view through the axis of the cask, (b) cross-sectional through the midplane of the overpack (from Holtec International, 2000)

The spent nuclear fuel (SNF) (or SNF assemblies) is stored in a fuel basket inside the MPC (see Figure D-5b). The fuel basket is made by welding a series of perpendicular and parallel plates to form an array of storage cells. Each storage cell contains a single fuel assembly. The Rail-Steel cask is designed to carry four general types of MPCs: (1) the MPC-24/-24E/-24EF, which contains a maximum of 24 pressurized-water reactor (PWR) fuel assemblies, (2) the MPC-32, which contains a maximum of 32 PWR fuel assemblies, (3) the MPC-68/-68F, which

contains a maximum of 68 boiling-water reactor (BWR) assemblies, and (4) the MPC-HB, which contains a maximum of 80 Humboldt Bay BWR assemblies. These MPC types are similar in design; however, the MPC-24 is designed to carry a greater specific heat load and the highest total heat load. For this reason, attention is focused on the MPC-24. In the MPC-24, the fuel cells are physically separated from one another by a gas pocket called the flux trap. The length of the fuel basket is approximately 4.48 m (176.5 in.). The fuel assembly might not reach this length; in such cases, spacers are installed on the baseplate and on the MPC lid to hold the fuel assemblies in place (see Figure D-5a).

A single fuel assembly consists of an array of fuel rods, each separated by a gas space (when the MPC is backfilled), as shown in Figure D-6a. The total number of rods per assembly varies with fuel assembly design. Each fuel rod consists of a number of cylindrical fuel pellets fitted into a thin-walled pipe, called the fuel cladding. The fuel cladding's inner diameter is slightly larger than the diameter of the pellets, as shown in Figure D-6b. The fuel pellets are held tightly against each other using the force of a spring. The radial dimensions of the rod components vary between fuel rod designs. In general, the length of the fuel column is only a fraction of the total length of the fuel rod and marks the active fuel region. The total length of the fuel rod is approximately the same as the length of the fuel assembly. Additional supports are added to the ends of the fuel assembly and at regular intervals along the length of the assembly for structural integrity to maintain spacing between the rods, as well as for handling purposes.

The Rail-Steel cask system is designed to carry a number of PWR fuel rods. It is impractical to analyze the Rail-Steel cask system with all of these fuel rod designs. Similarly, it is impractical to model the MPC contents with all the components described above because (1) the wide range of component length scales creates additional meshing complexities and (2) alternative methods have been employed in the SAR literature and in this study to obtain equivalent thermal properties for the MPC internal contents with good results (see Section D.3.4). Hence, the Rail-Steel cask model does not explicitly represent the fuel-basket region, which includes the fuel assembly, basket walls, and flux trap gaps.

The MPC shell contains support structures that help keep the fuel basket laterally in place and lift lugs, which are used during loading and unloading operations. Some slots between the periphery of the fuel basket and the MPC shell wall contain thin-wall heat conduction elements. These conduction elements extend the full length of the basket and provide an effective heat conduction path between the MPC basket and MPC shell. With the exception of the heat conduction elements, all other structural elements in the fuel-basket periphery region are ignored for the same reason cited in Section D.3.1.1. The fuel heat conduction elements are not represented explicitly, but their thermal effect is included through the use of a simplified analytical model explained in the Rail-Steel cask SAR.

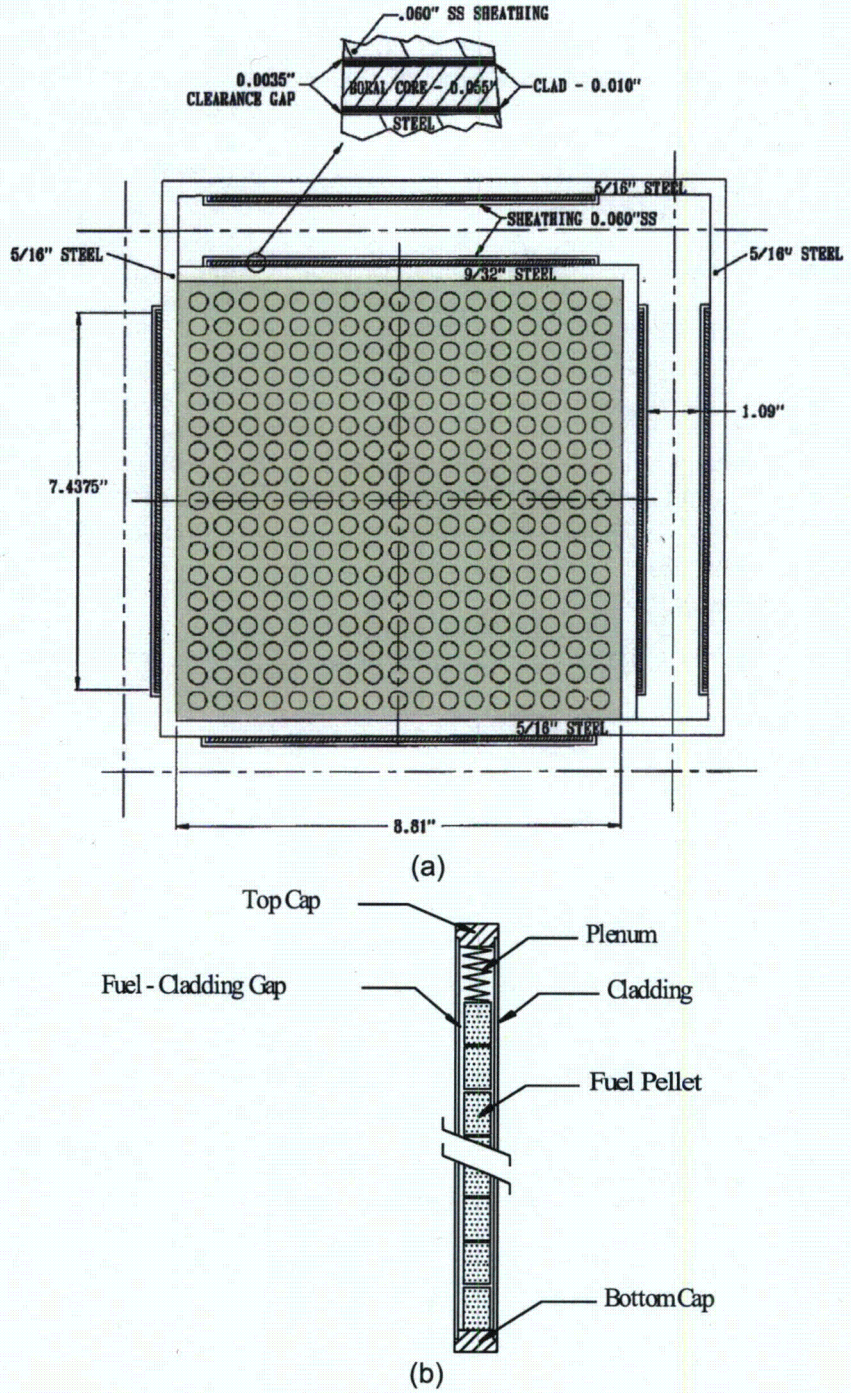

Figure D-6 Fuel assembly (a) and fuel rod (b)
(Figure D-6(a) from Holtec International, 2000)

To simplify the modeled geometry, the fuel-basket region and fuel-basket periphery region are modeled as two concentric cylindrical regions extending the length of the fuel assembly (see Figure D-7).

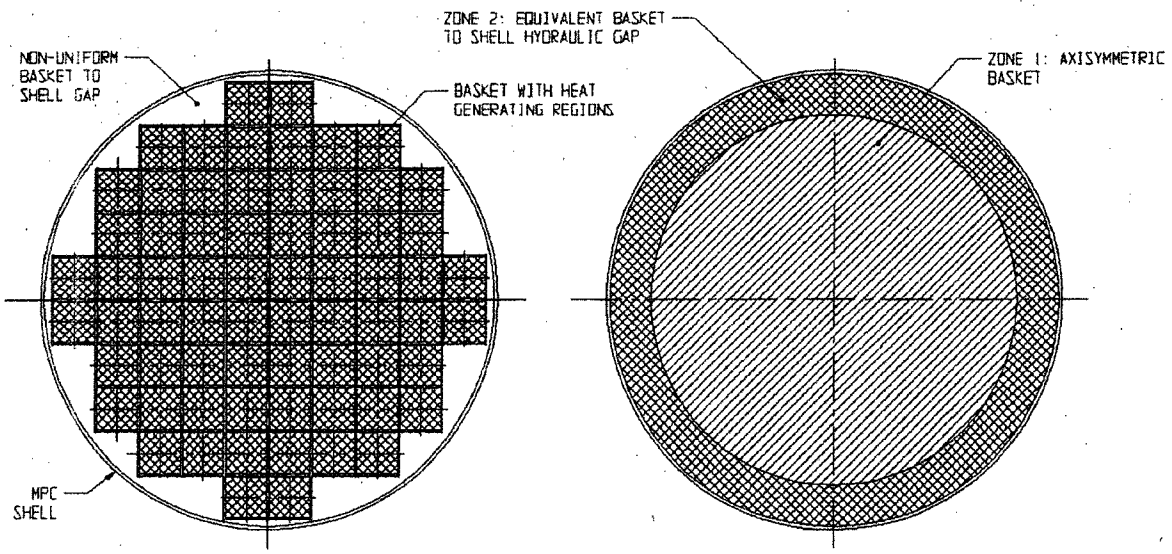

Figure D-7 Fuel-basket region (left) and equivalent fuel-basket region (right) (from Holtec International, 2000)

The diameter of the equivalent fuel-basket region (Zone 1) is calculated by using the hydraulic diameter of the fuel-basket periphery region (Zone 2). The hydraulic diameter takes into account the perimeter of the fuel basket, MPC support structures, MPC inner shell wall, and the area of the basket-to-shell gap—the total surface area between the perimeter of the fuel basket, MPC support structures, and MPC inner wall—through which heat transfer occurs. For the MPC-24 basket, the hydraulic diameter calculated using this method is approximately 12.7 cm (5 in.). The hydraulic diameter is also equal to the inner diameter of the MPC shell minus the inner diameter of the equivalent fuel-basket cylinder region. This provides a way to obtain the equivalent fuel-basket cylinder diameter and periphery annulus gap length (Zone 2). The periphery annulus gap length obtained from the hydraulic diameter calculation approximates the effective gap length through which heat is transferred between the irregular fuel-basket perimeter, the MPC support structures, and the MPC inner shell wall in the actual cask.

D.3.1.3 Rail-Steel Cask Impact Limiters

The impact limiters are relatively low-density cylindrical components that are not only designed to absorb energy during impact but also to serve as insulators during fires in the uncrushed state. The main body of the impact limiter has a maximum diameter of 3.25 m (128 in.) and a maximum length of 1.52 m (60 in.) (see Figure D-8).

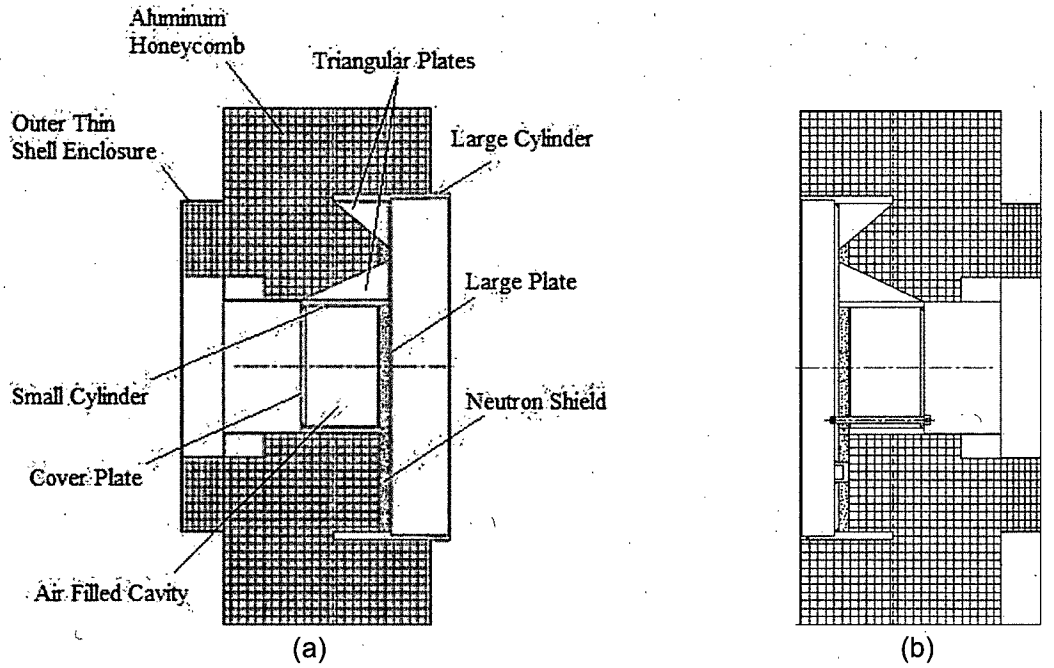

Figure D-8 Rail-Steel cask upper (a) and lower (b) impact limiters (from Holtec International, 2000)

Most of the impact limiter is honeycomb material enclosed in a thin shell metal wall. The honeycomb material and outer shell walls are supported in the interior of the limiter by a small and a large-diameter cylinder. Both these cylinders are concentric but offset axially from each other. As observed in Figure D-8, the small cylinder has uniform thickness, but the large cylinder has several wall thicknesses to accommodate the ends of the overpack. The small cylinder has a cover plate at one end and is welded to a large circular plate on the other end. The large plate is in turn welded to the large cylinder at its perimeter. The space inside this small cylinder is filled with air. Triangular plates welded to the large- and small-diameter cylinders complete the support structure in the interior of the impact limiter.

Each impact limiter contains a circular segment of neutron shielding, 6.35 cm (2.5 in.) thick, attached to the large plate on one side. This neutron shield provides axial neutron attenuation and serves as a heat barrier between the impact limiter body and the overpack ends.

The impact limiters are bolted to the ends of the overpack. The upper limiter bolts to the sides of the flange through the protruding section of the large cylinder, and the lower limiter bolts to the overpack metal base cup through the cover plate, neutron shield, and large plate, as shown in Figure D-8(b).

The impact limiters are assumed to stay intact after the hypothetical accident scenarios described in Chapter 4. This assumption is reasonable since the height of the flatbed railcar is approximately that of the diameter of the overpack. This height precludes any significant damage to the impact limiter during an accident scenario involving, for example, the overturn of the railcar flatbed. Since the limiters are assumed to stay intact, they are modeled in their original shape. The neutron shield material in the limiters is retained, but only up to the surface temperature at which the material starts to degrade (see Section D.3.3.4). Only the

large-diameter, thick-wall cylinder is explicitly modeled since it serves as a direct conduction path from the exterior to the interior of the limiter.

D.3.2 Rail-Steel Cask Thermal Behavior and Model Assumptions

The MPC-24 is designed to carry a maximum heat load of 20 kilowatt (kW) (0.833 kW per fuel assembly). This heat generation rate is nonuniform along the length of the active fuel region. Table D-1 shows the normalized, axial heat generation rate distribution for a typical Rail-Steel cask PWR assembly (Holtec International, 2000). This table is used to calculate the heat generation rate through the active length of the basket (i.e., in the axial direction). The Rail-Steel cask system is designed to reject heat passively to the environment under normal conditions of transport. Thus, heat is dissipated from the fuel rods to the exterior surfaces of the cask by a combination of conduction, convection, and radiation heat transfer modes.

Table D-1 Axial Burnup Profile in the Active Fuel Region of the Rail-Steel Cask

Axial Distance from Bottom of Active Fuel (% of Active Fuel Length)	Normalized Value
0% to 4-1/6%	0.548
4-1/6% to 8-1/3%	0.847
8-1/3% to 16-2/3%	1.077
16-2/3% to 33-1/3%	1.105
33-1/3% to 50%	1.098
50% to 66-2/3%	1.079
66-2/3% to 83-1/3%	1.050
83-1/3% to 91-2/3%	0.960
91-2/3% to 95-5/6%	0.734
95-5/6% to 100%	0.467

For normal transportation conditions, the internal temperature is higher than the external temperature of the cask; therefore, heat will be dissipated outwardly starting from the fuel rods. Inside the fuel rods, heat is transferred outward by (1) conduction through the gas space between rods and (2) radiation exchange between the fuel rods and between the fuel rods and the walls of the basket. Convection is assumed negligible in this region since radiation effects dominate at high temperatures. Heat is then dissipated by conduction through the gas space in the flux traps and by radiation between the basket walls. Convection is also assumed negligible in the flux trap region. In the fuel-basket periphery, heat is dissipated to the MPC shell by (1) conduction through the heat conduction elements and the gas and (2) radiation between the walls of the fuel basket and the MPC and between the inner walls of the heat conduction elements. In this region, natural convection loops enhance heat transfer between the inner walls

of the heat conduction elements. The results of the Rail-Steel cask SAR take this effect into account. A two-dimensional, finite element model is used to determine the heat convection coefficient for this region of the basket.

Heat transfer from the MPC shell to the overpack inner shell occurs through an MPC-overpack nonconcentric gap. In the horizontal position, the MPC makes contact with the overpack at the bottom. This contact gap is approximately 0.5 mm (0.02 in.) across. In this region, heat is also dissipated by conduction through the variable gas-filled gap and by radiation between the outer and inner walls of the MPC and overpack, respectively. The Rail-Steel cask SAR used a two-dimensional, analytical model to obtain an effective conductivity through the variable length gap, as discussed in Section D.3.3.2. Heat transfer through the inner and intermediate shells occurs by conduction through the shell material and through the contact gaps between the shells. These contact gaps are assumed to be five microns ($2x10^{-4}$ in.) across as in the Rail-Steel cask SAR. Conduction in the neutron shield region occurs in parallel through the radial connectors and the neutron shield material. A simple thermal resistor network is used to calculate the effective thermal conductivity through intermediate shells and through the neutron shield region (see Sections D.3.3.3 and D.3.3.4).

The Rail-Steel cask system is designed to maintain the temperature of components below their operational temperature limits[1] for normal conditions of transport and for a 30-minute, fully engulfing regulatory fire and subsequent cooldown period (10 CFR 71.73). For longer fully engulfing fires, such as the ones depicted in this study, a significant amount of heat may be transferred to the interior of the Rail-Steel cask, raising the temperature of some of its components to above their operational temperature limits. This is expected to occur in the neutron shield region. The operational temperature limit of the neutron shield insulation is 149 degrees Celsius (C) (300 degrees Fahrenheit (F)). In the model for this study, the neutron shield material is assumed to decompose completely shortly after it reaches this temperature limit, immediately triggering thermal radiation exchange between the overpack enclosure shell and the outermost intermediate shell. The assumption used in this study is a significant departure from the assumption made in the SAR. Section D.3.3 will discuss this point further. As with the neutron shield, the aluminum honeycomb is expected to reach temperatures beyond the operational temperature limits. However, the honeycomb material is not expected to completely melt. Given the results in Pierce et al. (2003), the regression rate of the honeycomb material is expected to be minimal over a 3-hour period and have only a local effect.

Heat dissipation through the cross-section (i.e., in the axial direction) of the MPC and overpack and through the limiters is assumed to occur mostly by conduction. Heat conduction occurs in parallel through each of the materials that comprise this cross-section. Thermal radiation in the axial direction is possible; however, since view factors tend to diminish with the distance square and angle of view and the temperature gradients are weak along the axis compared to the radial direction (as observed in contour results presented in Chapter 4), these effects are neglected in the basket region. Thus, radiation effects are assumed to be mostly in the radial direction, except near the lateral ends of the MPC. Thermal radiation exchange occurs between the MPC outer surface and the overpack inner lid and between the MPC outer surface and the overpack bottom plate. In the limiters, the thin metal shell covering the neutron shield radiates to the small

---

[1] The term operational temperature limit does not necessarily mean melting point. The Rail-Steel SAR provides operational temperature limits.

diameter plate located directly across the air gap that fills the small diameter cylinder (see Figure D-8 and the description in Section D.3.1.3).

With the exception of the contact gaps already mentioned (e.g., between intermediate shell layers and between the MPC and the overpack), all contact gaps in the Rail-Steel cask are assumed perfect.

D.3.3 Rail-Steel Cask Materials and Thermal Properties

The Rail-Steel cask system is made from a variety of steel and aluminum alloys. The overpack inner shell is made from SA203-E cryogenic steel, and the metal base cup, flange, and closure plate are made from SA350-LF3 cryogenic steel. The intermediate shells are made from SA516-70 carbon steel, and the radial channels and enclosure plates are made from SA515-70 carbon steel. The neutron shield material is Holtite-A, a synthetic neutron-absorbing polymer with 1-percent boron carbide, sold commercially under the trade name NS-4-FR (Holtec International, 2000). The variable-length gap between the MPC and overpack is filled with helium.

The MPC shell, lid, and baseplate; the basket; and the fuel-cell walls are made from alloy X, a generic term used in various SARs that usually stands for one of the following stainless steel metals: SA304, SA304LN, SA316, or SA316LN (Holtec International, 2000). The thermal properties of SA304 are assumed for these components. Very little difference in thermal properties is found between SA304 and the other stainless steel materials already mentioned. On one side of each fuel cell wall is a thin layer of Boral sandwiched between the fuel cell wall and thin stainless steel sheathing. Boral is a neutron absorber made of boron carbide and aluminum alloy 1100 (Holtec International, 2000). The Boral layer and stainless steel sheathing extend the length of the active fuel region. The MPC-24 is designed to carry intact Zircaloy and stainless steel clad fuel assemblies. In this study, the fuel rods are assumed to be made from Zircaloy cladding, as in the Rail-Steel cask for conservative results. The fuel pellets are uranium dioxide (UO_2). The MPC heat conduction elements are made from aluminum alloy 1100. All void spaces inside the MPC are filled with helium (Holtec International, 2000).

The honeycomb in the impact limiter is made from aluminum 5052, and the large-diameter cylinder is made from carbon steel (SA516). The neutron shield segments are also made from Holtite-A.

Table D-2 provides the thermal conductivity for materials used in the Rail-Steel cask at several temperatures. For aluminum 1100 and the various carbon steels, data from the Rail-Steel cask SAR are available over a limited temperature range. The analysis in that report showed only a limited range of temperatures because the fire exposure was limited to 30 minutes with a subsequent cooldown. For these materials, the data trend is decreasing; therefore, the thermal conductivity value at the highest temperature is used at higher temperatures. This reflects a conservative assumption since the thermal conductivity values used are higher than what they should be. Note also that Holtite-A is replaced with air once the temperature of the neutron shield region reached the operational temperature limit of that material. In reality, only a fraction of the Holtite-A decomposes. Some of the gases generated in the shield region outgas through the neutron shield rupture disks at high pressures. Up to 90 percent of these gases come from moisture in the Holtite-A (NRC, 2000). Experiments show that up to 50 percent (by weight) of

the NS-4-FR eventually degrades by the time the temperature of the material reaches 800 degrees C, leaving behind charred remains (Soo-Haeng et al., 1996), and these are not expected to combust (Soo-Haeng et al., 1996; NRC, 2000). The thermal conductivity of helium varies with pressure in addition to temperature; however, the pressure dependency is much weaker over the range of 101 to 689 kilopascals (14 to 100 pounds per square inch) (Petersen, 1970).

Table D-2 Thermal Conductivities for the Rail-Steel Cask Materials

Material	Thermal Conductivity W/m-°C (Btu/ft-hr-°F)				
	92 °C (200 °F)	226 °C (450 °F)	377 °C (700 °F)	477 °C (900 °F)	726 °C (1,340 °F)
Air[§]	0.026 (0.015)	0.040 (0.023)	0.050 (0.028)	0.055 (0.031)	0.067 (0.038)
Stainless Steel[§]	14.5 (8.3)	18.3 (10.5)	20.4 (11.8)	21.9 (12.6)	25.4 (14.6)
Aluminum Alloy 1100[*]	228 (131)	212 (122)	—	—	—
Aluminum-Honeycomb[‡]	3.5 (2.0)	4.1 (2.4)	4.8 (2.8)	5.2 (3.0)	—
Boral (B_4C)[*]	83.3 (48.2)	83.1 (48.0)	81.3 (47.0)	80.5 (46.5)	—
Carbon Steel- Int. Shells[*]	42.3 (24.5)	41.7 (24.1)	38.8 (22.4)	—	—
Carbon Steel-N. Shield[*]	50.7 (29.3)	49.1 (28.4)	42.6 (24.6)	—	—
Cryogenic Steel[*]	41.1 (23.8)	41.0 (23.7)	38.5 (22.3)	—	—
Helium[§]	0.17 (0.098)	0.22 (0.12)	0.26 (0.15)	0.29 (0.16)	0.35 (0.20)
Holtite-A[*]	0.65 (0.37)	—	—	—	—
UO_2[*]	6.0 (3.4)	6.0 (3.4)	5.1 (2.9)	—	—
Zircaloy[*]	13.5 (7.8)	14.6 (8.4)	16.2 (9.3)	17.8 (10.2)	—

§ Incropera and Dewitt, 1996
* Holtec International, 2000
‡ Thermophysical Properties Research Laboratory Inc., 2001

Table D-3 provides the specific heat for these same materials at several temperatures. Temperature-dependent values are given only for those materials that exhibited large variation in temperature. With the exception of stainless steel, aluminum 5052, and carbon steel, the specific heat of most materials used in the Rail-Steel cask is fairly constant. Of interest are the properties of carbon steel; the specific heat increases abruptly above 700 degrees C (1,292 F) and reaches a peak at around 768 degrees C (1,414 degrees F), the curie temperature. This behavior is associated with changes in the magnetic state of these materials and has been observed for a great number of carbon steel materials (Yafei, 2009). For Holtite-A, limited data are available above its operational temperature limit. Air properties are used beyond this limit. In addition, radiation exchange between the inner and outer surface of the neutron shield region is also allowed above this operational temperature limit to maximize heat input.

Table D-3 Specific Heat for the Rail-Steel Cask Materials

Material	Specific Heat J/kg-°C (Btu/lbm-°F)				
	92 °C (200 °F)	226 °C (450 °F)	377 °C (700 °F)	477 °C (900 °F)	726 °C (1,340 °F)
Air[§]	1,010 (0.24)	—	—	—	—
Stainless Steel[§]	482 (0.11)	535 (0.12)	563 (0.13)	575 (0.13)	611 (0.14)
Aluminum[§]	903 (0.21)	—	—	—	—
Aluminum-Honeycomb[‡]	890 (0.21)	976 (0.23)	1,057 (0.25)	1,100 (0.26)	—
Carbon Steel[§]	434 (0.10)	505 (0.12)	590 (0.14)	653 (0.15)	1,169 (0.27)
Boral (B_4C)[*]	2,478 (0.59)	—	—	—	—
Helium[§]	5,193 (1.2)	—	—	—	—
Holtite-A[*]	1,632 (0.39)	—	—	—	—
UO_2[*]	234 (0.056)	—	—	—	—
Zircaloy[*]	304 (0.073)	—	—	—	—

§ Incropera and Dewitt, 1996
* Holtec International, 2000
‡ Thermophysical Properties Research Laboratory Inc., 2001

Table D-4 provides densities for stainless steel, carbon steel, Zircaloy, and UO_2 at 92 degrees C (200 degrees F), and for air and helium at various temperatures. Since the density of most metals changes very little with temperature, only the values at 92 degrees C (200 degrees F) are used. The density of Holtite-A is assumed not to vary significantly from 92 degrees C (200 degrees F) to its operational temperature limit. Recall that air properties are used above this limit to replace Holtite-A.

Table D-5 shows the emissivity values obtained from the Rail-Steel cask SAR. The exterior surface of the Rail-Steel cask is coated with Carboline 890 paint, and the overpack inner surfaces are coated with Thermaline 450 paint. However, these coatings are only good up to 216 degrees C (422 degrees F) and 262 degrees C (505 degrees F), respectively (Holtec International, 2000). Note also the internal surfaces of the heat conduction elements are sandblasted to increase radiation between opposite sides of the heat conduction elements.

Table D-4 Densities for the Rail-Steel Cask Materials

Material	Density kg/m^3 (lbm/ft^3)				
	92 °C (200 °F)	226 °C (450 °F)	377 °C (700 °F)	477 °C (900 °F)	726 °C (1,340 °F)
Air[§]	0.98 (0.061)	0.69 (0.043)	0.54 (0.034)	0.46 (0.029)	0.35 (0.022)
Stainless Steel[§]	7,900 (493)	—	—	—	—
Aluminum[§]	2,702 (168)	—	—	—	—
Aluminum-Honeycomb[‡]	526 (32)	—	—	—	—
Carbon Steel[§]	7,854 (490)	—	—	—	—
Boral (B_4C)[*]	544 (34)	—	—	—	—
Helium[§]	0.14 (0.008)	0.10 (0.006)	0.077 (0.0048)	0.065 (0.0041)	0.048 (0.003)
Holtite-A[*]	1,681 (105)	—	—	—	—
UO_2[*]	10,956 (684)	—	—	—	—
Zircaloy[*]	6,551 (409)	—	—	—	—

§ Incropera and Dewitt, 1996
* Holtec International, 2000
‡ Thermophysical Properties Research Laboratory Inc., 2001

Table D-5 Emissivity for Some of the Rail-Steel Cask Materials and Paints

Material	Emissivity
Zircaloy	0.80
Painted Surface	0.85
Rolled Carbon Steel	0.66
Stainless Steel	0.36
Sandblasted Aluminum	0.40

D.3.3.1 Effective Thermal Properties of Fuel Basket and Fuel-Basket Periphery

Thermal properties for the fuel-basket region and fuel-basket periphery are obtained from the Rail-Steel cask SAR. In that report, the fuel basket and the fuel-basket periphery cross-sections were replaced with two concentric cylinders, each with equivalent effective thermal properties, as described in Section D.3.1.2. The procedure used to obtain the in-plane thermal conductivities of the fuel basket and fuel-basket periphery as a function of temperature is described in the Rail-Steel cask SAR, but is summarized here for completeness.

First, the cross-section of the fuel assembly is modeled using a detailed two-dimensional, finite element model of the cross-section of a 17×17 Optimized Fuel Assembly (OFA) rod arrangement (see Figure D-7a), a uniform heat generation rate over each fuel rod, and a uniform temperature applied to the periphery of the fuel assembly. The 17×17 OFA used was determined to be the most resistive assembly design (Holtec International, 2000). The finite element model takes into account radiation between the rods and conduction across the helium gap. The effective thermal conductivity is obtained from the following equation:

(D-1) $$k_{eff} = \frac{0.29468(q_g a^2)}{\Delta T}$$

Where q_g is the heat generation rate per fuel cell per unit length, a is half the length of one side of the fuel cell, and ΔT is the maximum temperature difference in the fuel assembly (Sanders et al., 1992). Since radiation is not linearly dependent on temperature, the model is run several times, each time with increasing uniform temperature near the edge of the fuel assembly to obtain effective properties at various temperatures. The detailed fuel assembly is thus replaced with a homogenized fuel cell region (see Figure D-7)

Second, the in-plane thermal conductivity of the basket storage wall, Boral, and stainless steel sheathing are replaced with an equivalent thermal conductivity using the thermal resistor network described in the Rail-Steel cask SAR. The representative network takes into account the thermal resistances perpendicular to the wall and along the wall.

Third, the cross-section of the MPC is modeled using a two-dimensional, finite element representation of the homogenized fuel-basket walls, with a uniform heat generation rate applied over each homogenized fuel assembly and a uniform temperature applied over the perimeter of the MPC shell. The model in the Rail-Steel cask SAR took into account (1) conduction through the homogenized fuel assemblies, the helium gas in the flux traps, and the basket periphery, (2) radiation between homogenized basket walls, and (3) natural convection loops in the basket periphery. The effective conductivities of the basket region (k_b) and periphery region (k_p) are given by the following equations:

(D-2) $$(k_b)_{eff} = \frac{q}{4\pi\Delta T_{bm}}$$

(D-3) $$(k_p)_{eff} = \frac{qW}{A_s\Delta T_{pb}}$$

Where

(D-4) $$\Delta T_{pb} = \Delta T_{pm} - \Delta T_{bm}.$$

Here, q is the MPC heat generation per unit length, ΔT_{bm} is the maximum temperature difference in the basket, ΔT_{pm} is the maximum temperature difference in the MPC cross-section, A_s is the surface area per unit length, and W is the basket periphery annular gap length. Table D-6 give the equivalent fuel-basket thermal conductivities. The Rail-Steel cask SAR obtained the effective axial thermal conductivities of the fuel basket by using the resistor method, which reduces to an area-weighted average since the basket length (L) in the resistance (L/kA) is equal across all materials. The specific heat and density are obtained using a mass- and volume-weighted average, respectively. Near the ends of the basket, the fuel rods

are filled with gas, decreasing the in-plane and axial thermal conductivity of the basket slightly since the thermal conductivity of helium is smaller than the UO_2 pellets. Note that the thermal conductivities did not vary much in temperature.

The properties in Table D-6 are used over the length of the basket. For consistency, temperature varying properties are implemented in the thermal model.

Table D-6 Effective Thermal Conductivity for the Fuel-Basket Region

Effective Thermal Properties	92 °C (200 °F)	226 °C (450 °F)	377 °C (700 °F)	477 °C (900 °F)	726 °C (1,340 °F)
In-Plane Thermal Conductivity W/m-°C (Btu/ft-hr-°F)	1.9 (1.1)	2.6 (1.5)	3.4 (1.9)	—	—
Axial Thermal Conductivity W/m-°C (Btu/ft-hr-°F)	3.4 (1.9)	3.8 (2.2)	4.3 (2.5)	4.6 (2.6)	—
Specific Heat J/kg-°C (Btu/lbm-°F)	305 (0.073)				
Density kg/m^3 (lbm/ft^3)	2,688 (168)				

Fuel spacers separate the ends of the fuel assembly from the MPC lid and MPC bottom plate. In these regions, conduction is predominately through the helium gas and through the fuel spacer and fuel-basket walls. Thermal radiation also occurs between the walls of the basket and the fuel spacers.

The homogenized material properties used in the fuel-spacer region are estimated by taking into account the properties of the fuel region, fuel spacer, the helium, the fuel-basket ends, and thermal radiation. A sensitivity study using theoretical bounds indicated that the temperatures obtained in the regions of interest were barely influenced by the properties used.

Fourth, the thermal conductivity in the basket periphery is further enhanced to account for heat dissipation through heat conduction elements. The equivalent resistor network through the heat conduction elements is obtained using a two-dimensional, analytical model explained in the Rail-Steel cask SAR. This resistance is added in parallel with the resistance obtained from the two-dimensional, finite element model for the basket periphery region. Table D-7 provides the fuel-basket periphery, in-plane conductivity.

Researchers determined the axial effective thermal conductivity from an area-weighted average using aluminum 1100 and helium properties. Holtec International (2000) gives the area of the periphery region. The area of the heat conduction elements is estimated at 3.5 times the fuel basket's cell pitch (27.3 cm (10.7 in.)) multiplied by the thickness of the elements (3.175 mm (0.125 in.)) and the total number of aluminum inserts (i.e., eight) (Holtec International, 2000). The specific heat and density of the fuel-basket periphery is obtained from an area- and mass-weighted average, respectively, again considering only aluminum 1100 and helium.

Heat transfer through the periphery region is further enhanced by radiation between the inner walls of the heat conduction elements and the walls of the MPC and fuel basket. As

demonstrated in Table D-6, the emissivity of stainless steel and sandblasted aluminum are not very different.

Table D-7 Effective Thermal Conductivity of the Aluminum Heat Conduction Elements

Effective Thermal Properties	92 °C (200 °F)	226 °C (450 °F)	377 °C (700 °F)	477 °C (900 °F)	726 °C (1,340°F)
In-Plane Thermal Conductivity W/m-°C (Btu/ft-hr-°F)	0.43 (0.25)				
Axial Thermal Conductivity W/m-°C (Btu/ft-hr-°F)	10 (5.8)				
Specific Heat J/kg-°C (Btu/lbm-°F)	964 (0.23)				
Density kg/m^3 (lbm/ft^3)	132 (8.25)				

D.3.3.2 Effective Thermal Properties of Multipurpose Canister-Overpack Helium Gap

In the horizontal position, the MPC rests on the overpack, forming a nonconcentric, variable-length helium gap. This gap is not modeled explicitly. Instead, the study used a two-dimensional, analytical model derived in Holtec International (2000) to obtain an effective conductivity through the variable-length gap. This model included the effects of the contact region as explained below.

To account for radial heat dissipation through the variable-length, helium gap and through the metal-to-metal contact area, equations for the overall heat conducted through these regions are summed and then equated to the overall heat conducted through a concentric gap to obtain an effective thermal conductivity for a constant-length helium gap (i.e., concentric gap). The following equation, taken from the Rail-Steel cask SAR, was used to obtain the effective thermal conductivity across the gap (k_{gap}):

(D-5)
$$\frac{(k_{gap})_{eff}}{k_{gas}} = \frac{t}{\pi}\int_0^{\pi} \frac{1}{t\,(1-\cos\theta)+\varepsilon\cos\theta}\,d\theta$$

Where k_{gas} is the conductivity of the gas, t is the thickness of the concentric gap, and ε (0.5 mm (0.02 in.)) is the metal-to-metal contact area width. Results reported in the SAR show that the effective conductivity through the equivalent concentric gap is twice the conductivity of helium.

D.3.3.3 Effective Thermal Properties of Overpack Intermediate Shells

The Rail-Steel cask consists of a series of shell-gas layers between the inner shell wall and the outermost intermediate shell of the overpack. The contact gaps are assumed to be 0.05 mm (0.002 in.) across (Holtec International, 2000). No radiation is assumed through these gaps since radiation accounts for less than 5 percent of the effective conductivity for gaps of this size. Researchers obtained the in-plane thermal conductivity by adding the resistances across each shell and gap in series (see Table D-8). The axial and circumferential conductivities are

assumed to be that of the shell layer material since the thermal conductivity of air and the gap area of air contribute very little. Similarly, the specific heat and density of the intermediate shell layers are assumed to be equal to the intermediate shell material.

Table D-8 Effective Thermal Conductivity of the Intermediate Shells in the In-Plane Directions

Effective Thermal Properties	92 °C (200 °F)	226 °C (450 °F)	377 °C (700 °F)	477 °C (900 °F)	726 °C (1,340 °F)
In-Plane Thermal Conductivity W/m-°C (Btu/ft-hr-°F)	13.2 (7.6)	15.6 (9.0)	17.0 (9.8)	18.6 (10.7)	22.1 (12.7)

D.3.3.4 Effective Thermal Properties of Neutron Shield Region

The neutron shield region consists of the Holtite-A inside the cavities formed between the outermost intermediate shell and the outer enclosure shell and between the radial channels. Note that the outer enclosure shell is not included here because it is modeled explicitly. The neutron shield region includes the Holtite-A material and the radial sections of the channel (2 per channel for a total of 40). This region is also modeled as a single volume with homogenized thermal properties.

Table D-9 shows the effective properties in the neutron shield region. The effective thermal conductivity in the in-plane and axial direction are obtained by summing the resistance through the radial channels and through the neutron shield material in parallel. Since both the Holtite-A and radial channels extend the same length in the axial direction, the resistance equation in the axial direction reduces to an area-weighted average of the individual material conductivities. Researchers used air in place of Holtite-A to calculate the effective properties above 149 degrees C (300 degrees F), taking into account the radial channels.

Table D-9 Effective Conductivity of the Neutron Shield Region

Effective Thermal Properties	92 °C (200 °F)	226 °C (450 °F)	377 °C (700 °F)	477 °C (900 °F)	726 °C (1,340 °F)
In-Plane Thermal Conductivity W/m-°C (Btu/ft-hr-°F)	4.3 (2.4)	3.5 (2.0)	3.2 (1.8)	3.1 (1.8)	2.7 (1.5)
Axial Thermal Conductivity W/m-°C (Btu/ft-hr-°F)	3.6 (2.0)	3.3 (1.9)	3.0 (1.7)	3.0 (1.7)	2.6 (1.5)
Specific Heat J/kg-°C (Btu/lbm-°F)	1,315 (0.31)	505 (0.12)	590 (0.14)	653 (0.15)	1,130 (0.28)
Density kg/m^3 (lbm/ft^3)	2,113 (132)	552 (34)			

The thermal conductivity in the circumferential direction is assumed to be that of Holtite-A since the total thickness of the radial channels in this direction is small compared to the total circumferential length of the Holtite-A. Note that this is a conservative assumption in the sense

that heat dissipated through the neutron shield region is preferentially in the in-plane and axial directions as a result of the latter assumption. This assumption does not have an impact in the uniform-heating run, but it does have an impact on the CAFE fire runs, where heat input around the circumference of the cask varies. In this case, heat will be dissipated more readily through the in-plane direction, thus giving higher temperatures in the interior of the cask.

Researchers obtained the specific heat and density of the neutron shield region using a mass- and area-weighted average, respectively. Holtite-A is expected to reach its temperature limit during the early transient period of a fire. When this happens, Holtite-A partially decomposes, leaving char residue behind. Most of the excess gas generated in Holtite-A outgases through the rupture disks when the pressure inside the neutron shield region reaches the disks' design limits. In the thermal model, when Holtite-A's temperature limit is reached, Holtite-A is replaced with air, and radiation is activated by setting the emissivity to an appropriate value. Note that air effectively lowers the specific heat and density of the neutron shield region. The effective specific heat of the neutron shield region is greatly influenced by the specific heat values of carbon steel since the density of air in the mass-weighted average is very small compared to carbon steel.

D.3.4 Rail-Steel Cask, Finite Element Model, and Boundary Conditions

A steady-state case was run to obtain the initial conditions of the Rail-Steel cask and to compare results against those provided in the Rail-Steel SAR and Adkins et al. (2006). The steady-state model consisted of exposing the Rail-Steel cask to a 37.8-degree C (100-degree F) ambient-temperature, radiation boundary condition. This boundary condition is applied over the entire outer surface of the cask using an emissivity value of 0.85. In addition, insolation is applied over the outer curved surfaces of the cask (193.8 watts per square meter (W/m^2) (61.4 British thermal unit per square foot per hour (Btu/ft^2-hr)) and over the flat ends of the cask (96.9 W/m^2 (30.7 Btu/ft^2-hr)), as specified in American Society of Testing Materials E2230, "Standard Practice for Thermal Qualification of Type B Packages for Radioactive Material" (ASTM, 2008). A convection boundary condition is also applied to the outer surface of the cask using a heat transfer coefficient of 3 W/m^2-°C (0.53 Btu/ft^2-hr-°F). This value is obtained from a set of correlations described in the Rail-Steel cask SAR—assuming turbulent flow—and is within the same order of magnitude as values obtained from correlations in (Incropera and Dewitt, 1996).

In general, steady-state results are slightly higher than those presented in the Rail-Steel cask SAR, but lower than those reported in Adkins et al. (2006). For example, the current study found a maximum fuel cladding temperature of 376 degrees C (710 degrees F), compared to 372 degrees C (701 degrees F) in the Rail-Steel cask SAR and 392 degrees C (738 degrees F) in Adkins et al. (2006). The largest differences are observed in the extreme ends of the overpack, where temperatures in the Rail-Steel cask are lower (by approximately 25 degrees C (45 degrees F)) than reported here and significantly lower (approximately 50 degrees C (90 degrees F)) than what is reported in Adkins et al. (2006). These differences are attributed to dissimilarities in modeling assumptions and approaches and boundary conditions. For example, Adkins et al. (2006) assumed a gap between the overpack and the limiters. Overall, however, the temperatures obtained from these three studies showed similar spatial trends and good agreement given the differences cited above.

The steady-state case is used to assess the suitability of the mesh. The mesh is initially 169,600 elements; this corresponds to a nominal element size of 10.2 cm (4 in.). This value is decreased to 5.1 cm (2 in.) and then increased to 15.2 cm (6 in.) to study the effects of element size on temperatures at locations of interest (as shown in the results of Chapter 4 and later in this appendix). Results of the 15.2-cm (6-in.) element-size mesh showed some difference in the temperatures in the interior of the cask when compared to those of the 10.2-cm (4-in.) element-size mesh. This is expected since large cells are created in the interior of the cask. Near the exterior of the overpack, small geometric features resulted in small size elements. Results of the 5.1-cm (2-in.) element-size mesh showed very little difference when compared to the 10.2-cm (4-in.) element-size mesh. The 5.1-cm (2-in.) element-size mesh had smaller elements in the interior and about the same near the exterior of the overpack. Therefore, a third case was run, this time using the 10.2-cm (4-in.) mesh, with a refined mesh near the exterior of the overpack. Results from this mesh showed some difference (less than 5 degrees in the neutron shield region), but not enough to justify the extra computational time needed to run this mesh. Figure D-9 shows the final mesh used to run the five scenarios described in Chapter 4.

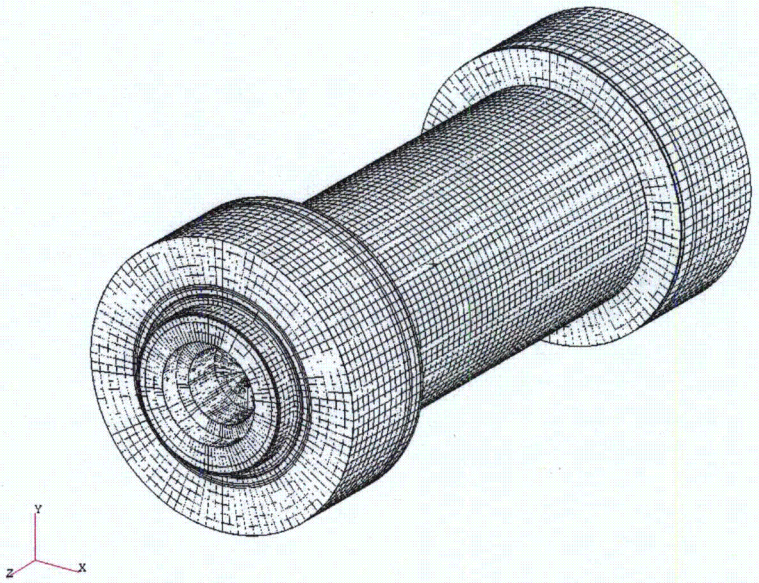

Figure D-9 Rail-Steel cask finite element mesh

The uniform-heating case described in Chapter 4 was run initially to verify the Rail-Steel cask finite element model. This exercise gave an additional measure of confidence in the Rail-Steel cask model. The boundary conditions for this case consisted of exposing the Rail-Steel cask to an 800-degree C (1,472-degree F) ambient-temperature, radiation boundary condition. This boundary condition is applied over the entire outer surface of the cask using an emissivity value of 0.9. A convection boundary condition is also applied to the outer surface of the cask using a heat transfer coefficient of 85 W/m^2-°C (15.2 Btu/ft^2-hr-°F). The Rail-Steel cask SAR obtains this value from a set of correlations described within that report. The Rail-Steel cask SAR also assumes a vertical flame speed of 15 meters per second (m/s) (49 feet per second (ft/s)), a value significantly higher than that specified in Nakos (2005) but nevertheless conservative because it will result in a higher heat input to the cask. Convection accounts for about 10 to

20 percent of the total heat input for large objects inside a fire; the rest is through thermal radiation (Nicolette and Larson, 1989).

The uniform-heating case is run for 30 minutes, followed by an 11.5-hour transient cooldown with insolation. During the cooldown period, the boundary conditions are set back to their steady-state case values, except for the emissivity of the outer cask, which remains the same to simulate what happens in actual fires—a blanket of soot covers the cask. Also, unlike the Rail-Steel cask SAR, the neutron shield region is assumed to contain air with radiation interaction between the outer enclosure shell and the outermost intermediate shell.

Overall, maximum temperatures obtained using the model developed in this study and in the Rail-Steel cask SAR are similar. The difference in purpose of the two analyses leads to some different assumptions, which in turn leads to slightly different results.

For the remaining cases, the external boundary conditions are obtained from CAFE, the computational fluid dynamics code coupled to P/Thermal. As mentioned in Section D.2, a boundary condition was set up in Patran that allowed CAFE results to be communicated to P/Thermal and vice-versa. The cooldown period for these cases also used the steady-state case boundary conditions (from 10 CFR 71.71, "Normal Conditions of Transport").

D.3.5 Rail-Steel Cask Thermal Analysis Results

Figure D-10 through Figure D-14 show results for the five scenarios already described in Chapter 4. These results are not discussed here, but are presented to supplement results discussed in Chapter 4. Figure D-10 shows results for the regulatory uniform-heating case cited in the previous section. This is the P/Thermal-only run. Figure D-11 shows results for the regulatory CAFE fire and, together with Figure D-10, may be useful in determining the differences between uniform and nonuniform fire conditions.

Nicolette and Larson (1989) discuss the effect that large objects have on fires and their implications to modeling large casks in fires. Figure D-12 shows results for the fully engulfing CAFE fire with the cask on the ground, and Figure D-13 and Figure D-14 show results for the cask on the ground but outside the fire. The last three cases are for a 3-hour fire and subsequent cooldown period.

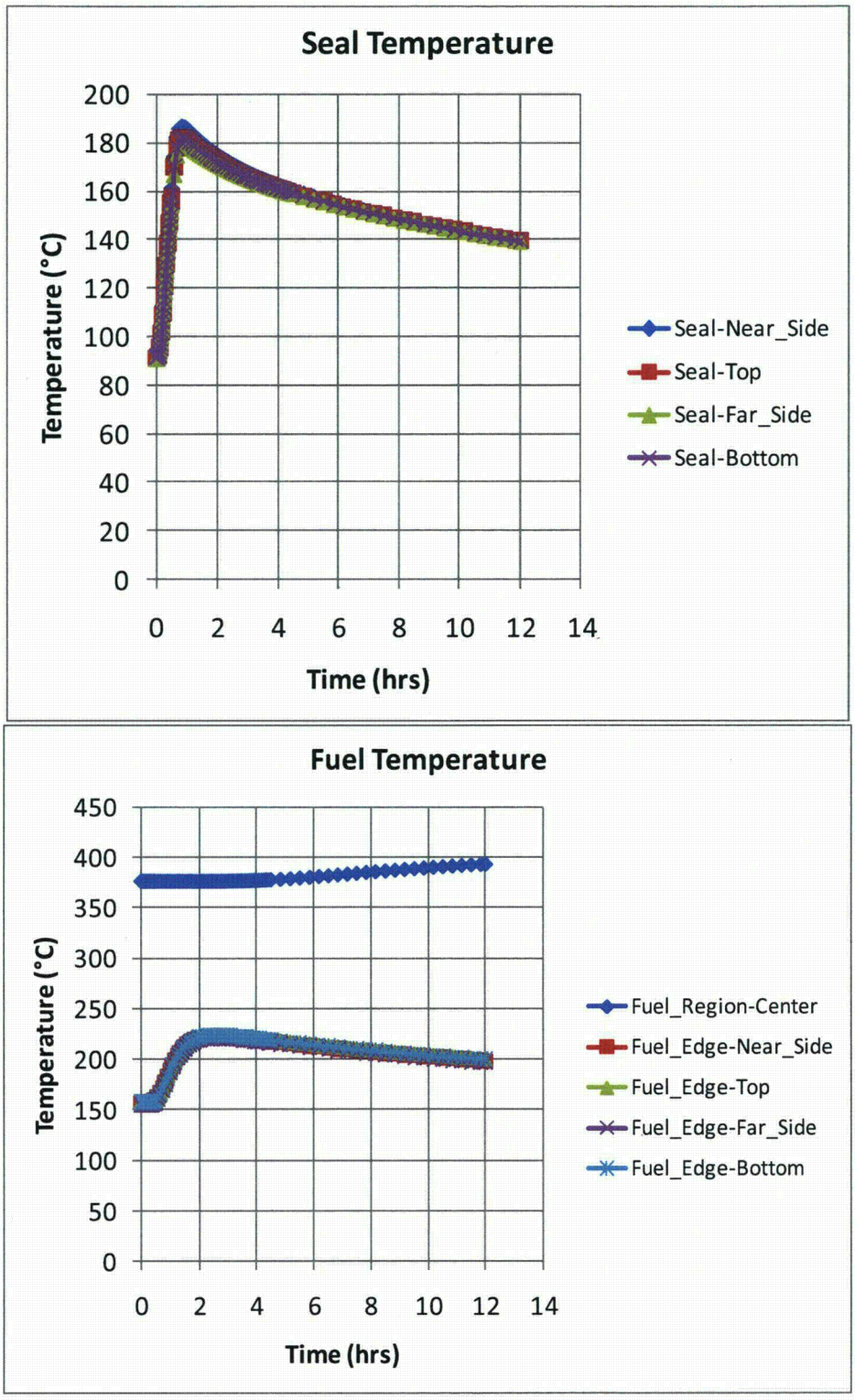

Figure D-10 Rail-Steel cask regulatory uniform-heating results (P/Thermal)

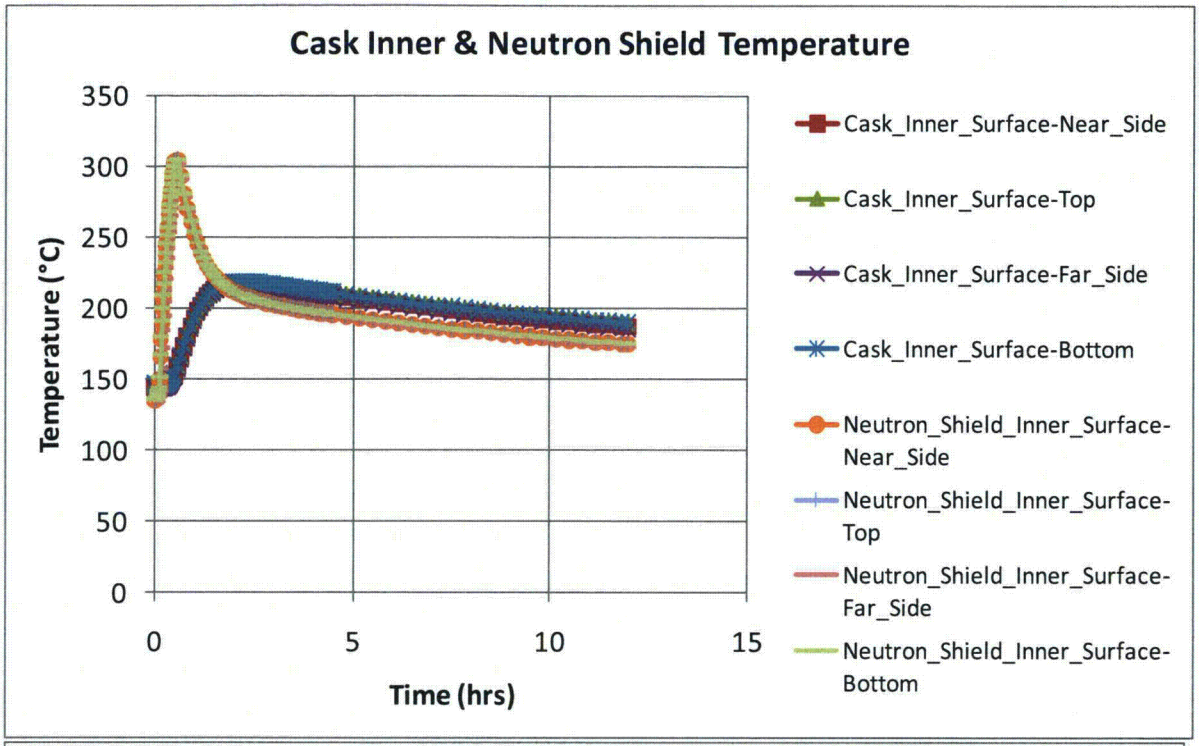

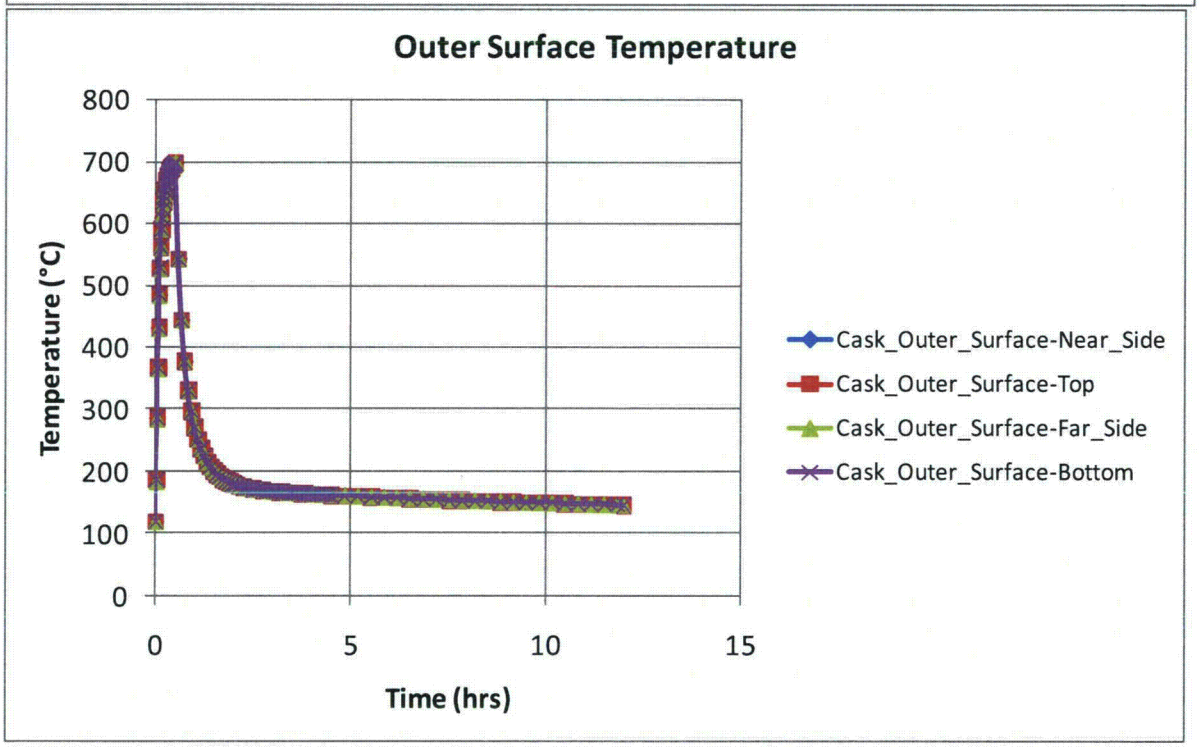

Figure D-10 Rail-Steel cask regulatory uniform-heating results (P/Thermal) (continued)

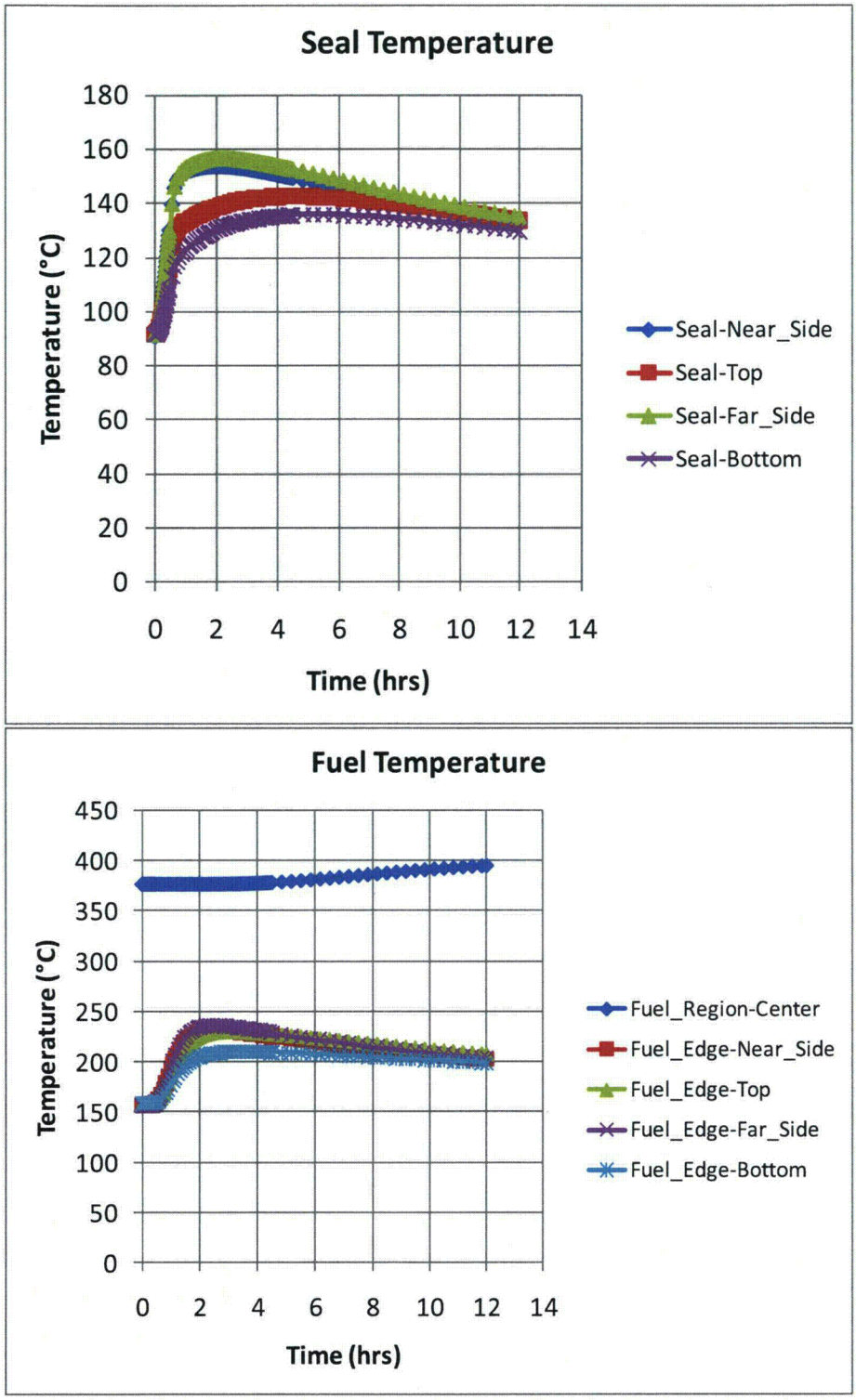

Figure D-11 Rail-Steel cask CAFE regulatory fire

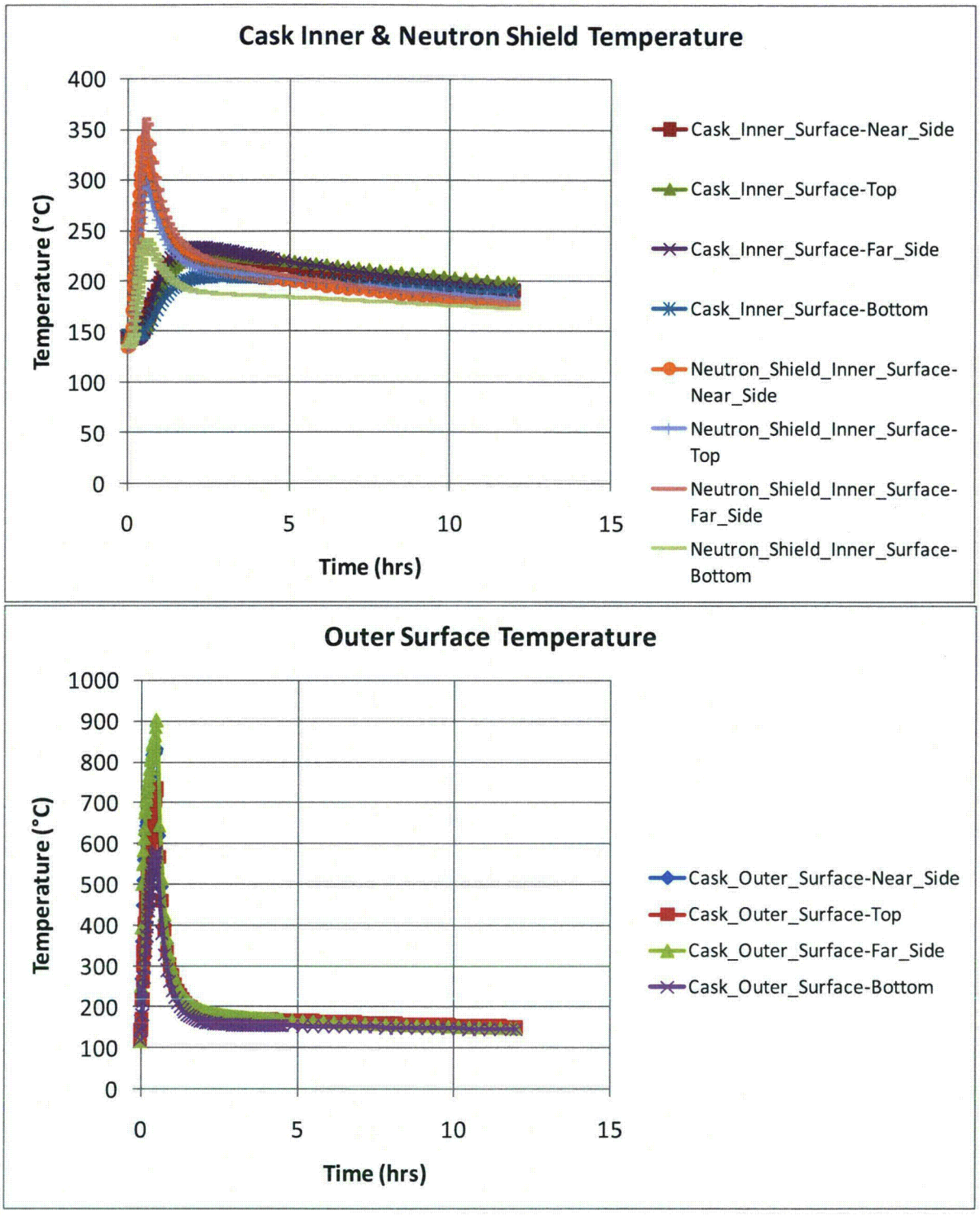

Figure D-11 Rail-Steel cask CAFE regulatory fire (continued)

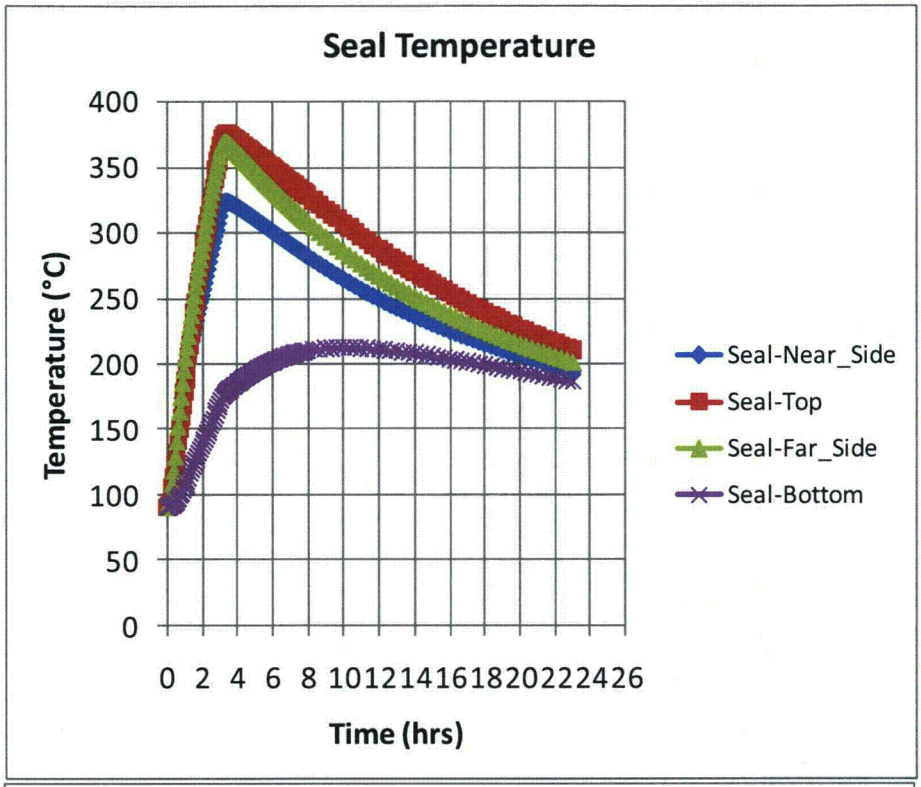

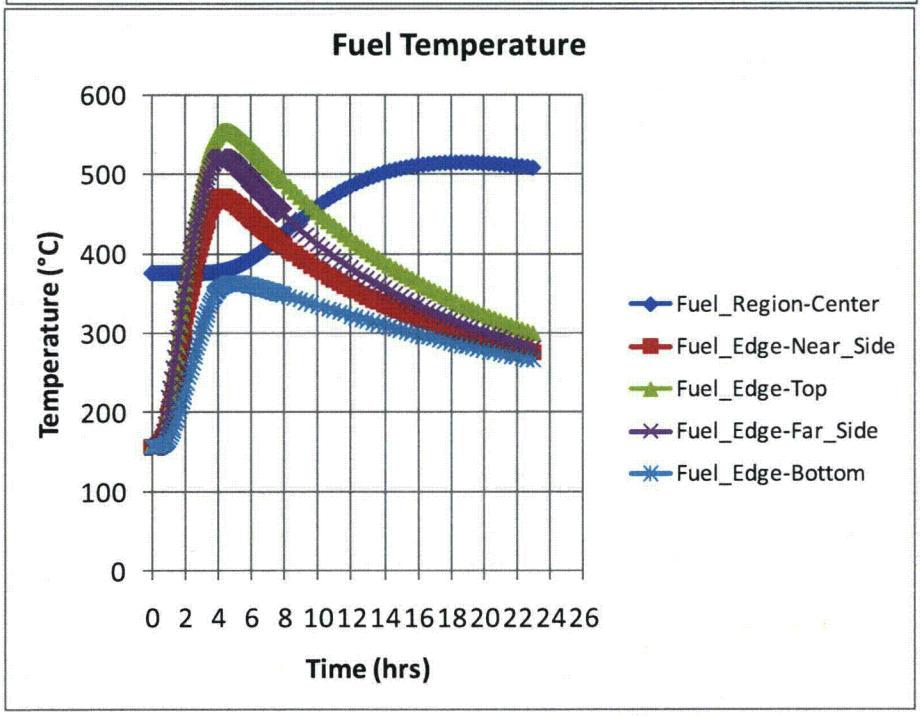

Figure D-12 Rail-Steel cask CAFE fire with cask on ground and at the pool center

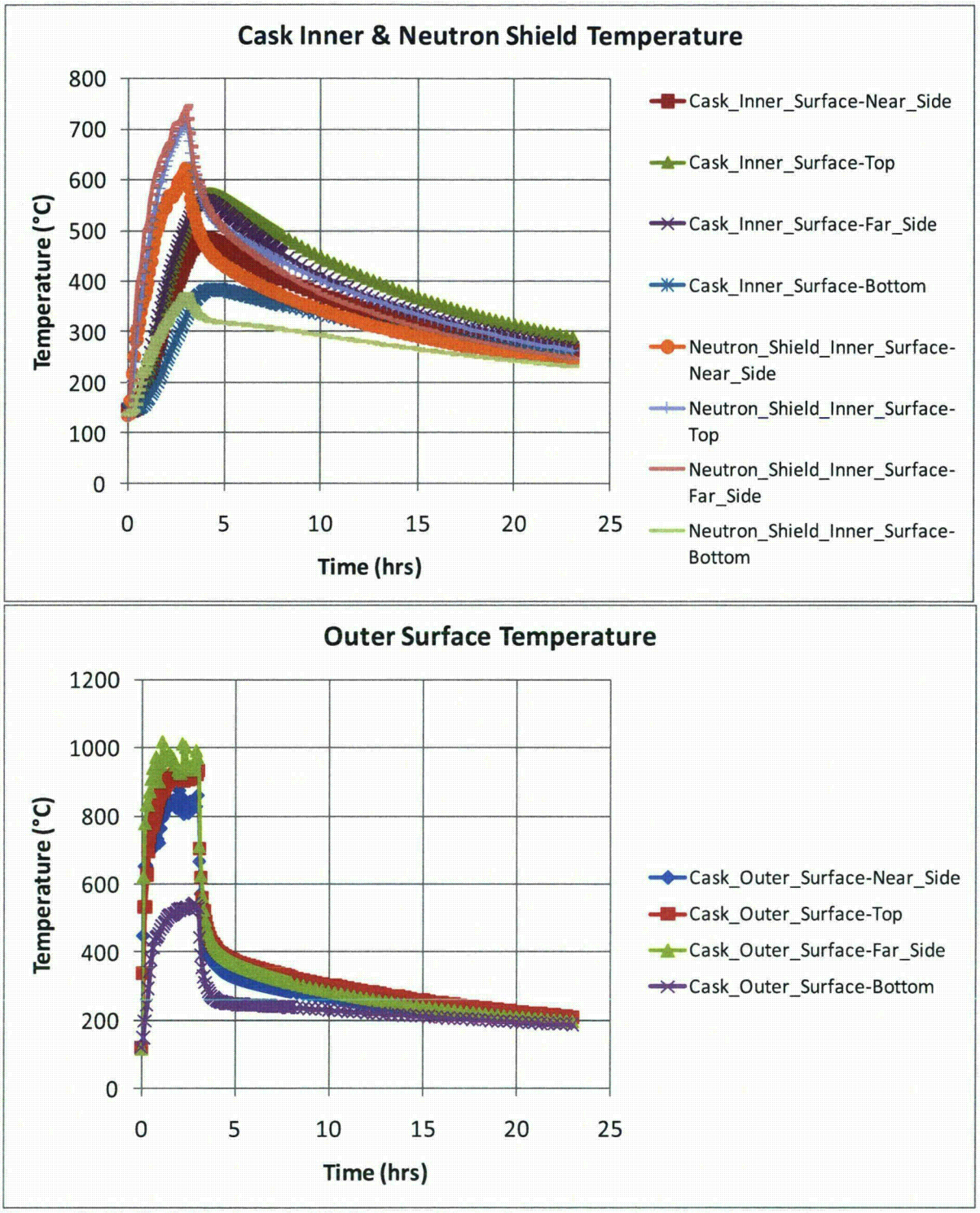

Figure D-12 Rail-Steel cask CAFE fire with cask on ground and at the pool center (continued)

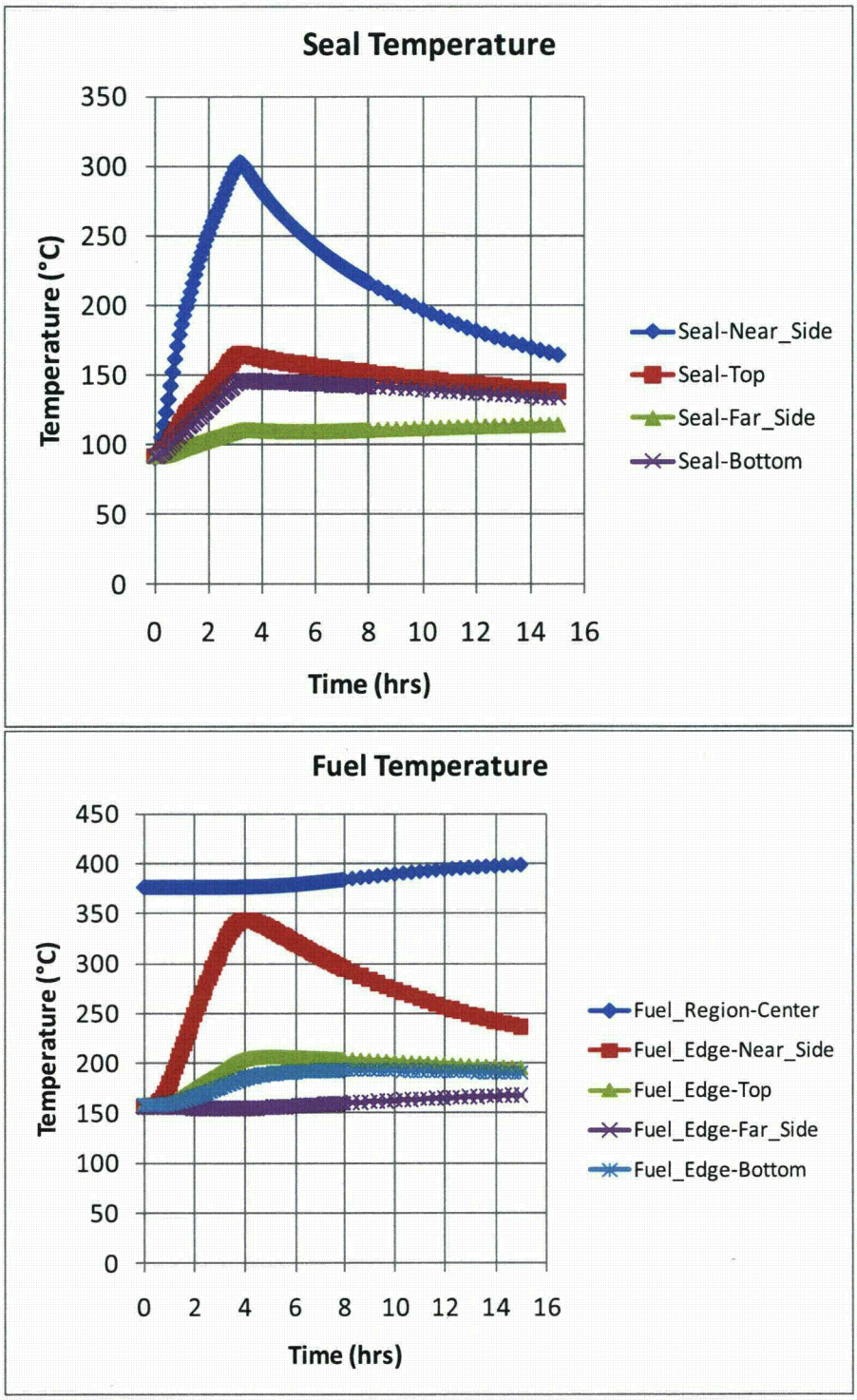

Figure D-13 Rail-Steel cask CAFE fire with cask on ground 3 m (10 feet) from the edge of the pool

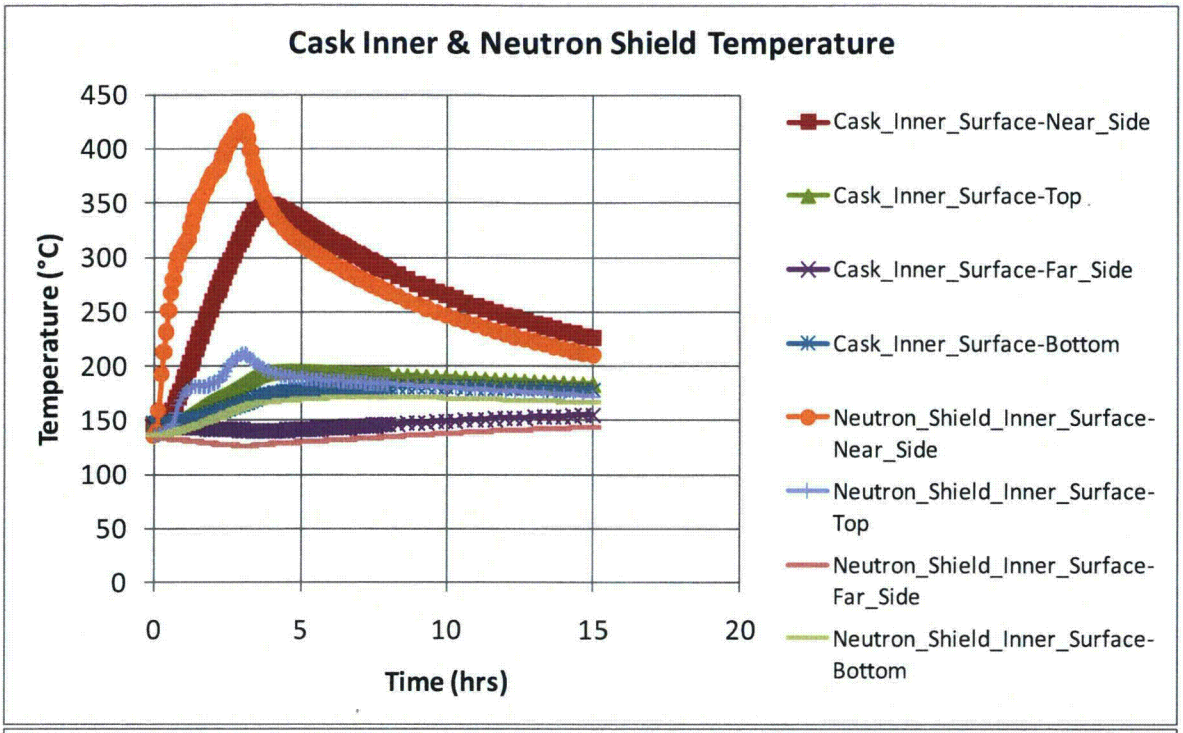

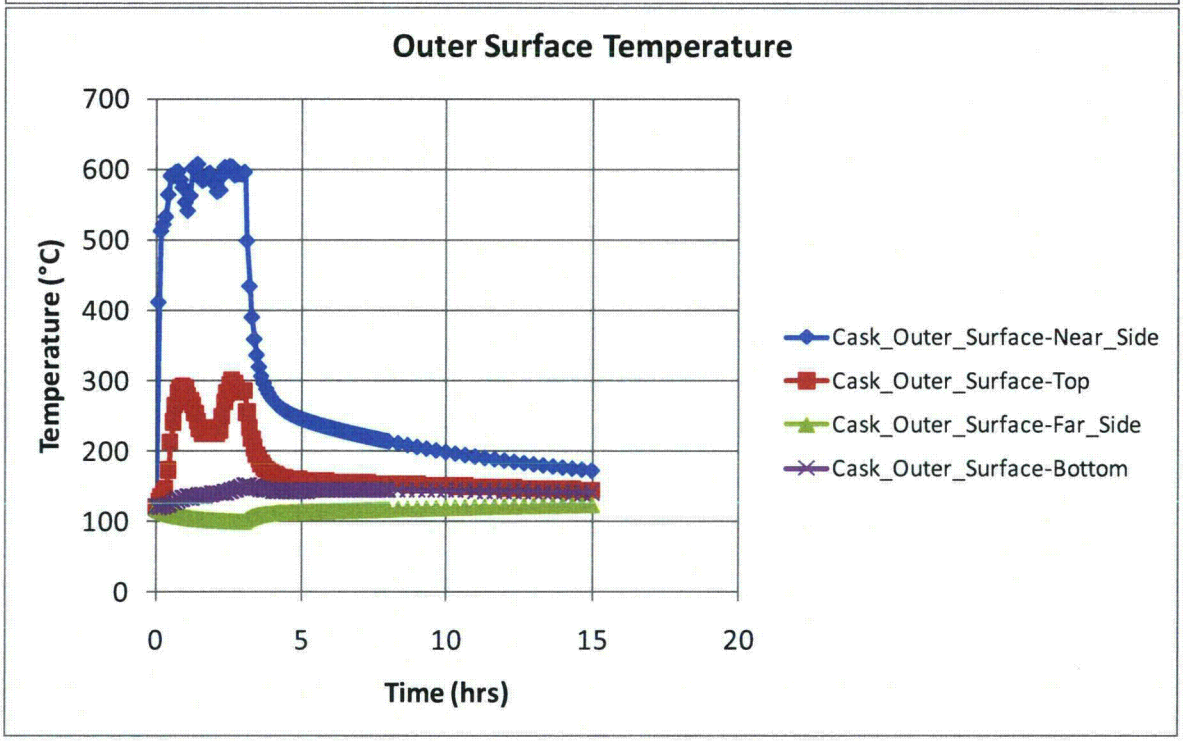

Figure D-13 Rail-Steel cask CAFE fire with cask on ground 3 m (10 feet) from the edge of the pool (continued)

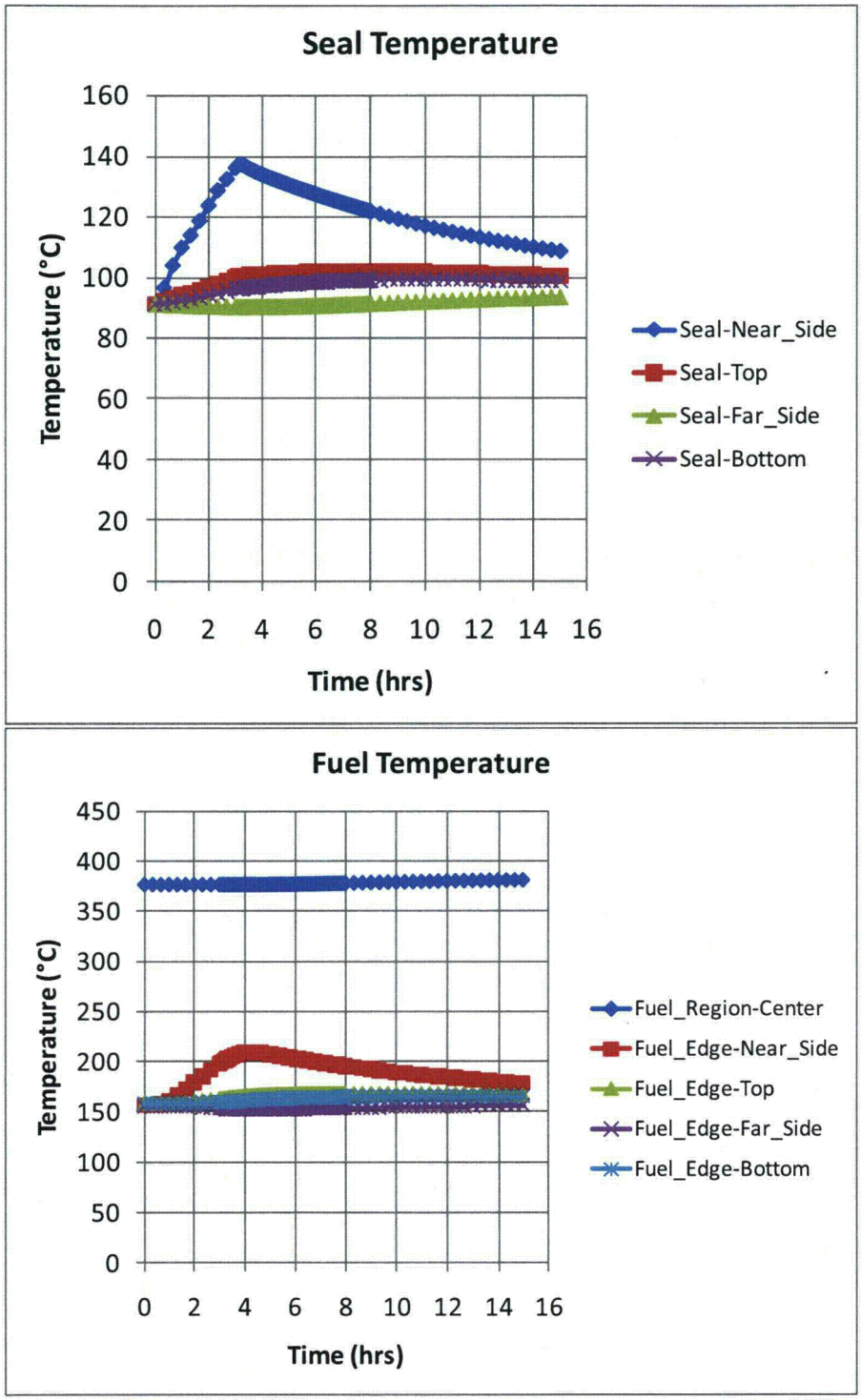

Figure D-14 Rail-Steel cask CAFE fire with cask on ground 18.3 m (60 feet) from the edge of the pool

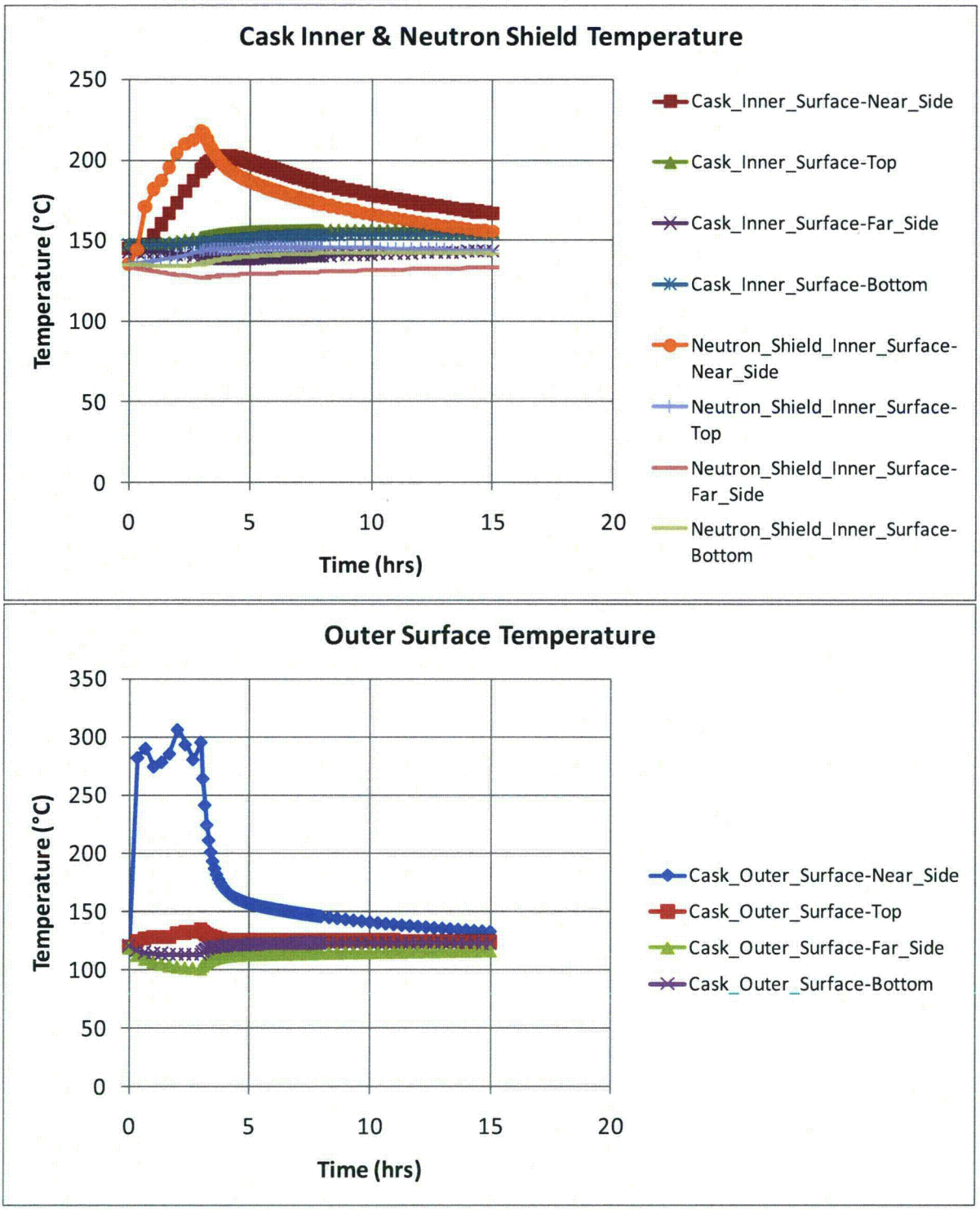

Figure D-14 Rail-Steel cask CAFE fire with cask on ground 18.3 m (60 feet) from the edge of the pool (continued)

D.4 Rail Cask with Lead Shielding

The Rail-Lead cask (NAC International, 2004) is also certified to transport SNF material on railcars. This cask is chosen because it presents quite a different design philosophy from the Rail-Steel cask. The Rail-Lead cask uses lead for the gamma shield. Moreover, the Rail-Lead cask is certified to carry SNF without a separate canister. As in the Rail-Steel cask analysis, the Rail-Lead cask is assumed to be in the horizontal configuration, as it would be during transportation, and most likely after an accident scenario. Only the thermally relevant components of the Rail-Lead cask are considered to estimate the thermal response of this cask.

The Rail-Lead cask uses a single lead gamma shield, as opposed to a multilayer carbon steel gamma shield like the one used in the Rail-Steel cask. This lead shield melts at relatively low temperatures, but remains in the overpack in molten form until the temperature is low enough to change back to the solid state. This process impacts the ability of the cask to attenuate gamma rays, as described in Chapter 5 and Appendix E. One unique feature of the Rail-Lead cask is that it can transport the SNF in a directly loaded fuel basket, in addition to inside a canister, as used in the Rail-Steel cask. The directly loaded configuration is a significant design departure from the MPC configuration since there is no barrier between the fuel assemblies and the inner walls of the overpack. For this reason, this analysis focuses on the directly loaded configuration. Finally, the Rail-Lead cask uses wood-filled impact limiters, as opposed to an aluminum honeycomb, a minor difference from the thermal analysis point of view, but nevertheless important to note.

In most cases, results reported in the Rail-Lead cask SAR (NAC International, 2004) are used but modified where necessary, as done in the Rail-Steel cask analysis. The only significant departure is how the interior of the overpack is treated in the Rail-Lead cask SAR, as explained in the introduction to this appendix. Unlike the method used in that SAR, the directly loaded basket is replaced with a cylinder having equivalent effective thermal properties using a simple, three-dimensional, finite element model and the thermal resistor network method. As done in the Rail-Steel cask analysis, the neutron shield region is replaced with an equivalent thermal region. The impact limiters are also modeled in the uncrushed state for the same reasons cited in Section D.3.1.3.

D.4.1 Geometry Considerations

The directly loaded Rail-Lead cask consists of an overpack, a fuel basket, and limiters at each end of the basket, as shown in Figure D-15. The directly loaded fuel basket is an open fuel container designed to fit snugly within the overpack interior cavity. The overpack is designed to attenuate both the heat and the neutron and gamma rays generated inside the fuel basket. The overpack contains two lids, each fitted with seals that completely seal the contents inside the overpack from the outside environment. The total length of the Rail-Lead cask, including the limiters, is approximately 6.5 m (256 in.).

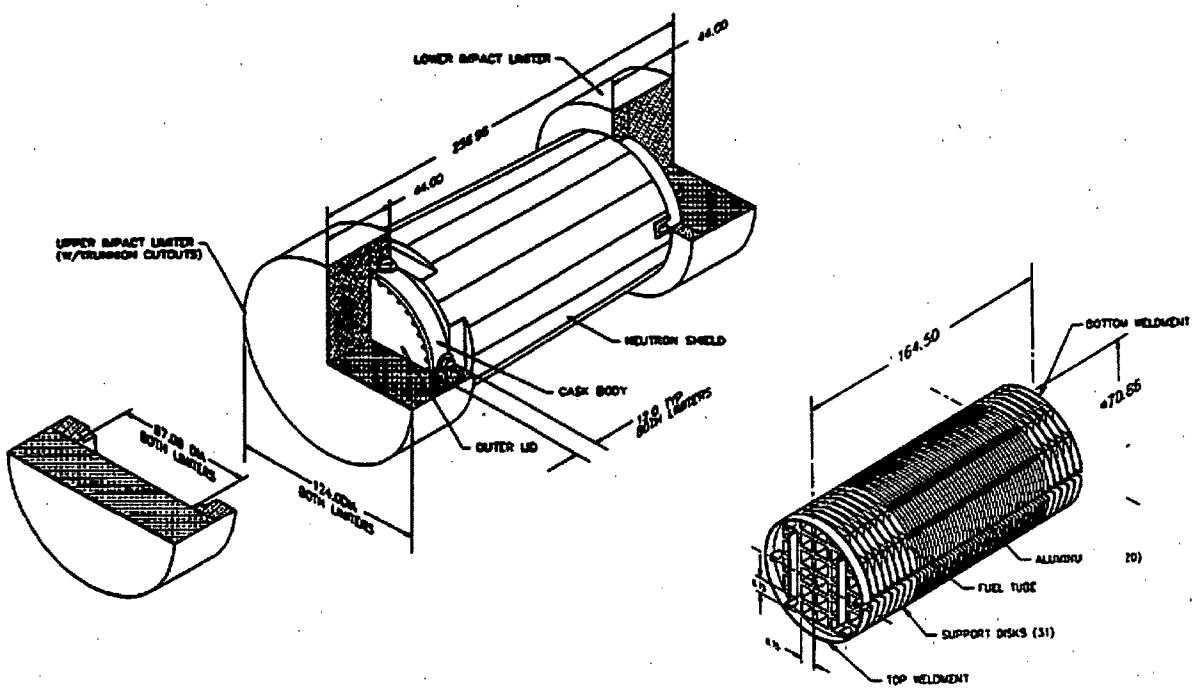

Figure D-15 Rail-Lead cask components with the directly loaded fuel basket shown to the right (from NAC International, 2004)

D.4.1.1 Overpack

The Rail-Lead cask overpack is also a multilayer cylindrical vessel approximately 2.20 m (86.7 in.) in diameter and 4.90 m (193 in.) in length (see Figure D-15). The inner cavity of the overpack is approximately 1.80 m (71 in.) in diameter and 4.19 m (165 in.) in length. The cross-section of the overpack vessel is made of three shell layers arranged in the following order starting from the center of the overpack: an inner shell, a lead shell, and an outer shell (see Figure D-16).

As in the Rail-Steel cask, these shells are tightly coupled to each other and are welded to the overpack bottom plate and top flange. The lead shell acts as the gamma shield in this design. The thickness of the inner shell wall is not constant throughout, but tapers in slightly through most of the overpack side wall. This configuration allows the thickness of the lead shell to increase slightly through the same section of the overpack, where the gamma shielding is most needed. Radial channels are also welded to the outer shell to enhance heat transfer through the neutron shield region. The outer enclosure shell is formed the same way as in the Rail-Steel cask. Similarly, the cavities formed by the outer enclosure shell, the radial channels, and the outer enclosure shell are filled with a neutron shield material. The neutron shield region increases the diameter of the overpack an additional 29.2 cm (11.5 in). Unlike the Rail-Steel cask, the overpack contains inner and outer lids that fit into the flange. Both the inner lid and bottom plate contain a 5-cm- (2-in.)-thick cylindrical layer of neutron shield within them.

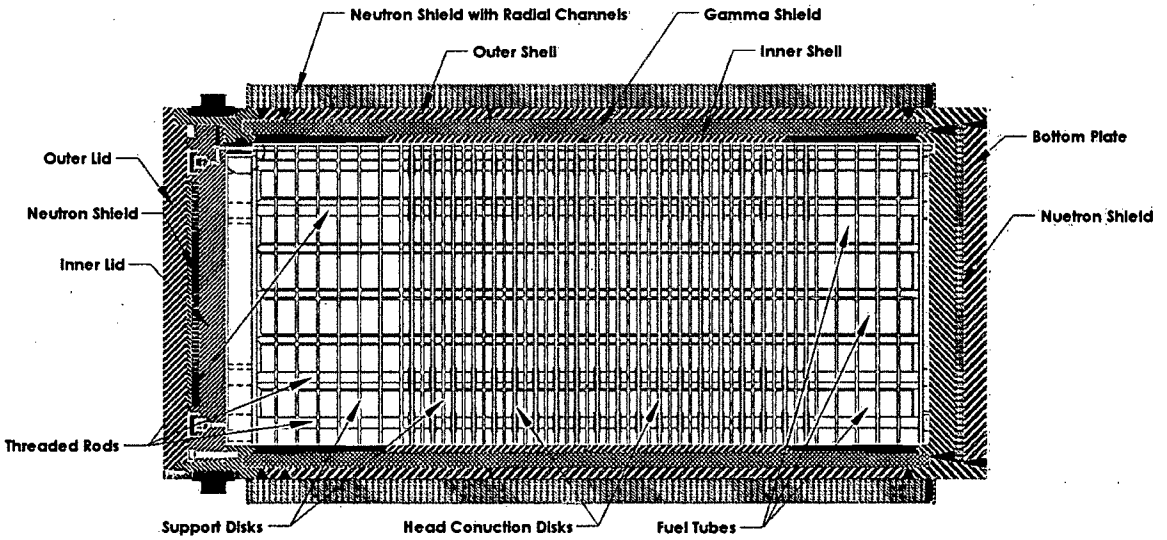

Figure D-16 Cross-section view of the Rail-Lead cask with the directly loaded fuel basket

The thermal model explicitly represents the inner, outer, and lead shells; the flange; the inner and outer lids; and the bottom plate, with minor alterations to simplify the model. The most significant change is in making the thickness of the inner shell and lead shell constant throughout. Their thickness is kept equal to the corresponding thicknesses in the middle section of the overpack. As in the Rail-Steel cask model, the neutron shield region is represented as a single volume to minimize geometric complexity. As with the Rail-Steel cask, the Rail-Lead cask overpack contains a number of features that serve a special purpose. These features are omitted from the model for the same reasons they were omitted in the Rail-Steel cask model—their effects are assumed to be either (1) negligible because of their small volume and mass relative to the other components in the overpack or (2) highly localized with no effect to the overall thermal performance of the cask at locations of interest or (3) both.

D.4.1.2 Directly Loaded Fuel Basket

In the Rail-Lead cask, the nuclear spent fuel is stored in a directly loaded basket (see Figure D-15). In this configuration, the fuel basket can store up to 26 PWR fuel assemblies. The total length of the fuel basket is 4.18 m (164.5 in.) and the diameter is a little less than the inner diameter of the overpack. The fuel basket consists of 31 support disks and 20 heat transfer disks, aligned parallel to each other, and each is precisely separated using six threaded rods and spacer nuts. The heat transfer disks are placed between the support disks in the region where the heat decay rate is at a maximum. Except for the end support disks, all support disks are the same thickness; the end support disks are twice as thick. Except for the end support disks, all heat transfer disks are slightly thicker. Both disk types contain 26 square holes spaced at regular intervals and aligned between disks. Each square hole fits a thin walled, square fuel tube that extends almost the length of the basket. These tubes are welded to the disks and accommodate the fuel assemblies. The fuel assemblies extend almost the entire length of the fuel basket. The basket's active fuel region is assumed to be 3.66 m (144 in.) in length, as suggested in the Rail-Lead cask SAR. Additional plates and a short-length cylinder are welded to the end support disks for extra support and to complete the fuel-basket design. The fuel basket fits within the inner cavity of the overpack, but a small gap exists between the basket

disks and the inner wall of the overpack and between the ends of the basket and the lid and bottom plate walls.

As in the Rail-Steel cask, each fuel assembly consists of an array of fuel rods, each separated by a helium gas space. The total number of rods in the fuel assembly, the dimensions of each rod, and the type of fuel cladding vary between assembly designs. Section D.3.1.2 more fully describes the fuel assembly and fuel rods.

The model does not explicitly include the fuel basket and fuel assemblies. Instead, a separate three-dimensional model was generated to obtain the effective properties of the basket in the in-plane and axial directions. Since the basket support disks, gas regions, and heat transfer disks repeat at regular intervals in the active fuel region, a three-dimensional, quarter solid model of a section comprising two support disks and a heat transfer disk, as well as the gas and fuel tubes between them, was generated to obtain the effective properties of the basket in the in-plane and axial directions. The diameter of the support and heat transfer disks is assumed to be the same to simplify the solid modeling and mesh process. The same model is used for the portion of the fuel basket without the heat transfer disk. In this case, the material properties and boundary conditions for the heat transfer disk are replaced with those of the gas region.

D.4.1.3 Impact Limiters

The impact limiters in the Rail-Lead cask are cylindrical wood-filled structures, also encased in a thin metal shell. Each impact limiter is 3.15 m (124 in.) in diameter and 1.12 m (44 in.) in length (see Figure D-15). The depth of the cap where the overpack fits is 30.5 cm (12 in.). These limiters serve the same purpose as the impact limiters in the Rail-Steel cask (see Section D.3.1.3). Since the impact limiters are mostly wood and have very little metal as part of their structures, they are modeled as two coupled all wood structures of the same volume and shape.

D.4.2 Rail-Lead Cask Thermal Behavior and Model Assumptions

The Rail-Lead cask is also designed to release heat passively under normal conditions of transport. In the directly loaded configuration, the basket is designed to accommodate a maximum heat load of 22.1 kW (0.85 kW per fuel assembly). Figure D-17 shows the normalized, axial heat generation rate distribution for a 0.85-kW PWR assembly. As with the Rail-Steel cask, heat is dissipated from the fuel rods to the exterior surfaces of the Rail-Lead cask by a combination of conduction, convection, and radiation heat transfer.

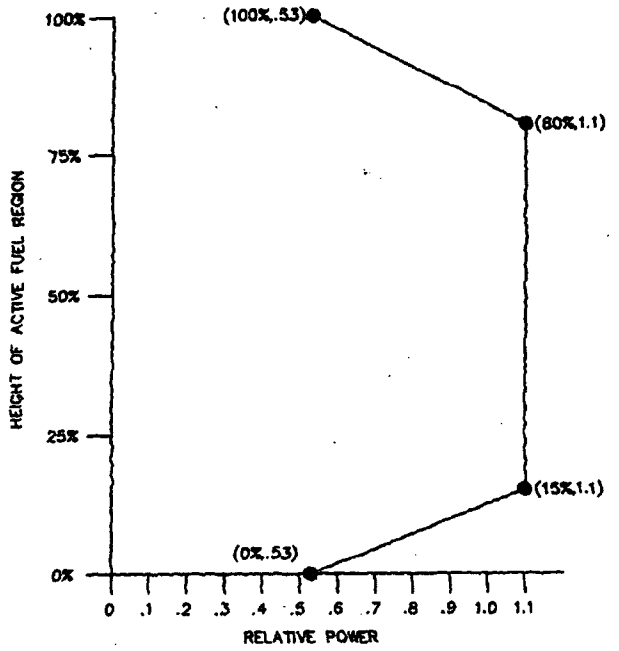

Figure D-17 Axial burn up profile for the directly loaded fuel basket (from NAC International, 2004)

The fuel assembly design in the Rail-Lead cask is conceptually the same as in the Rail-Steel cask model; therefore, the same heat transfer mechanisms are present as described in Section D.3.2. The approach described in Section D.3.3.1 is also used in the Rail-Lead cask SAR to obtain the effective thermal conductivity of the fuel assembly in the radial direction. Values presented in the Rail-Lead cask SAR are used in this study and are not much different from those used in the Rail-Steel cask SAR, as expected. Heat generated in the assembly is dissipated by conduction through the fuel tube walls. From the tubes, heat is then radially dissipated by conduction through the support and heat transfer disks and through the gas in the void formed between the tubes and the inner wall of the overpack. Radiation to the adjacent tubes and disks, and to the inner wall of the overpack, also distributes heat. As in the Rail-Steel cask fuel basket, convection is limited to a few regions around the basket perimeter. However, unlike the HI-STAR configuration, the convective cells in the Rail-Lead cask fuel basket are confined to the gas void between adjacent disks. Moreover, heat dissipated from the adjacent disks through this void tends to decrease the temperature gradient across this void region, reducing temperature-gradient-induced flow. In the Rail-Lead cask model, convection is neglected in this region since it is not expected to be significant given the Nusselt values presented in the Rail-Steel cask SAR for a similar void configuration.

Heat is dissipated radially by conduction and radiation through the gap between the disks and the overpack inner wall. This gap is assumed to be 1.65 mm (0.065 in) across, as stated in the Rail-Lead cask SAR. As mentioned before, a three-dimensional, quarter section of the fuel basket is generated to obtain effective thermal conductivities in the in-plane and axial directions (see Figure D-18). The small gap between the disks and the inner wall of the overpack is included (not visible in Figure D-18). Except for convection, this model accounts for all modes of

heat transfer, including radiation between the tubes, between the tubes and the disks, between the tubes and the inner shell (also not shown), between the disks, and between the disks and the inner shell. In the horizontal position, the disks make contact with the inner shell wall. To account for conduction through the contact area between the disks and the inner shell wall, the same method developed Rail-Steel cask is employed to enhance conductivity through the equivalent concentric gap (see Section D.3.3.2). Note that both the support and heat transfer disk diameters are assumed to be the same after thermal expansion.

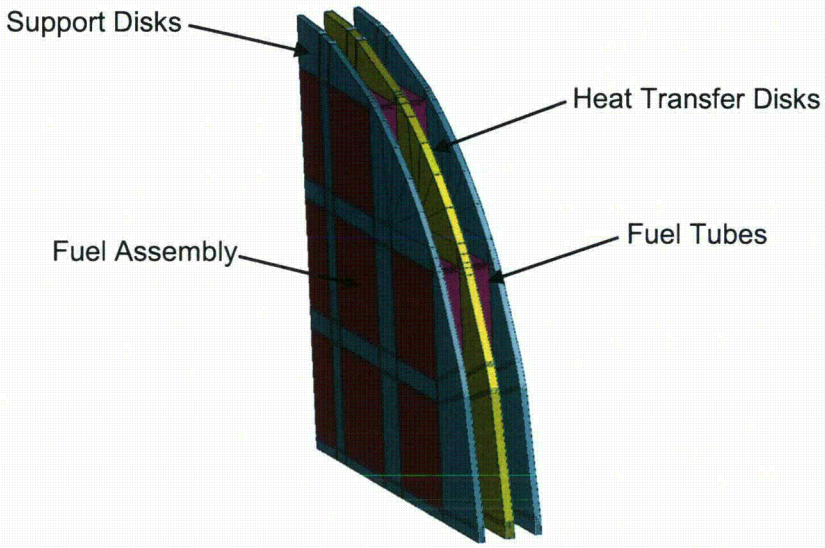

Figure D-18 Three-dimensional, quarter section of the directly loaded basket. The helium material is not shown.

Heat transfer through the inner shell, lead, and outer shell of the overpack occurs by conduction through the shell materials. These are modeled explicitly. As in the Rail-Steel cask, conduction in the neutron shield region occurs in parallel through the radial connectors and the neutron shield material.

Heat transfer from the cross-section of the directly loaded basket and overpack to the axial ends of the overpack is assumed to occur by conduction and radiation. Heat conduction occurs in parallel through each of the connecting materials that comprise the basket and overpack. The effective thermal properties are obtained in the same manner as in the Rail-Steel cask model. Radiation is assumed to occur between the end disks of the basket to the interior wall of the inner lid and bottom plate of the overpack.

The Rail-Lead cask system is also designed to maintain the temperature of critical components below their design limits during and after a 30-minute, fully engulfing HAC scenario. For fire accident scenarios lasting longer than the HAC fire described in 10 CFR 71.73, a significant amount of heat may be transferred to the interior of the cask. As in the Rail-Steel cask, the temperature of the neutron shield is expected to reach temperatures beyond its material temperature limits. Heat then is dissipated by conduction through the gas layer in the neutron shield and by radiation between the outer wall of the intermediate shell layer and the outer enclosure shell. Similarly, the lead shell is expected to melt since its melting point is around

321 degrees C (611 degrees F). The impact limiters are made of wood encased in a thin metal layer and are sealed to prevent moisture from deteriorating the wood over long periods of time. Since the impact limiters are assumed to stay intact (i.e., with the content sealed) after the initial accident event (e.g., derailment), the wood is not expected to char significantly. Therefore, this model does not take into account charring.

D.4.3 Rail-Lead Cask Materials and Thermal Properties

The Rail-Lead cask is made of stainless steel, lead, copper, aluminum, NS-4-FR, and Boral neutron absorber and is backfilled with helium. The inner and outer shell, the outer enclosure shell, the bottom plate, the top flange, and the inner lid of the overpack are made from type 304 stainless steel. The gamma shield is made from copper-lead and the outer lid from type 630 stainless steel. The radial channels are made from a combination of type 304 stainless steel, copper, and a small section of carbon steel. The stainless steel in the channel serves as the main support component, while the copper enhances conduction through the channels. The overpack neutron shield is made from NS-4-FR. The impact limiters are redwood and balsa layers encased in a thin stainless steel shell.

In the fuel basket, the support disks, threaded rods, and spacer nuts are made from type 630 stainless steel, and the top and bottom support plates, short length cylinder, and fuel tubes are made from type 304 stainless steel. The heat transfer support disks are made from aluminum alloy 6061. As with the Rail-Steel cask, adjacent to each fuel tube wall is a layer of Boral sandwiched between the tube wall and a thin layer of stainless steel sheathing. The fuel rods are assumed to be Zircaloy as in the Rail-Steel cask analysis. The pellets are made from UO_2. The empty gas space, which encompasses most of the volume inside the overpack cavity, is filled with helium.

Table D-10 through Table D-13 provide the thermal conductivity, specific heat, density, and emissivity for those materials used in the Rail-Lead cask which differ from the Rail-Steel cask or for which the properties are significantly different (see Table D-2 through Table D-5 for additional properties). The properties of NS-4-FR reported in the Rail-Lead cask SAR are marginally different from those reported for Holtite-A, as expected. The thermal conductivity of redwood and balsa vary depending on the direction of the grain. For balsa, values from the MSC Patran material database were used and compared well with values in Incropera and Dewitt (1996). Table D-10 gives the MSC Patran database references. NUREG-0361, "Safety Analysis Report for the Plutonium Air Transportable Package, Model PAT-1," issued in 1978 (U.S. Nuclear Regulatory Commission, 1978), gives values through and along the grain for redwood; however, since the Rail-Lead cask SAR does not specifically describe the arrangement of the wood layers in the limiters, average properties (along and through the grain) are assumed. The specific heat and density of copper-lead provided in the Rail-Lead cask SAR are slightly lower and higher, respectively, than for plain lead (Incropera and Dewitt, 1996); properties from the MSC Patran database are used instead since data are readily available above the melting temperature and include the specific latent heat of fusion (23.9 kilojoules per kilogram (kJ/kg) (10.3 Btu per pounds mass (Btu/lbm)). The specific heat of lead increases up to the melting point (by a factor of 1.07), but then remains approximately the same. Since these changes are small, the value at 92 degrees C (200 degrees F) is used throughout the rest of the temperature range.

Table D-10 Thermal Conductivities for the Rail-Lead Cask Materials

Material	Thermal Conductivity, W/m-°C (Btu/ft-hr-°F)				
	92 °C (200 °F)	226 °C (450 °F)	377 °C (700 °F)	477 °C (900 °F)	726 °C (1,340 °F)
Aluminum 6061*	171 (98.8)	176 (101.7)	176 (101.7)		
Copper§	402 (232.4)	386 (223.1)	376 (217.3)	369 (213.3)	352 (203.5)
Balsa¥	0.050 (0.029)	—	—	—	—
Lead‡	33.9 (19.6)	29.3 (16.9)	16.7 (9.7)	15.3 (8.8)	14.7 (8.5)
Redwood€	3.6 (2.0)	5.5 (3.1)	—	—	—
Stainless Steel Type 630*	17.5 (9.9)	18.3 (10.6)	20.7 (12.0)	24.6 (14.2)	—

* NAC International, 2004
§ Incropera and Dewitt, 1996
¥ McAdams, 1954; Perry, 1963; Weast, 1966
‡ Kelley, 1960; Schorsch, 1966; Weast, 1966
€ U.S. Nuclear Regulatory Commission, 1978

Table D-11 Specific Heat for the Rail-Lead Cask Materials

Material	Specific Heat J/kg-K (Btu/lbm-F)				
	92 °C (200 °F)	226 °C (450 °F)	377 °C (700 °F)	477 °C (900 °F)	726 °C (1,340 °F)
Copper§	390 (0.093)	406 (0.097)	422 (0.101)	431 (0.103)	451 (0.108)
Balsa¥	2,302 (0.55)	—	—	—	—
Lead‡	131 (0.031)	—	—	—	—
Redwood€	2,386 (0.57)	3,898 (0.93)	—	—	—

§ Incropera and Dewitt, 1996
¥ McAdams, 1954; Perry, 1963; Weast, 1966
‡ Kelley, 1960; Schorsch, 1966; Weast, 1966
€ U.S. Nuclear Regulatory Commission, 1978

Table D-12 Densities for the Rail-Lead Cask Materials

	Density kg/m^3 (lbm/ft^3)				
	92 °C (200 °F)	226 °C (450 °F)	377 °C (700 °F)	477 °C (900 °F)	726 °C (1,340 °F)
Aluminum 6061[*]	2,823 (176)	—	—	—	—
Copper[§]	8,933 (558)	—	—	—	—
Balsa[¥]	130 (8.1)	—	—	—	—
Lead[‡]	11,350 (709)	—	—	—	—
Redwood[€]	352 (22)	—	—	—	—

* NAC International, 2004
§ Incropera and Dewitt, 1996
¥ McAdams, 1954; Perry, 1963; Weast, 1966
‡ Kelley, 1960; Schorsch, 1966; Weast, 1966
€ U.S. Nuclear Regulatory Commission, 1978

Table D-13 Emissivity for Some of the Rail-Lead Cask Materials

Material	Emissivity
Aluminum 6061	0.22
Stainless Steel Type 630	0.58

With the exception of the basket and neutron region, all components are modeled explicitly. The impact limiters are modeled in their intact state, with properties of redwood and balsa, since the outer shell volume is significantly smaller than the total wood volume. Contact gap effects are assumed negligible. As in the Rail-Steel cask model, NS-4-FR is replaced with air when the former reaches its temperature limit, but only in the neutron shield region of the overpack. Radiation is activated in this region by setting the emissivity to the appropriate value.

D.4.3.1 Directly Fuel Loaded Basket

In the Rail-Lead cask SAR, fuel rods are evaluated to determine a representative fuel rod configuration. The fuel assembly is then modeled explicitly to obtain an equivalent in-plane thermal conductivity for the homogenized fuel assembly, as described in Section-D.3.3.1. The fuel assembly axial conductivity is next obtained with an area-weighted average using the thermal conductivities of the individual components of the fuel rods and helium. The rest of the directly loaded basket with the homogenized fuel assembly is then included explicitly in the normal condition run, but is not included in the subsequent regulatory fire accident run. Instead, the maximum temperature difference between the fuel basket and the inner wall of the overpack calculated in the normal condition run is added to the inner wall temperature of the overpack

calculated in the regulatory fire run to obtain an estimate of the temperature of the center of the fuel basket for the regulatory run. Since the Rail-Lead cask SAR did not provide homogenized properties for the fuel-basket region, this study used a different approach to obtain these properties. This alternate approach (1) reduces geometric modeling complexities while maintaining the overall response of the cask and (2) is consistent with the approach employed to model the Rail-Steel cask.

The directly loaded fuel basket is replaced with a homogenized cylinder having equivalent effective thermal conductivities in the in-plane and axial directions. As described in Section D.4.2, two variations of the same three-dimensional, quarter section, finite element model are generated. The first model included two support disks, a heat transfer disk, and the fuel tubes and helium space between the disks (see Figure D-18). The second model did not include the heat transfer disk; instead, it is replaced with helium and the boundary conditions are modified to reflect this change.

Since the Rail-Lead cask SAR did not explicitly give the effective in-plane and axial conductivities for the fuel basket (i.e., the fuel basket was modeled explicitly in that SAR), these effective conductivities are obtained using the following four-step procedure.

First, the detailed cross-section of the fuel assembly is replaced with a homogenized fuel region having equivalent thermal properties. This analysis is done in the Rail-Lead cask SAR, as explained above, and this study includes the analysis results. As expected, the thermal conductivities reported in the Rail-Lead cask SAR are close to those reported in the Rail-Steel cask SAR for similar fuel assemblies, which serves as a check. Second, the fuel tube, Boral, and stainless steel sheathing are replaced with a homogenized wall having an equivalent thermal conductivity, as described in the Rail-Lead cask SAR.

Third, both three-dimensional, quarter section models described above (and shown in Figure D-18) are used to obtain the in-plane and axial effective thermal conductivities. Each model is evaluated with two sets of boundary conditions:

(1) a uniform temperature applied over the outer circumference of the inner shell, adiabatic conditions over the in-plane ends, and uniform heat generation in the homogenized fuel assemblies

(2) adiabatic conditions applied over the outer circumference of the inner shell, a uniform temperature over one of the in-plane ends and a uniform heat flux over the other in-plane end, and no uniform heat generation in the homogenized fuel assemblies

In the first case, the in-plane thermal conductivity is obtained using the same procedure described in Section D.3.3.1. In the second case, the axial thermal conductivity is obtained using the standard relationship:

(D-6)
$$k_{eff} = \frac{qA}{L(T_q - T_t)}$$

Here A is the cross-sectional area of the basket; L is the thickness across the modeled section; q is the uniform heat flux applied over one of the cross-sectional area, axial ends; and T_t is the

uniform temperature applied over the other cross-sectional area, axial end. T_q is the average temperature where uniform heat flux is applied and is calculated using the simulation results. A second option is to apply constant (but different) temperatures at both axial ends of the basket, then calculate the total heat flow (qA) through the basket using the simulation results, and lastly calculate the effective axial conductivity using the above equation. To obtain temperature-dependent thermal conductivities, this third step is repeated a number of times using a wide range of uniform circumferential temperatures and applied heat fluxes. Fourth, the thermal conductivities obtained in the third step are added using an equivalent thermal resistor network model to obtain in-plane and axial thermal conductivities, respectively, over the entire fuel basket.

Table D-14 shows the thermal properties used for the basket. These properties are applied to the homogenized fuel-basket cylinder. The equivalent specific heat and density are obtained using a mass- and volume-weighted average, respectively, over the individual component properties. The Rail-Lead cask SAR gives the volume of each component in the fuel basket (i.e., support disks, heat transfer disks, fuel tubes).

Table D-14 Effective Thermal Properties of the Directly Loaded Fuel Basket

Effective Thermal Properties	92 °C (200 °F)	226 °C (450 °F)	377 °C (700 °F)	477 °C (900 °F)	726 °C (1,340 °F)
Radial Thermal Conductivity W/m-°C (Btu/ft-hr-°F)	3.2 (1.8)	3.8 (2.1)	4.3 (2.4)	5.0 (2.8)	5.9 (3.4)
Axial Thermal Conductivity W/m-°C (Btu/ft-hr-°F)	2.4 (1.4)	3.2 (1.8)	3.8 (2.1)	4.5 (2.6)	5.8 (3.3)
Specific Heat J/kg-°C (Btu/lbm-°F)	332 (0.079)				
Density kg/m^3 (lbm/ft^3)	2,450 (153)				

D.4.3.2 Neutron Shield Region

The neutron shield region is modeled using the same approach as that used in the SARs (NAC International, 2004; Holtec International, 2000). Both reports used the thermal resistor network method to obtain the in-plane and axial effective thermal conductivities (see Section D.3.3.4). In the case of the Rail-Lead cask, there are fewer radial channels than in the Rail-Steel cask; however, as will be demonstrated shortly, this shortcoming is compensated for by adding copper in the neutron shield region. Table D-15 shows the thermal properties used for the neutron shield region in the Rail-Lead cask. The circumferential thermal conductivity is assumed to be that of NS-4-FR. As before, the specific heat and density are obtained from a mass- and area-weighted average. Note that the thermal conductivity is slightly higher than in the Rail-Steel cask even though the Rail-Lead cask contains fewer channels. This is expected since the neutron shield in the Rail-Lead cask contains copper, which has a much higher thermal conductivity than carbon steel.

Table D-15 Effective Thermal Conductivities for the Neutron Shield Region of the Rail-Lead Cask

	92 °C (200 °F)	226 °C (450 °F)	377 °C (700 °F)	477 °C (900 °F)	726 °C (1,340 °F)
In-Plane Thermal Conductivity W/m-°C (Btu/ft-hr-°F)	8.1 (4.6)	7.9 (4.5)	7.7 (4.4)	7.7 (4.4)	7.4 (4.2)
Axial Thermal Conductivity W/m-°C (Btu/ft-hr-°F)	7.6 (4.3)	7.3 (4.2)	7.3 (4.2)	7.2 (4.1)	6.9 (3.9)
Specific Heat J/kg-°C (Btu/lbm-°F)	1,406 (0.33)	535 (0.12)	563 (0.13)	575 (0.13)	611 (0.14)
Density kg/m^3 (lbm/ft^3)	1,983 (123)	380 (23)			

D.4.4 Rail-Lead Cask Finite Element Model

The following description is short since most of the details are similar to the Rail-Steel cask analysis described in Section D.3.4. In the Rail-Lead cask runs, the cask model had 109,662 elements (see Figure D-19); this corresponds to a nominal element size of 10.2 cm (4 in.). The element count is less than in the Rail-Steel cask since the Rail-Lead cask is smaller and has fewer features which add to the element count. A mesh refinement study was also conducted with the Rail-Lead cask model with a similar outcome. The boundary conditions for the normal condition, steady-state run, the regulatory uniform-heating run, and the CAFE fire runs are the same as those discussed in Sections D.2 and D.3.4. They are not repeated here.

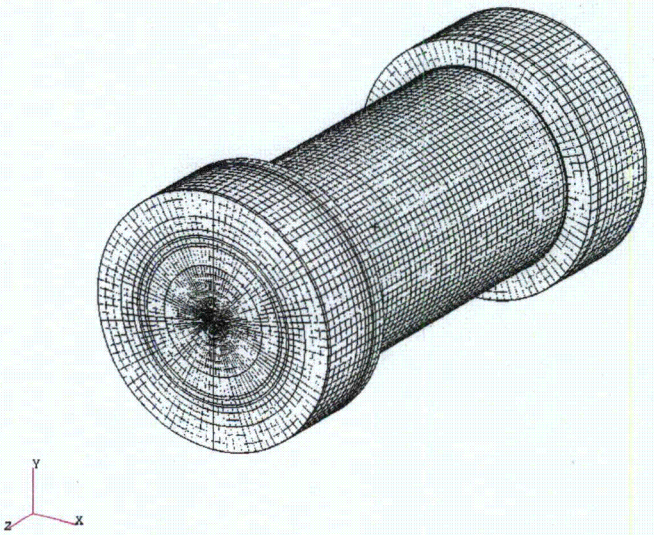

Figure D-19 The Rail-Lead cask mesh

Overall, maximum temperatures obtained using the model developed here and in the Rail-Lead cask SAR are also similar. Again, the difference in purpose of the two analyses leads to some different assumptions, which in turn leads to slightly different results.

D.4.5 Rail-Lead Cask Thermal Analysis Results

The following figures (Figure D-20 through Figure D-24) show additional results for the Rail-Lead cask not provided in Chapter 4. Figure D-20 shows results for the regulatory uniform-heating case. Recall this is a P/Thermal-only run. Figure D-21 shows results for the regulatory CAFE fire; Figure D-22 shows results for the fully engulfing CAFE fire run with the cask on the ground; and Figures D-23 and D-24 show results for the CAFE fire runs with the cask on the ground and outside the pool area. As with the Rail-Steel cask, the last three cases are run for a total of 3 hours. Chapter 4 discusses these results and their implications.

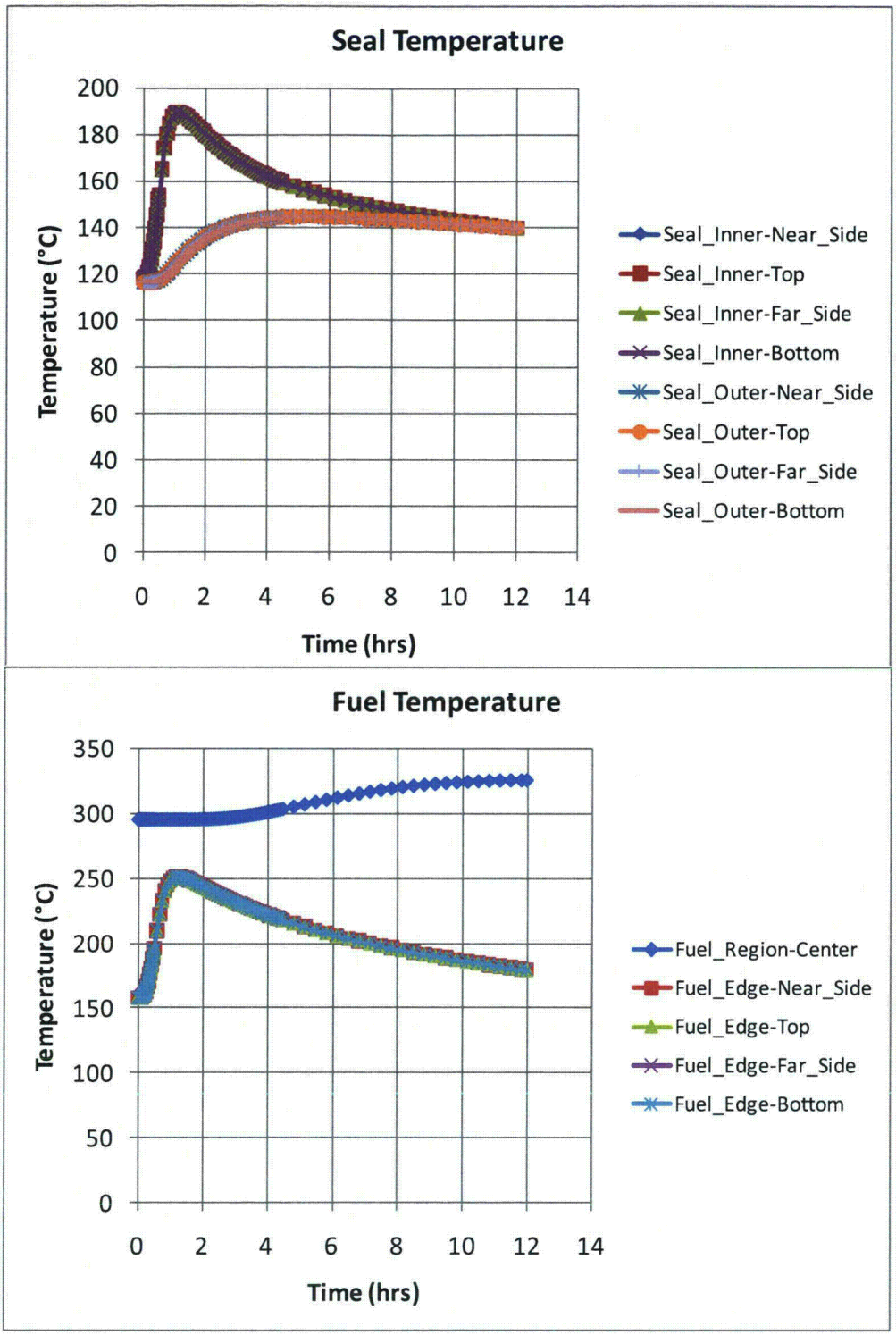

Figure D-20 Rail-Lead cask regulatory uniform-heating results

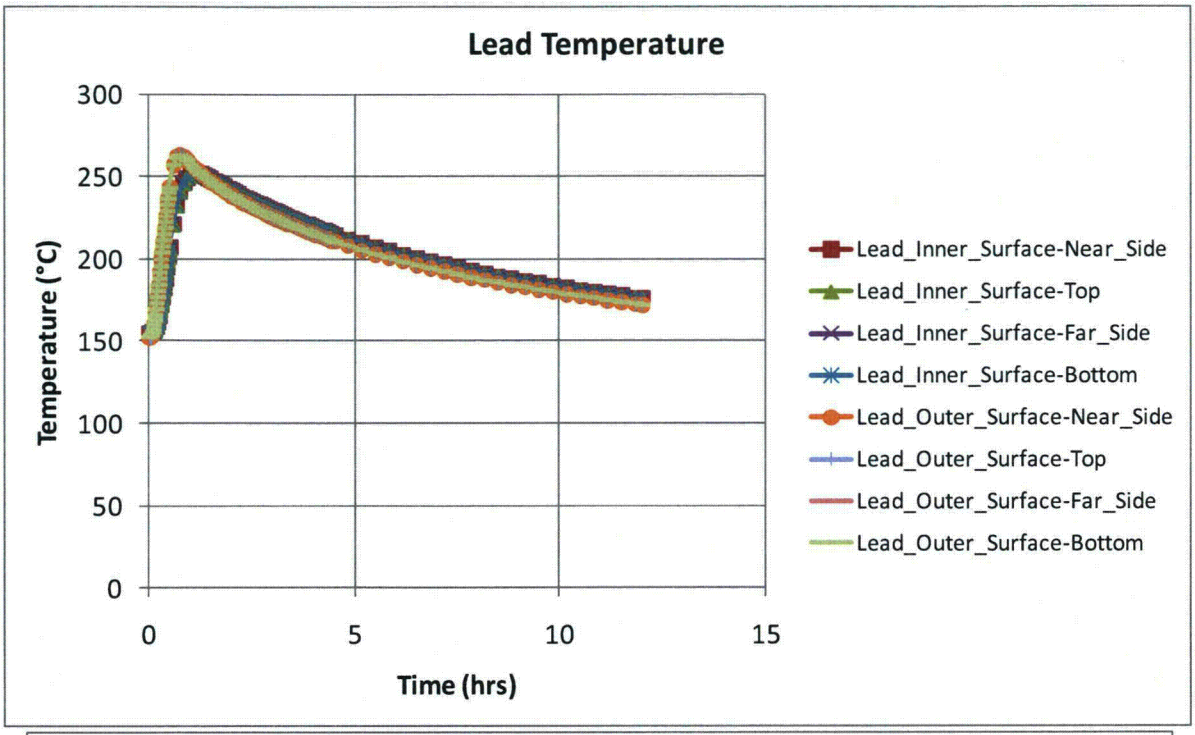

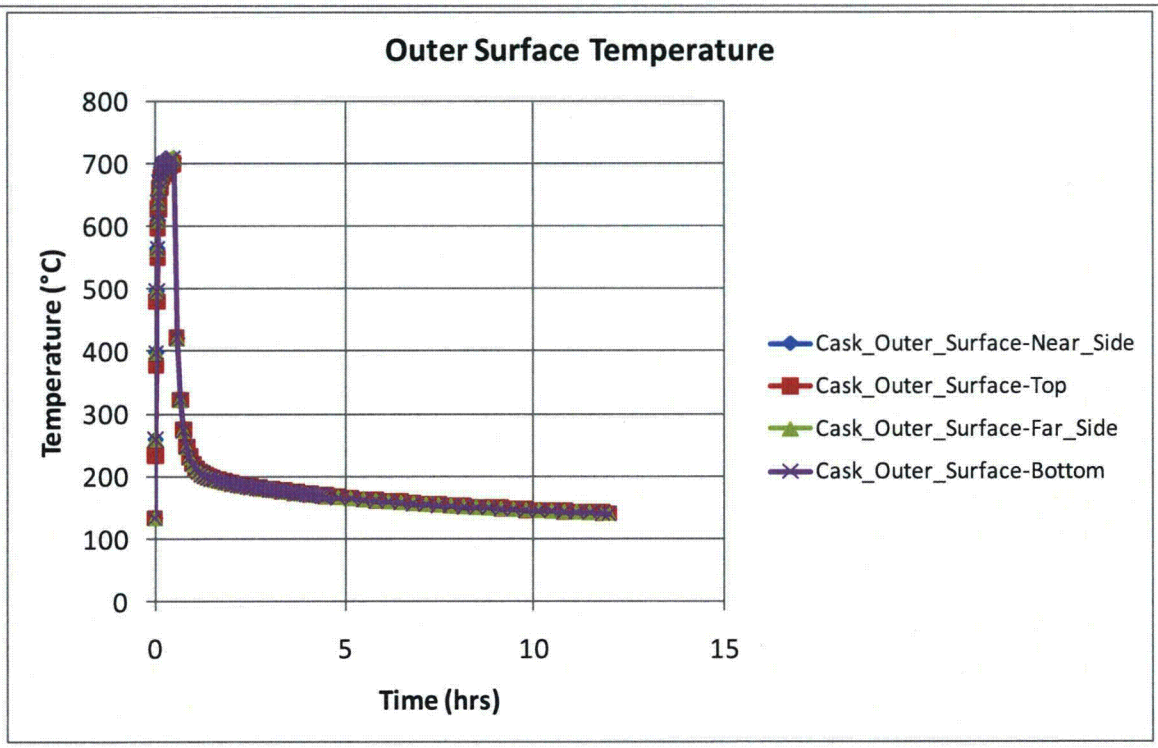

Figure D-20 Rail-Lead cask regulatory uniform-heating results (continued)

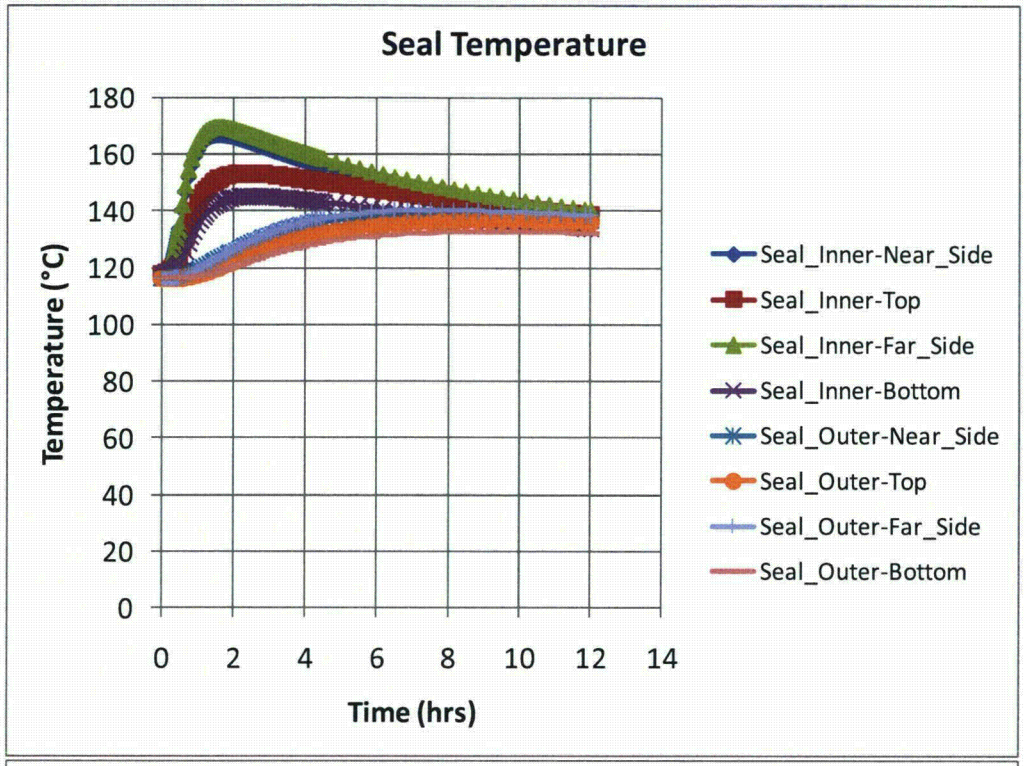

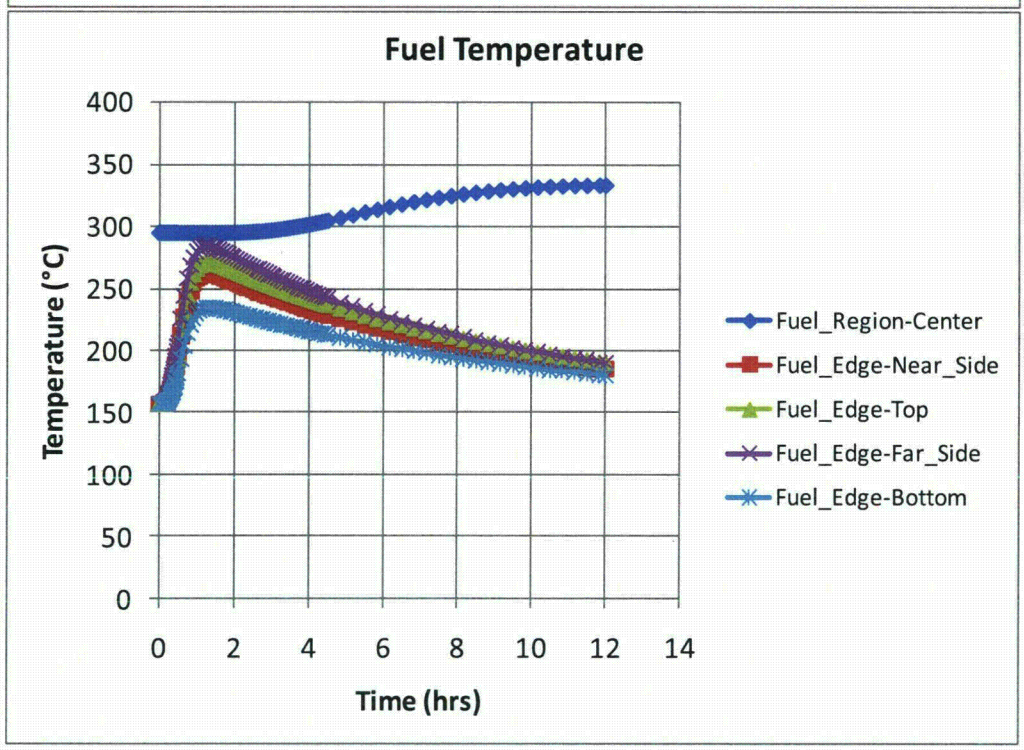

Figure D-21 Rail-Lead cask CAFE regulatory fire

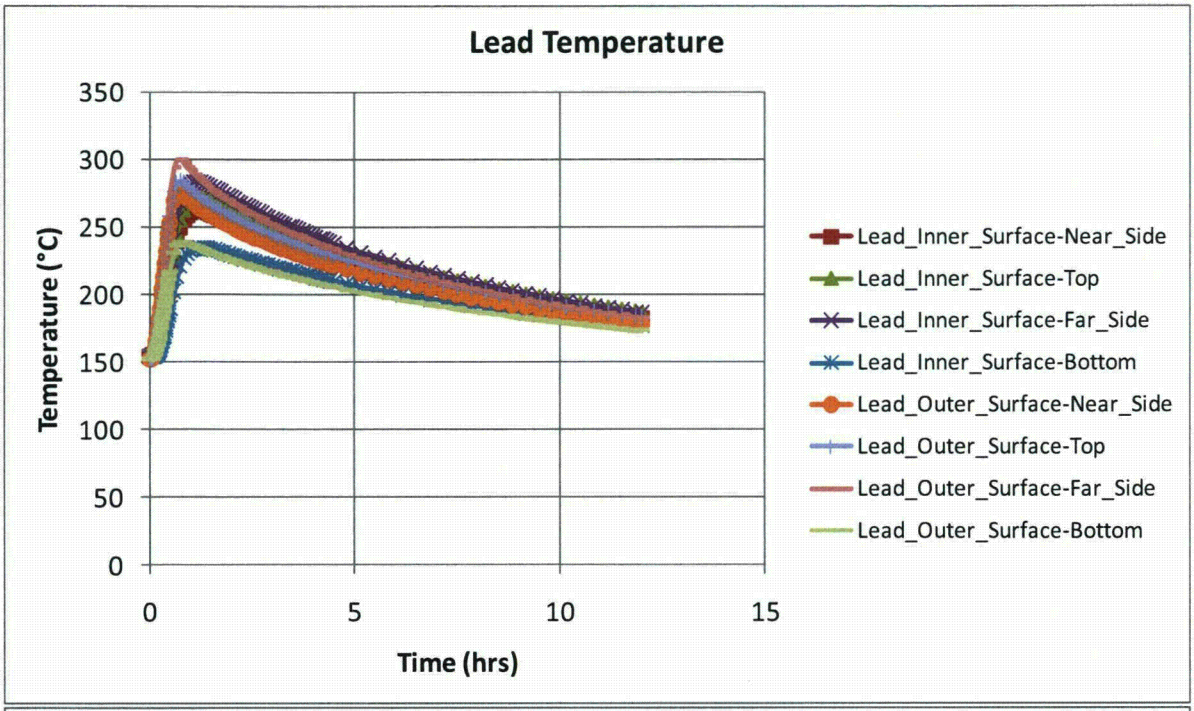

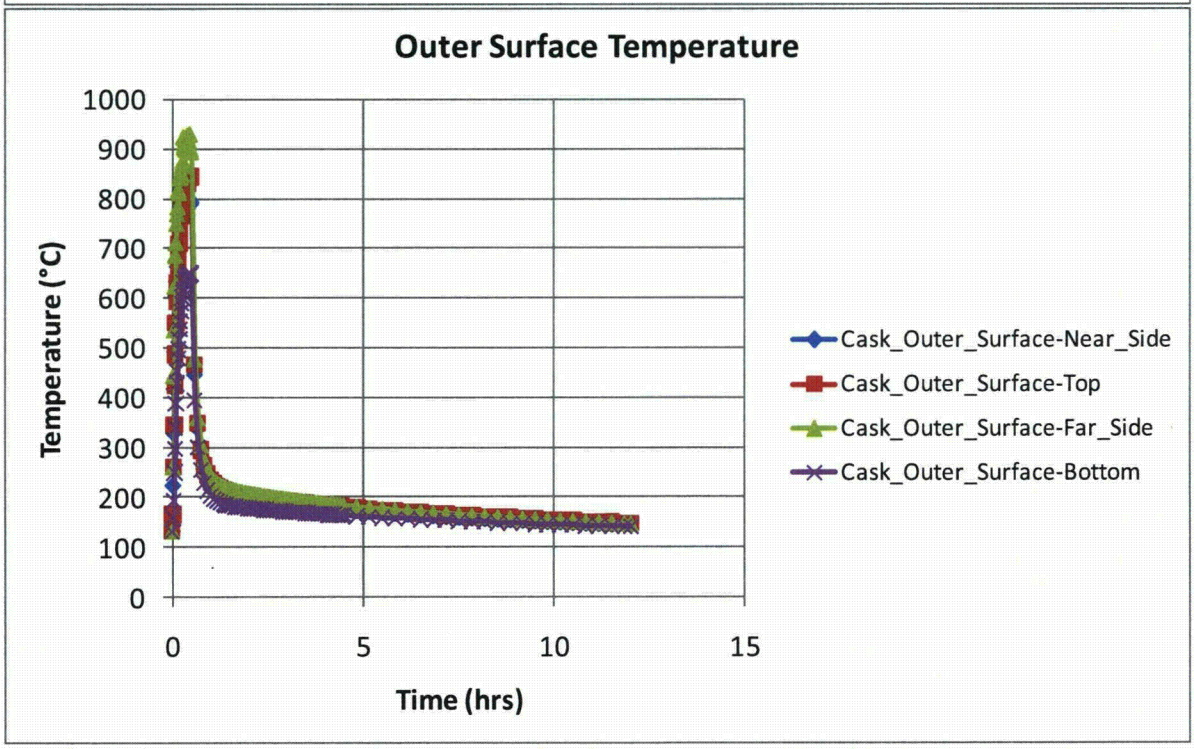

Figure D-21 Rail-Lead cask CAFE regulatory fire (continued)

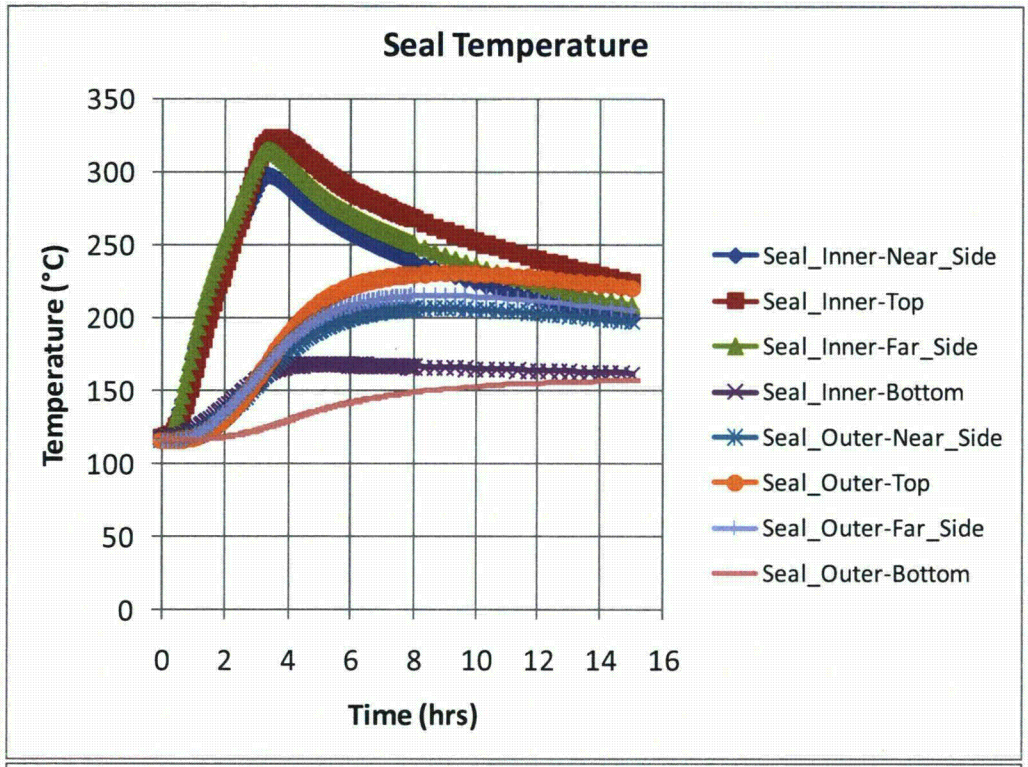

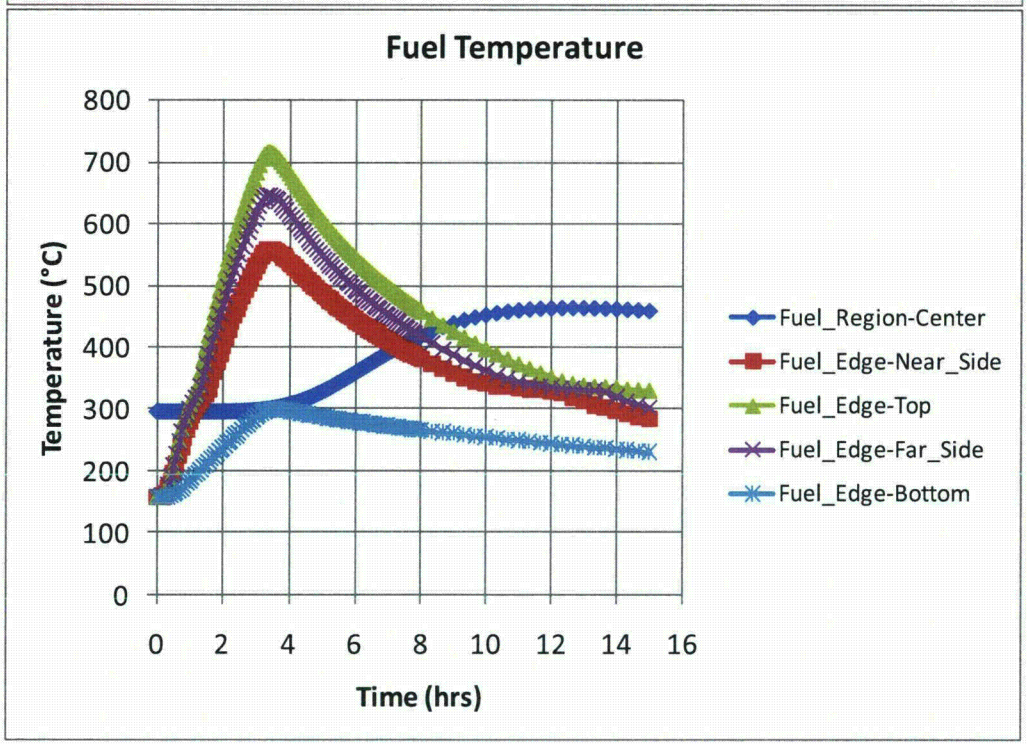

Figure D-22 Rail-Lead cask on ground at the pool center

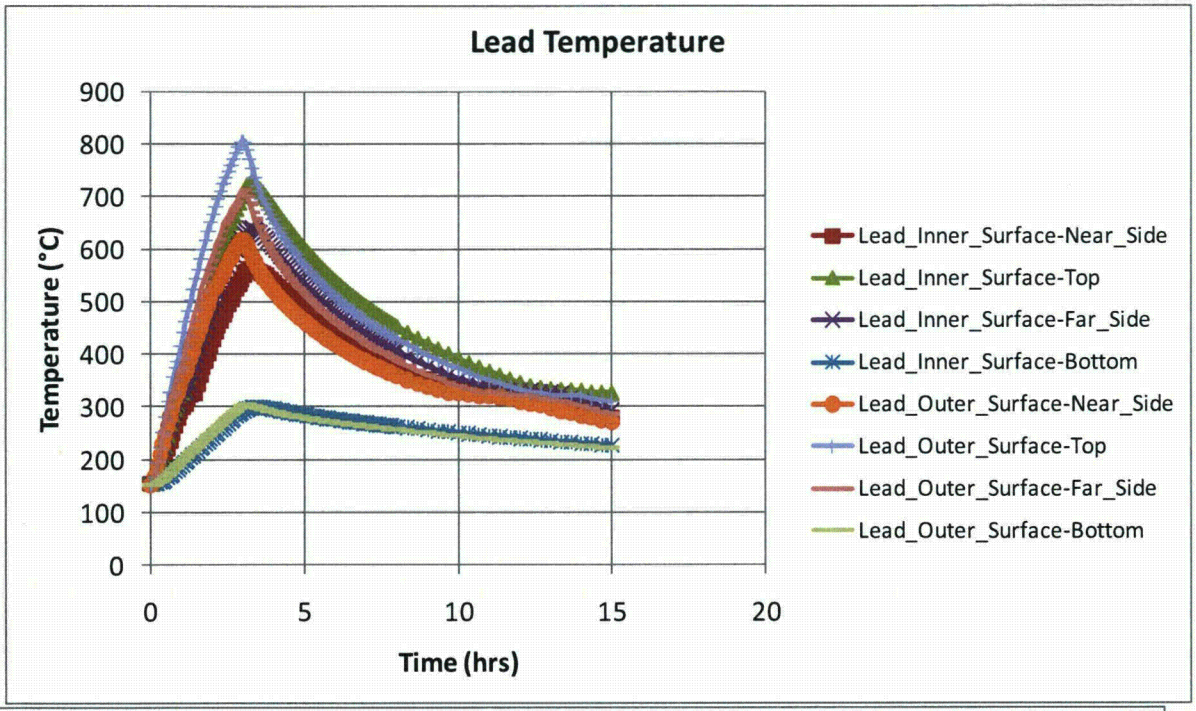

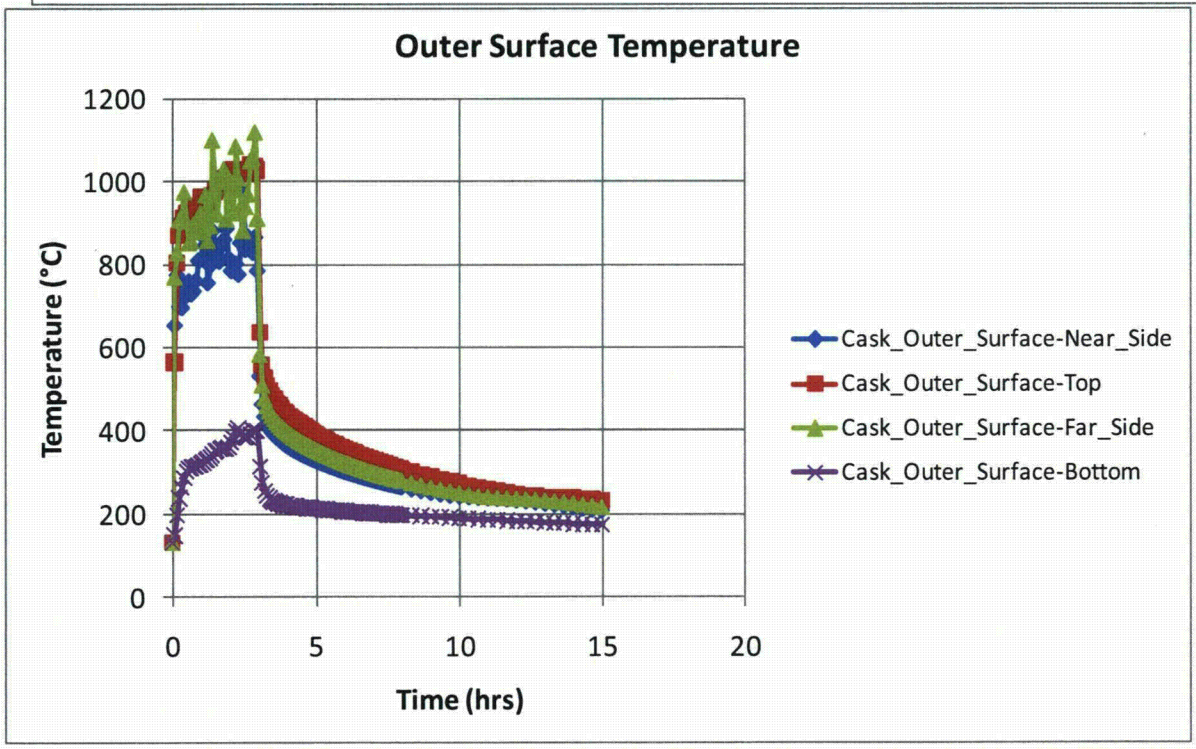

Figure D-22 Rail-Lead cask on ground at the pool center (continued)

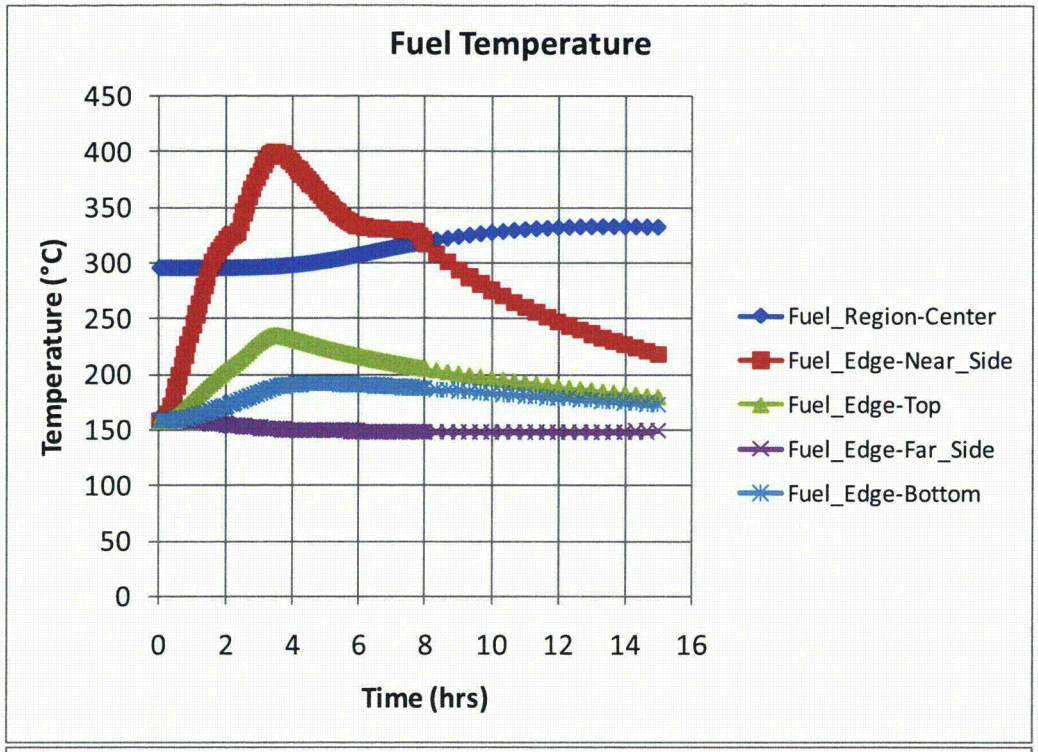

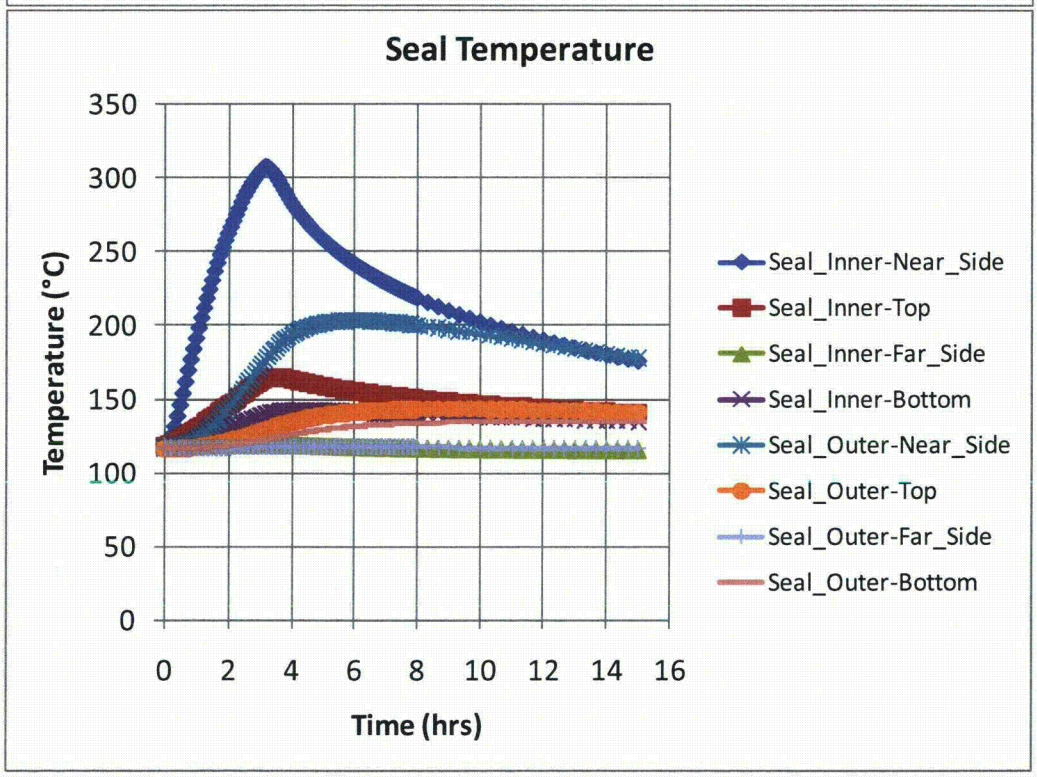

Figure D-23 Rail-Lead cask on ground 3.0 m (10 feet) from the edge of the pool

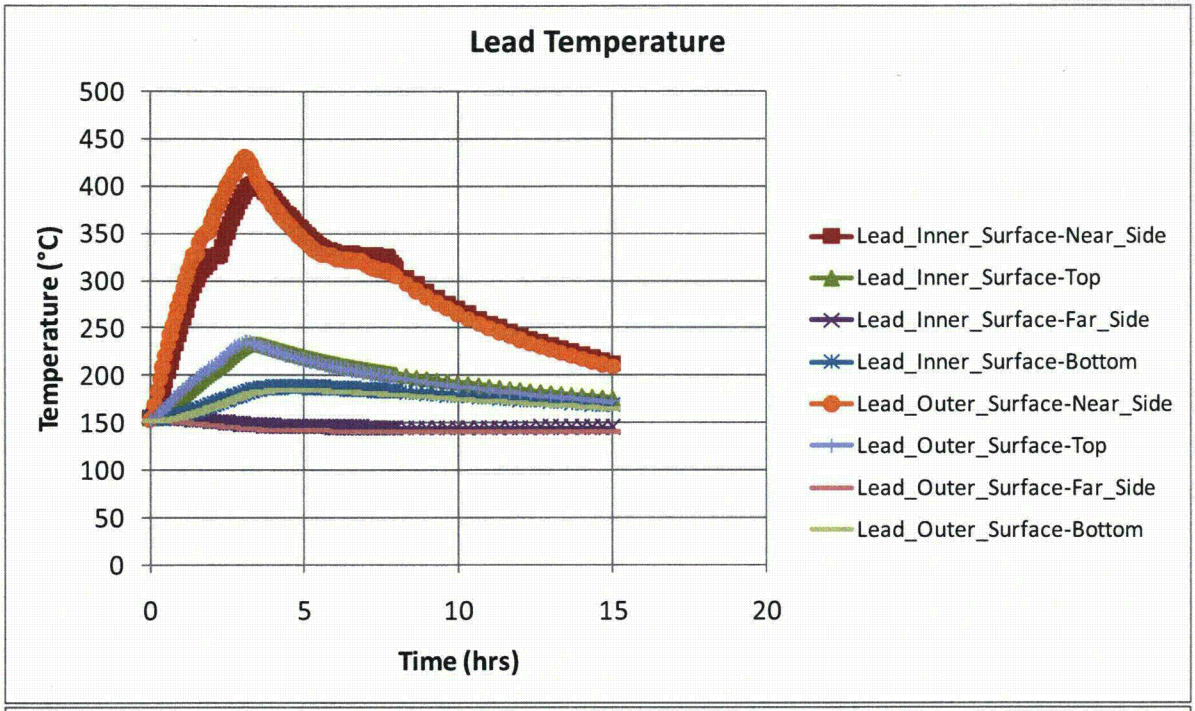

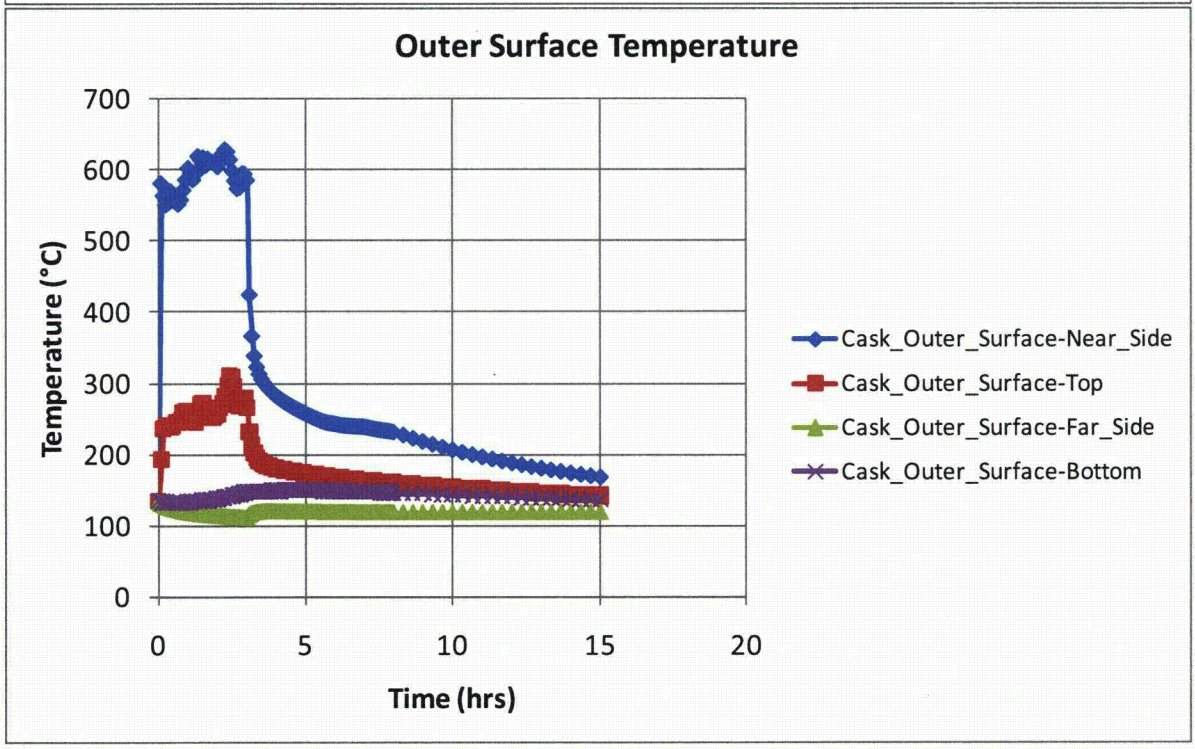

Figure D-23 Rail-Lead cask on ground 3.0 m (10 feet) from the edge of the pool (continued)

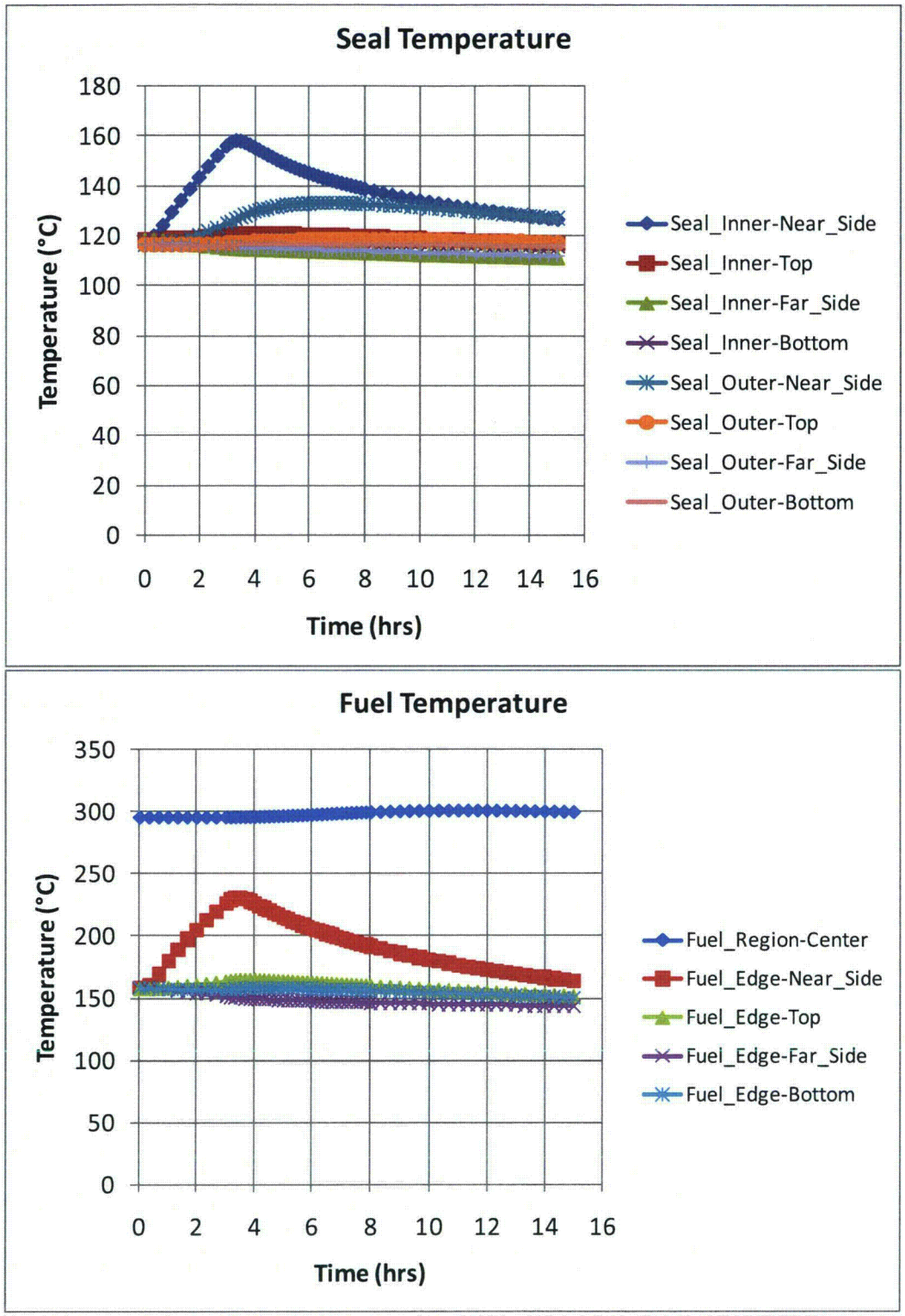

Figure D-24 Rail-Lead cask on ground 18.3 m (60 feet) from the edge of the pool

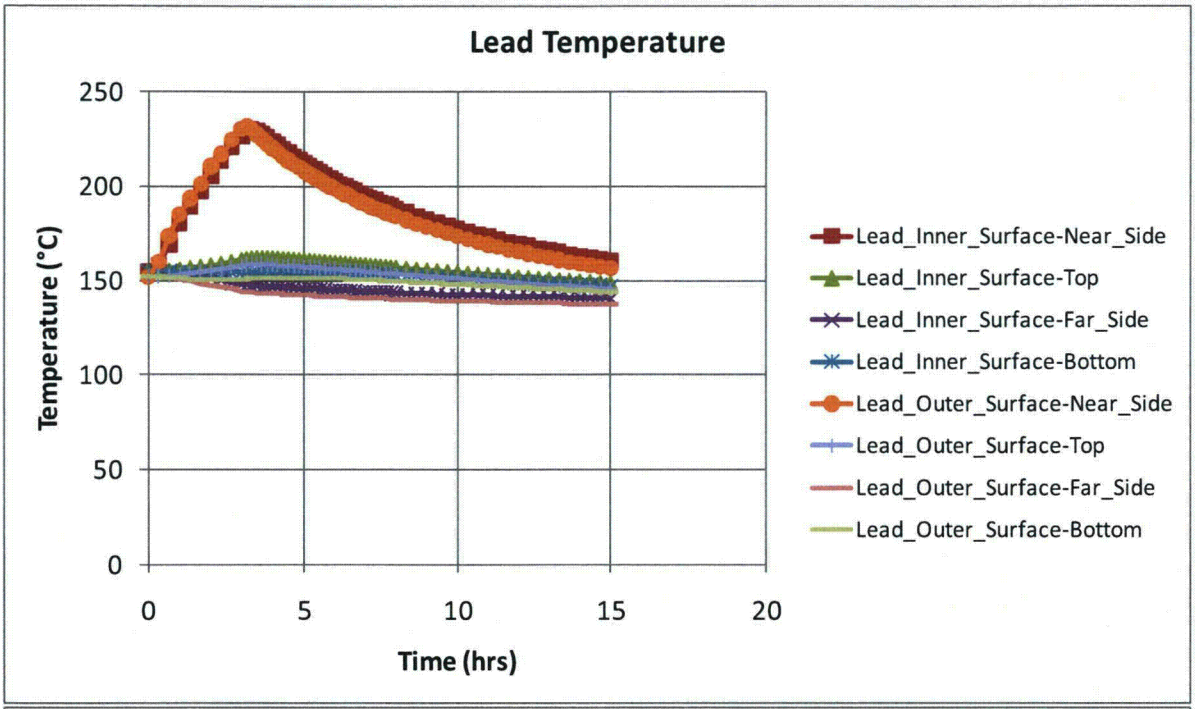

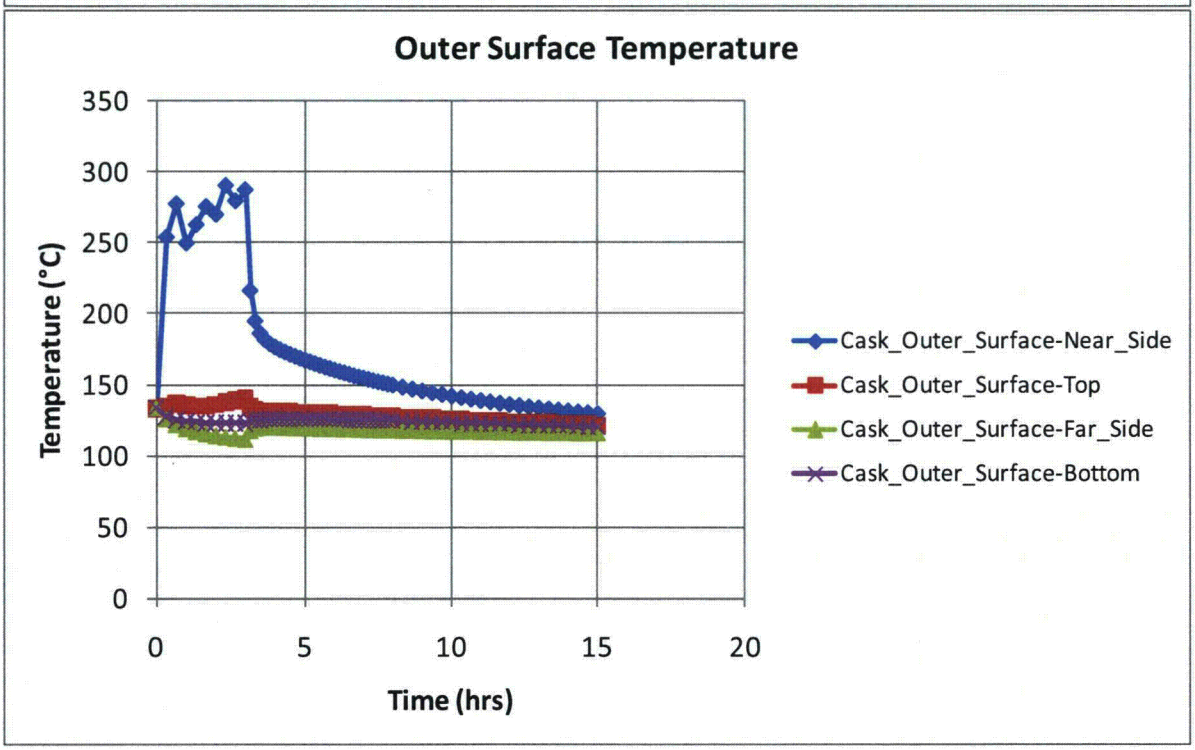

Figure D-24 Rail-Lead cask on ground 18.3 m (60 feet) from the edge of the pool (continued)

D.5 Truck Cask with Depleted Uranium

The Truck-DU cask is slightly different from the two previously analyzed casks. This cask is certified to transport up to four PWR spent fuel assemblies on a truck flat bed and uses depleted uranium (DU) for the gamma shield. In this analysis, the cask is assumed to be in the horizontal configuration, as it would most likely be after an accident scenario. For the Truck-DU cask, results reported in the Truck-DU SAR (General Atomics, 1998) are used but modified where necessary to reflect the current study.

D.5.1 Geometric Considerations

The Truck-DU consists of an overpack, a fuel basket, and limiters at each end. Like the Rail-Lead cask, the Truck-DU is a single containment cask with no MPC. Compared to the Rail-Steel and Rail-Lead casks, however, this cask is smaller in size (1.00 m (39.8 in.) in diameter at the center, 2.3 m (90 in.) in diameter at the impact limiters, and 5.94 m (234 in.) in length) since it carries only four spent fuel assemblies. Figure D-25 shows the layout of the Truck-DU cask.

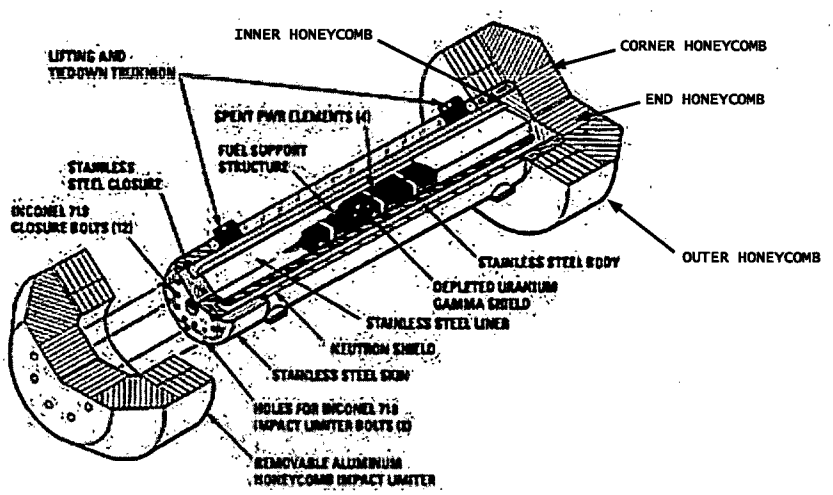

Figure D-25 Components of Truck-DU cask (from General Atomics 1998)

D.5.1.1 Fuel Assembly and Interior Cavity of the Overpack

The inner cavity of the Truck-DU is a rectangular box measuring 0.46×0.46 m (18×18 in.) in the cross-section and 4.25 m (167 in.) long. Inside this cavity, the fuel assemblies are stored within four slots formed by a steel fuel-support structure (FSS). Section D.3.1.2 discusses the details of the fuel assembly. The FSS is made from four 0.016-m (0.61-in.)-thick panels arranged in a perpendicular cross pattern. This section refers to the fuel assembly and FSS together as the fuel basket. Fuel spacers and other support structures complete the remaining space at the ends of the fuel basket. This section refers to these regions as the fuel basket ends.

In this analysis, the fuel basket and the fuel-basket end regions are each represented as single volumes to minimize geometric complexity, but their thermal response is accounted for using effective properties.

D.5.1.2 Overpack

The overpack center cross-section is made from a five-layer cross-section. The first three inner layers are square with rounded corners. The first layer, the cavity liner, is a thin steel wall (9.5 mm (0.376 in.) thick) that separates the contents of the cask from the gamma shield. The second layer is a thick wall (6.7 cm (2.6 in.) at the center of the cask) of DU which serves as the gamma shield. The third, and last square layer, is a thick wall (7.6 cm (3 in)) of steel. In the axial direction, the DU layer tapers off and extends just past the ends of the inner cavity of the overpack. The cavity liner and the thick steel wall extend almost to the axial ends of the gamma shield. The cavity liner and the thick steel wall mate with a square-shaped, steel flange at the top of the overpack and a square-shaped, metal base cup at the bottom. The inner cavity of the overpack is sealed off from the environment using a steel lid (0.28 m (11 in,) thick at the center) which fits on the flange, as shown in Figure D-25. The metal base cup is 0.24 m (9.5 in.) thick.

The last two layers, the neutron shield and the thin steel outer skin wall (1 cm (0.4 in.) thick), form the rest of the center cross-section of the overpack. The outer surface of the neutron shield layer and the outer skin wall are circular in shape. In the axial direction, the neutron shield and the outer skin wall extend the interior plane wall of the impact limiters. Both layers mate with an impact limiter support structure (ILSS) at these extreme ends. The ILSS is design to support the impact limiters using a series of ribs, 1.9 cm (0.75 in.) thick, that extend radially outward from the exterior surface of the thick steel wall to the interior surface of the outer shell wall of the ILSS. The space between these ribs and between the exterior surface of the thick steel wall and the interior surface of the outer shell wall of the ILSS is filled with a neutron shield material. In the axial direction, the ILSS extends to the end of the lid at the top and to the metal base cup at the bottom.

The thermal model explicitly represents the cavity liner, gamma shield, thick steel wall, flange, base metal cup, lid, neutron shield region, and outer skin wall, with minor alterations to simplify the model. The ILSS are represented as single volumes to minimize geometric complexity, but their thermal response is accounted for appropriately using effective properties. As with the rail casks, the Truck-DU cask overpack contains a number of features that serve a special purpose (e.g., valves, seals, trunnions). The model omits these features for the same reasons they were omitted from the rail cask models—the effects of these features are assumed to be either (1) negligible because of their small volume and mass relative to the other components in the overpack or (2) highly localized with no effect to the overall thermal performance of the cask at locations of interest or (3) both.

D.5.1.3 Impact Limiters

For the Truck-DU cask, impact limiters bolt to the top and bottom of the overpack. These impact limiters are similar to the Rail-Steel limiters in that they are made of aluminum honeycomb material encased in a thin steel shell. Figure D-25 illustrates the arrangement of the honeycomb material.

In this model, the impact limiters were assumed undamaged; hence, they are modeled using the geometry shown in Figure D-25. The encasing steel shell is neglected since the total volume of the shell is small compared to the rest of the honeycomb material.

D.5.2 Truck-DU Thermal Behavior and Model Assumptions

Like the rail casks, the Truck-DU cask is designed to release heat passively under normal conditions of transport. The Truck-DU fuel basket is designed to accommodate a maximum heat load of 2,468 W (a maximum of four fuel assemblies at 617 W per assembly). Table D-16 shows the normalized, axial heat generation rate distribution for a 617-W PWR assembly. This axial heat generation profile is applied over the active fuel region which encompasses only about 3.66 m (144 in.) of the total fuel assembly length.

Table D-16 Axial Burn up Profile in the Active Fuel Region of the Truck-DU Cask

Axial Distance from Bottom of Active Fuel (% of Active Fuel Length)	Normalized Value
0–1.4	0.432
1.4–4.2	0.630
4.2–7.6	0.847
7.6–11.1	0.964
11.1–15.3	1.09
15.3–24.3	1.22
24.3–38.9	1.22
38.9–66.0	1.09
66.0–77.9	0.964
77.9–84.7	0.847
84.7–91.7	0.630
91.7–96.3	0.432
96.3–100	0.252

As with the rail casks, heat is dissipated from the fuel rods to the exterior surfaces of the Truck-DU cask by a combination of conduction, convection, and radiation heat transfer. Heat transfer from the fuel assemblies to the outer surface of the overpack and the limiters is similar to the other rail casks. The only exception is that there are fewer large voids through the cross-section of this cask. Heat dissipation from the center cross-section of the cask is predominately by conduction and radiation through the fuel assembly and the FSS. Conduction dominates through the overpack cross-section. In the axial direction, radiation occurs between the ends of the fuel assembly and inner cavity wall. Conduction through the honeycomb material is complex; however, effective properties found in the Truck-DU cask SAR are used to obtain the thermal response of the impact limiters.

The Truck-DU cask is also designed to maintain the temperature of critical components below their design limits during and after a 30-minute, fully engulfing, HAC scenario. For fire accident scenarios lasting longer than the HAC fire described in 10 CFR 71.73, a significant amount of heat may be transferred to the interior of the cask. As in the rail casks, the temperature of the neutron shield material is expected to reach temperatures beyond its operational temperature limit. Heat then is assumed to be dissipated by conduction through a gas layer in the neutron shield region and by radiation between the outer surface of the thick steel wall layer and the inner surface of the outer skin wall.

D.5.3 Truck-DU Materials and Thermal Properties

The Truck-DU cask is made of stainless steel, DU, copper, aluminum, hydrogenous neutron absorber, Boral neutron absorber (B_4C), and helium. With the exception of spacers, bolts, and the lifting trunnions, which this analysis ignores, all major components of the overpack are made from type XM-19 stainless steel. The outer skin wall of the overpack is made from a combination of XM-19 stainless steel and copper. The stainless steel serves as the main support component, while the copper enhances conduction in the axial direction. The neutron shield material is made from a hydrogenous material which continues to function to above 149 degrees C (300 degrees F). The impact limiters are made from various density aluminum alloy materials. This study ignores the stainless steel shell (XM-11 and XM-19) encasing the honeycomb material. As with previous fuel-basket wall materials, the FSS is made from stainless steel and B_4C.

With the exception of the XM-19 stainless steel and the honeycomb material, all material properties can be found in Sections D.3.3 and D.4.3. Table D-17 and Table D-18 show the material properties used for the XM-19 stainless steel and the honeycomb material. The honeycomb material is classified by location in the limiter (see Figure D-25).

D.5.3.1 Effective Thermal Properties

Effective properties were used for the active fuel-basket region, the ends of the fuel basket, the neutron shield region, the ILSS region, and the outer skin wall (see Tables D-19 and Table D-20). These properties were obtained from the Truck-DU cask SAR (General Atomics, 1998). For the HAC scenarios, the hydrogenous neutron shield material was replaced with air above 149 degrees C (300 degrees F). Recall that radiation heat transfer was added between the outer surface of the thick steel wall layer and the inner surface of the outer skin wall to increase heat transfer to the interior of the cask during the fire (as was done in the rail cask analysis).

Table D-17 Thermal Conductivities for the Truck-DU Cask Materials

Material	Thermal Conductivity W/m-°C (Btu/hr-ft-°F)				
	92 °C (200 °F)	226 °C (450 °F)	377 °C (700 °F)	477 °C (900 °F)	726 °C (1,340 °F)
XM-19	12.3 (7.1)	15.2 (8.8)	17.0 (9.8)	18.7 (10.7)	22.8 (13.2)
Inner Honeycomb k_r/k_z	8.7/2.6 (5.0/1.5)				
Outer Honeycomb k_r/k_z	6.5/2.0 (3.8/1.2)				
Corner Honeycomb k_r/k_z	1.7/2.9 (0.98/1.8)				
End Honeycomb k_r/k_z	2.6/8.6 (1.5/5.0)				

Table D-18 Volumetric Specific Heat for the Truck-DU Cask Materials

Material	Volumetric Specific Heat (ρC_p) J/m^3-°C (Btu/ft^3-°F)
XM-19	4,287,264 (63.9)
Inner Honeycomb	155,300 (2.3)
Outer Honeycomb	117,000 (1.7)
Corner Honeycomb	39,290 (0.58)
End Honeycomb	155,300 (2.3)

Table D-19 Effective Thermal Conductivities for the Truck-DU Cask Materials

Material	Thermal Conductivity W/m-°C (Btu/hr-ft-°F)				
	92 °C (200 °F)	226 °C (450 °F)	377 °C (700 °F)	477 °C (900 °F)	726 °C (1,340 °F)
Active Fuel Region k_r/k_z	1.2/4.5 (1.0/3.8)	1.8/4.9 (1.5/4.2)	2.3/5.2 (2.0/4.4)	2.8/5.7 (2.4/4.9)	4.9/7.3 (4.2/6.2)
Fuel Region Ends k_r/k_z	0.28/3.3 (0.24/2.8)	0.31/3.8 (0.26/3.2)	0.33/4.1 (0.28/3.5)	0.35/4.6 (0.30/3.9)	0.40/6.3 (0.34/5.3)
Neutron Shield Region k_r/k_z	1.7/0.15 (1.5/0.12)				
ILSS $k_{r\_bottom}/k_{r\_top}/k_z$	2.2/3.9/0.85 (1.8/3.3/0.72)	2.8/4.9/1.0 (2.3/4.1/0.85)	3.2/5.6/1.2 (2.7/4.8/1.0)	3.5/6.1/1.3 (3.0/5.2/1.1)	4.2/7.5/1.5 (3.6/6.4/1.3)
Outer Skin Wall k_r/k_z	12.2/41.5 (10.4/35.4)	15.2/44.0 (13.0/37.5)	17.0/45.5 (14.5/38.8)	18.6/47.0 (15.9/40.0)	22.8/50.3 (19.4/42.9)

Table D-20 Effective Volumetric Specific Heat for the Truck-DU Cask Materials

Material	Volumetric Specific Heat (ρC_p) J/m^3-°C (Btu/ft^3-°F)
Active Fuel Region	938,700 (25.2)
Fuel Region Ends	1,263,000 (33.9)
Neutron Region	1,715,000 (46.0)
ILSS	1,225,000 (32.8)
Outer Skin Wall	3,882,000 (104.2)

D.5.4 Truck-DU P/Thermal Finite Element Model

In the Truck-DU runs, the cask model had 241,700 elements (see Figure D-26). The element count is higher than in the rail cask analysis since the Truck-DU has a number of smaller features that add to the element count. The boundary conditions for the normal condition, steady-state run; the regulatory uniform-heating run; and the CAFE fire run are the same as discussed in Sections D.2 and D.3.4. In this analysis, the fire is run for only 1 hour. This timeframe corresponds to the total fuel burning time for the maximum-capacity, fully loaded fuel tanker truck.

Overall, maximum temperatures obtained in the normal condition, steady-state run and in the regulatory uniform-heating case using the model developed for this study are similar to the results presented in the Truck-DU cask SAR. Again, the difference in purpose of the two analyses leads to some different assumptions, which in turn leads to slightly different results.

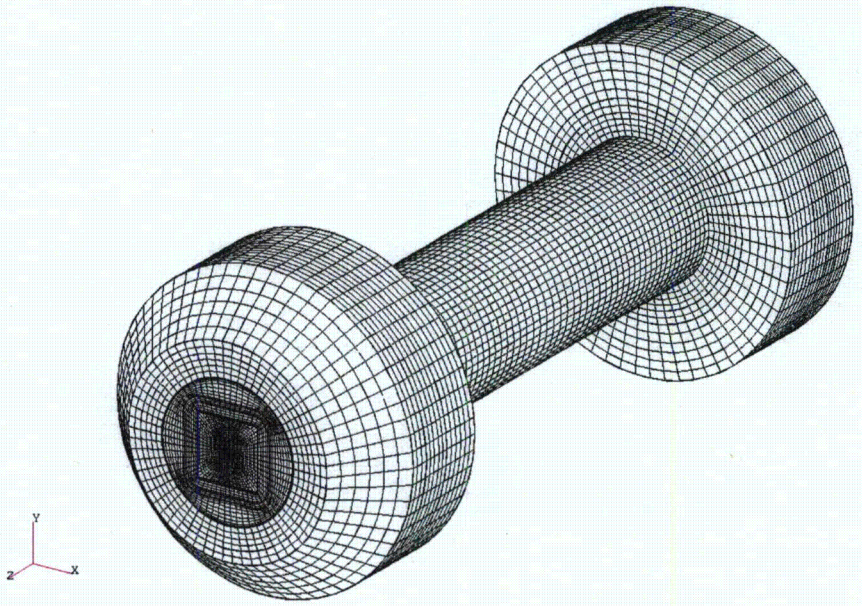

Figure D-26 Truck-DU cask mesh

D.5.5 Truck-DU Cask Thermal Analysis Results

For the Truck-DU cask, only one CAFE nonregulatory fire was run—the cask on ground and at the center of the pool (see Figure D-27). This is the most severe case, as demonstrated in the Rail-Steel and Rail-Lead cask analyses. Figure D-28 shows additional results for this case not provided in Chapter 4. A discussion of these results and their implications is provided in Chapter 4.

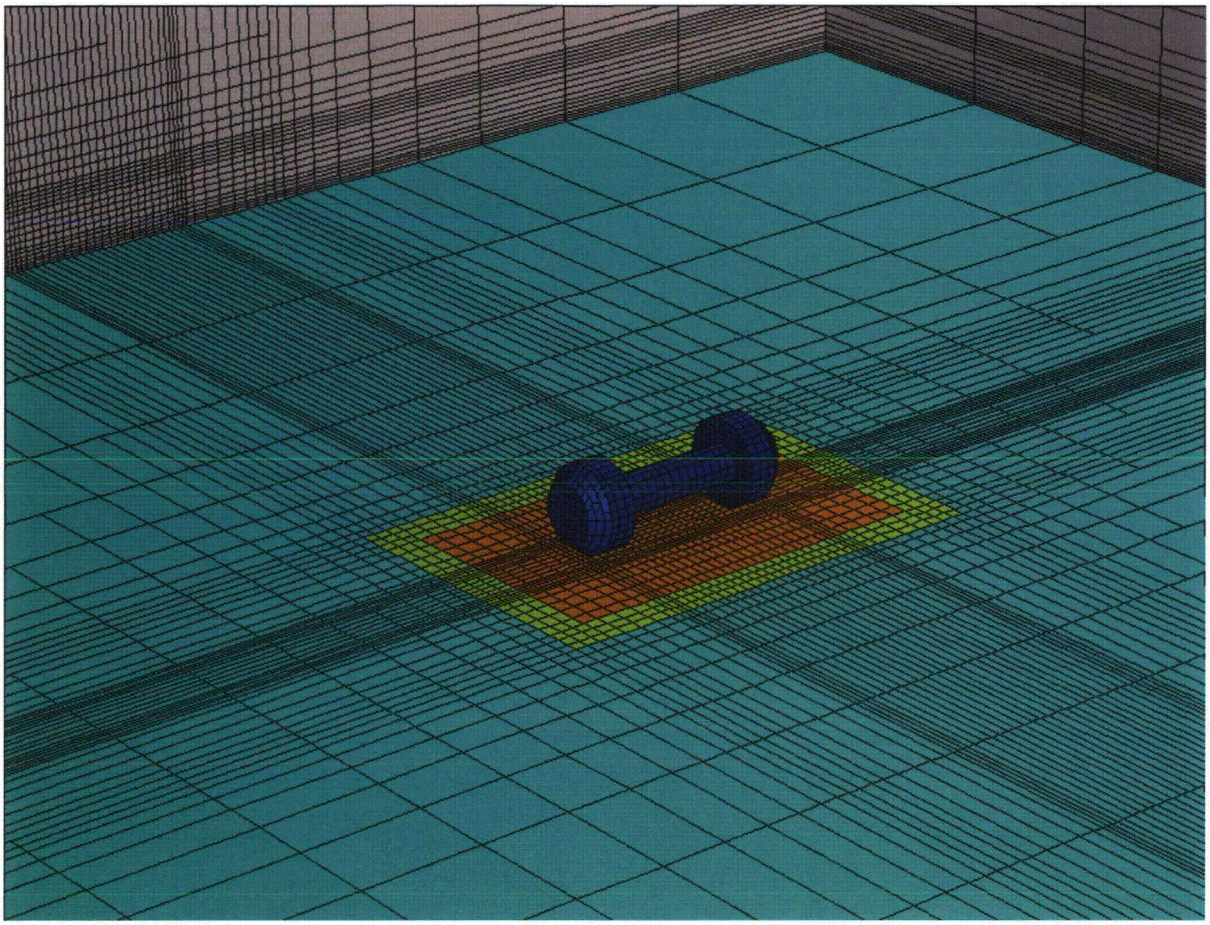

Figure D-27 CAFE three-dimensional domain with Truck-DU cask on ground

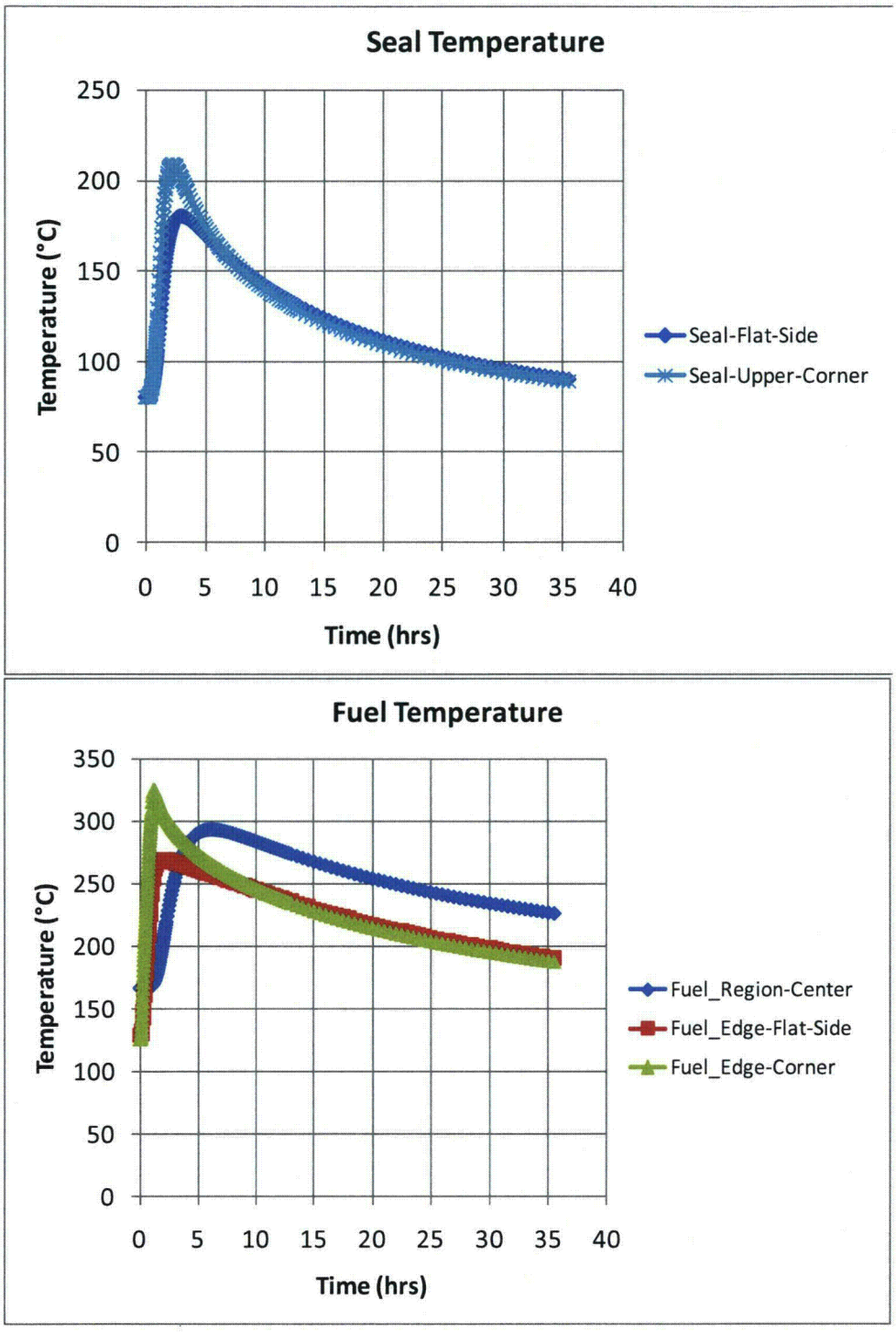

Figure D-28 Truck-DU cask on ground at the pool center

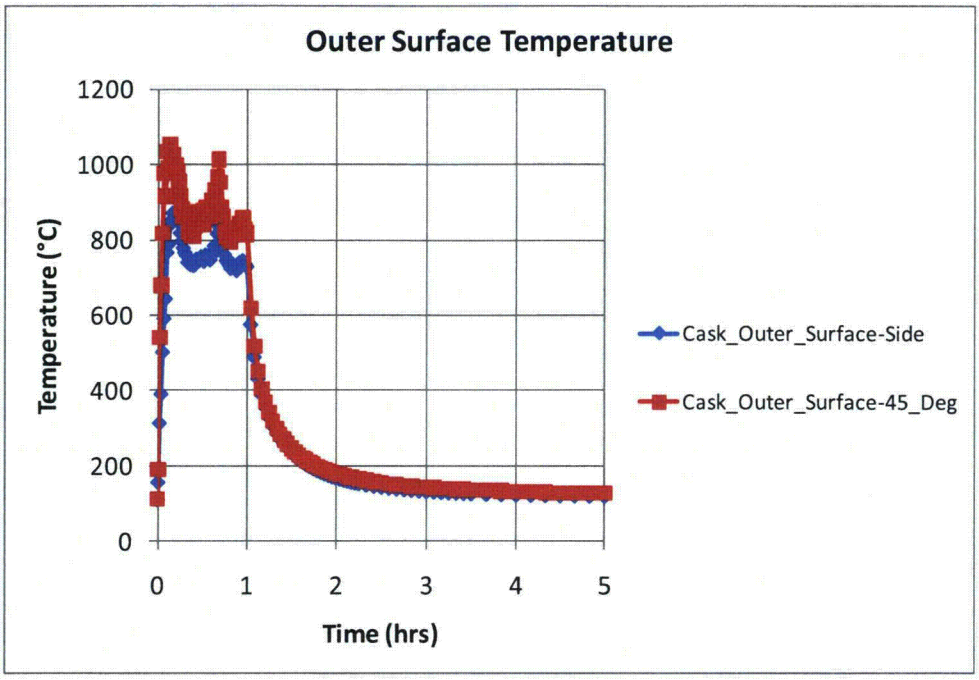

Figure D-28 Truck-DU cask on ground at the pool center (continued)

D.6 Container Analysis Fire Environment Benchmark

Large, fully engulfed objects have a great impact on the surrounding fire environment. To adequately predict incident heat flux to casks, computational fluid dynamics models must be employed with appropriate boundary conditions. Also, because of the impact that massive objects have on fires, computational fluid dynamics models must be validated against experimental data from tests that have similar size objects (Nicolette and Larson, 1989).

Since the development of the CAFE code (del Valle, et. al., 2009; del Valle, 2007; Are, et.al., 2005; Lopez, et. al., 2003), there has been a continuing effort to benchmark and fine tune this fire model by making use of relevant empirical data from experiments. Continuing with this effort, before running the cases described in Chapter 4, CAFE is benchmarked against experimental data obtained from two fire test series conducted at Sandia National Laboratory's Lurance Canyon Burn Site: (1) one using a large calorimeter in the center of the pool (Greiner, 2009; Kramer, 2008) and (2) the other using a smaller diameter calorimeter adjacent to the fire (Lopez et. al., 2003). The large calorimeter is close to the size of the casks analyzed in this study and had a test setup and conditions that closely matched the regulatory hypothetical fire accident scenario outlined in 10 CFR 71.73 for certification of SNF transportation casks. The smaller diameter calorimeter test is used to benchmark CAFE's ability to predict heat flux to objects outside the fire plume. This section briefly describes these experiments and shows benchmark results.

D.6.1 Large Calorimeter Test and Benchmark Results

The large calorimeter is a carbon steel cylindrical pipe approximately 2.43 m (96 in.) in diameter and 4.6 m (180 in.) in length, with nominal 2.54-cm- (1-in.)-thick walls, and had bolted lids on each end (see Figure D-29(a)). The calorimeter is placed on two stands at the center of a 7.93-m- (26-ft)-diameter fuel pool. The stands maintained the calorimeter 1 m (39.4 in.) above the fuel surface. Approximately 7,500 liters (2,000 gallons) of JP8 are used for each test. Total burn time varies with each test, but is at least 25 minutes. All tests are conducted in relatively low wind conditions (less than 5 m/s (11 mph)) to ensure that the calorimeter is fully or partially engulfed (see Figure D-29(b)).

Thermocouples (TCs) are installed on the interior walls of the calorimeter to measure interior surface temperatures. All TCs are installed in a ring configuration as shown in Figure D-30. Heat flux gages are placed just outside the round walls of the calorimeter in a ring configuration and outside the lids to measure incident heat fluxes close to the outer walls of the calorimeter. Fuel burn rates are measured using a TC rake—a linear array of TCs traversing the depth of the fuel layer at known distance intervals. Directional flow probes are installed just outside of the calorimeter walls to measure the flow speed of hot gases near the calorimeter walls. Finally, ultrasonic sensors placed on four towers—two sensor towers aligned with the calorimeter lids and two sensor towers perpendicular to the cylindrical section of the calorimeter, but on opposite sides—are used to measure windspeed and wind direction. Each tower is approximately 24.4 m (80 feet) from the center of the pool and has three ultrasonic sensors placed 2, 8 and 10 m (6.5, 26.2, and 32.8 feet) from the ground.

(a) (b)

Figure D-29 Large calorimeter fire test: (a) test setup and (b) fire fully engulfing the calorimeter

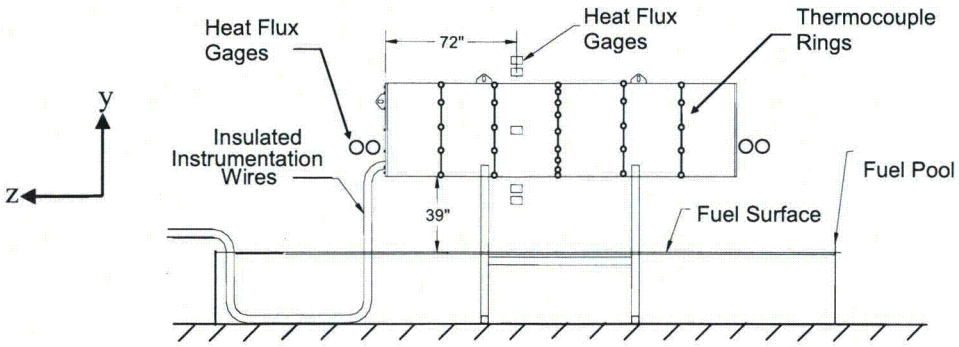

Figure D-30 Side view (looking from the north) of calorimeter and test setup. Note: The calorimeter is centered with the pool. This drawing is not to scale.

Figure D-31a shows average temperatures along the four circumferential sides of the calorimeter obtained from Test 1 and from the CAFE benchmark run. Data from Test 1 were chosen because the wind conditions and fire characteristics of this test best matched the regulatory conditions specified in 10 CFR 71.73 and the fire scenarios analyzed in this study. The test readings were taken from TCs located at 0 degrees (north side; that is, pointing out of the page), 90 degrees (top side), 180 degrees (south side; that is, pointing into the page), and 270 degrees (underneath). This plot illustrates that average temperature predictions obtained from CAFE envelop the average temperatures readings from the test.

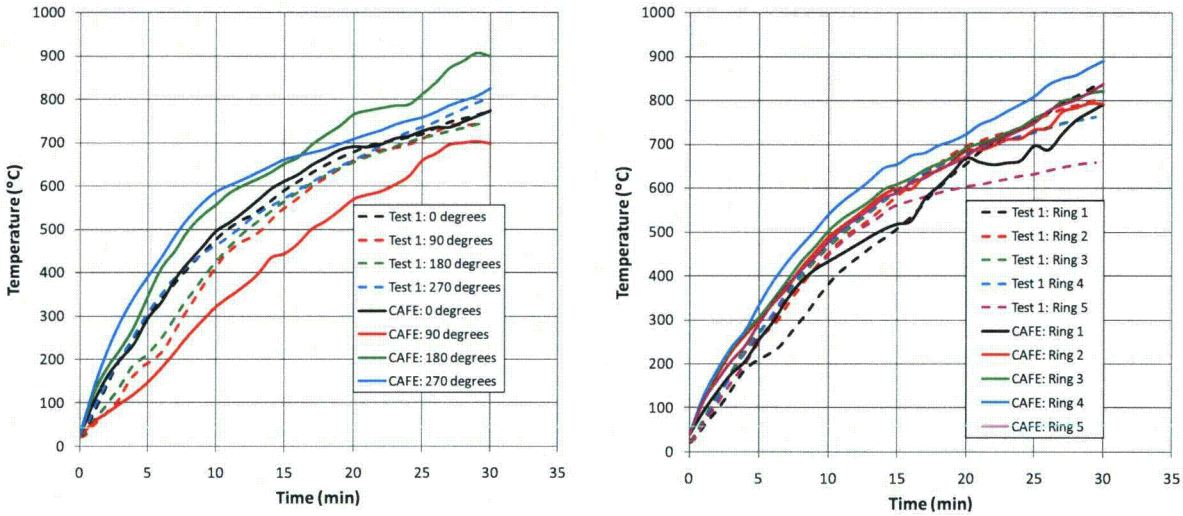

(a) (b)

Figure D-31 CAFE benchmark results using fully engulfed large calorimeter: (a) temperatures average along the 0-, 90-, 180-, and 270-degree side looking at the calorimeter from the negative z-direction and (b) temperatures averaged over each ring starting from Ring 1 located on the positive side of the z-axis

From this perspective, CAFE over predicts temperatures underneath and on the south side of the calorimeter and underpredicts temperatures on the top of the calorimeter. Figure D-31b

shows a plot of average temperatures over each TC ring starting from the left side of the calorimeter and moving along the negative z-axis, as shown in Figure D-30. From this perspective, CAFE predicts the average temperatures over the rings reasonably well.

Closer inspection of the temperature histories obtained from CAFE at each of the nodes corresponding to TC locations revealed excellent agreement with test data over most of the cask, except at locations where the wind effects are strongest—the last two rings to the right of Figure D-30 at 90 degrees (top side), 180 degrees (south side) and 270 degrees (underneath). Temperatures at 180 and 270 degrees are higher than expected, while temperatures at 90 degrees are underpredicted. Differences rapidly diminished going from the rings on the right side of the calorimeter to the rings on the left side, as shown in Figure D-30. Part of the reason for these discrepancies is the way in which the computational fluid dynamics model applies the wind boundary conditions. In the large calorimeter test series, windspeeds are obtained only at four locations around the pool and at three heights. These height-dependent data are applied uniformly over the corresponding cross-sections of the domain, which does not necessarily reflect the actual conditions in the test. This leads to windspeeds being higher than expected in some locations around the casks, such as the south side of the cask near ring 5 (rightmost ring in Figure D-30).

D.6.2 Small Calorimeter Test and Benchmark Results

Experimental data from a smaller pipe calorimeter is used to benchmark the view factor method used in CAFE (Lopez et al., 2003). The CAFE model for thermal radiation transport within and near large hydrocarbon fires is divided into two types—diffusive radiation inside the flame zone and clear air or view factor radiation outside the flame zone. Outside the flame zone, thermal radiation transport is modeled by the clear air or view factor method. The calculation of the view factor between the fire and an adjacent object is complicated by the fact that the outer surface of a fire (or smoky region) is dynamically changing as a result of the puffing and turbulent nature of flames (Lopez et al., 2003).

In the experiments, a calorimeter is positioned such that its axis is 1.5 m (4.9 feet) away from the center of the fuel pool. The wind blew the fire away from the calorimeter leaving a significantly larger gap between the pipe calorimeter and the plume. Figure D-32 presents the results from tests and CAFE. The temperatures shown are at the center ring of this calorimeter. The blue lines are obtained from experimental data and the black lines are obtained from CAFE. By looking at the temperature distribution of this very long pipe, it can be clearly seen how the external radiation algorithm worked on the far field object.

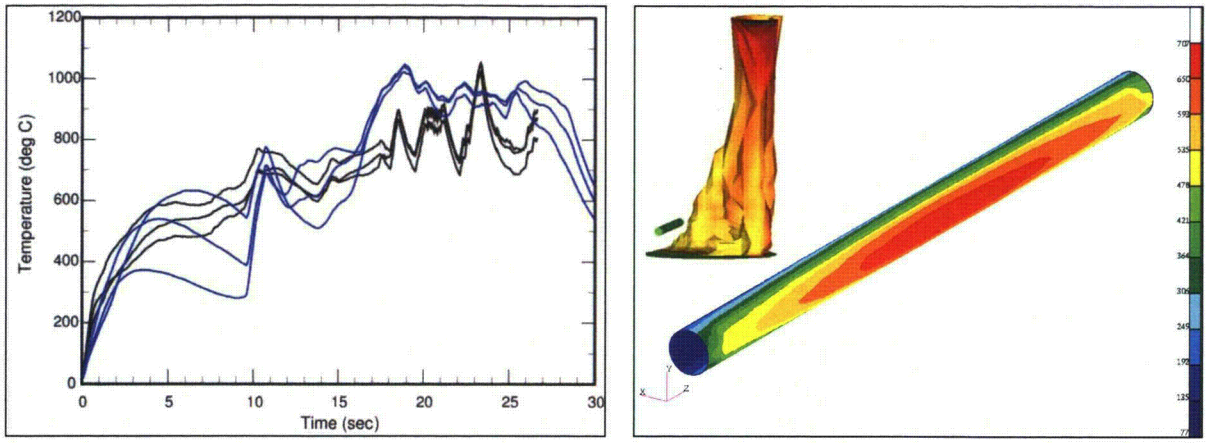

Figure D-32 CAFE benchmark results using a small calorimeter 1.5 m (4.9 feet) from the edge of the fire

D.6.3 Summary of Benchmark Results

The fully engulfing benchmark results show that CAFE bounds the experimental calorimeter temperatures. Inside the fire, CAFE underestimates temperatures near the top of the calorimeter, while it overestimates temperatures on all other sides of the calorimeter. Taken as a whole, these results show that CAFE slightly overpredicts the average temperature of the surface of the calorimeter. Therefore, it is expected that for the fully engulfing cases examined in this study, the cask surface temperatures predicted by CAFE will be close to or slightly higher than expected.

Outside the fire zone, CAFE is expected to predict reasonably accurate temperatures for objects near the fire. For objects further from the pool, results are expected to be less accurate given the method employed by the code. This is not a concern since the heat flux to objects outside the plume decreases with the distance squared, suggesting that the fire threat is also less severe with distance from the fuel pool as observed in the results for the 18.3-m (60-ft) standoff case.

D.7 Summary

This appendix discusses the method employed to obtain the thermal response of the Rail-Steel, Rail-Lead, and Truck-DU casks to several fires lasting longer than the HAC fire described in 10 CFR 71.73.

The approach used to model internals of these casks is similar to that presented in the respective cask SARs and in the Truck-DU cask SAR. This appendix describes some mathematical models and results reported in these documents and used in this study. In addition, modifications made to the cask models to simplify the complexities inherent in the cask design are noted. In general, boundary conditions and material properties differ slightly from those used in the SARs. For consistency, the same properties were used in these casks when the same or similar type materials were used. Since realistic boundary conditions are

sometimes difficult to implement using available data and current analysis tools, some simplifications were also necessary.

MSC Patran is the front-end code employed to generate the material database, the finite element discretization, and the boundary conditions for the internals of the casks. P/Thermal is the finite element heat transfer code used to solve the internal thermal response of the casks. CAFE is the computational fluid dynamics code used to generate the fire environment for the hypothetical fires lasting longer than the hypothetical fire described in 10 CFR 71.73. For these scenarios, CAFE and P/Thermal are coupled together to obtain the thermal response of the casks. P/Thermal is also used to generate the regulatory fire environments used for model verification. Results from these P/Thermal regulatory fires were compared against results presented in the SARs for the same regulatory environments. This served as a check to the current models.

Four fire accident scenarios are analyzed for the rail casks and one hypothetical fire accident scenario—the worst case in the rail cask analyses—is analyzed for the truck cask. These scenarios include the regulatory fire described in 10 CFR 71.73, a cask on the ground concentric with a fuel pool sufficiently large to engulf the cask, a cask on the ground with a pool fire offset by the width of a railcar (3 m (10 feet)), and a cask on the ground with a pool fire offset by the length of a railcar (18 m (60 feet)). These nonregulatory scenarios represent an accident in which a pool of flammable liquid and the cask are separated by one railcar width or by one railcar length following an accident. The results shown in this section demonstrate that the Rail-Steel, Rail-Lead, and Truck-DU casks maintain containment for the cases analyzed in this study.

APPENDIX E

DETAILS OF TRANSPORTATION ACCIDENTS

E.1 Types of Accidents and Incidents

The following types of accidents can interfere with routine transportation of spent nuclear fuel:

- accidents in which the spent fuel cask is not damaged or affected
  - minor traffic accidents (e.g., fender-benders, flat tires) that result in minor damage to the vehicle—usually called "incidents"[1]
  - accidents that damage the vehicle or trailer enough that the vehicle cannot move from the scene of the accident under its own power, but which do not result in damage to the spent fuel cask
  - accidents that involve a death or injury, but no damage to the spent fuel cask
- accidents in which the spent fuel cask is affected
  - accidents that result in loss of gamma shielding effectiveness but no release of radioactive material
  - accidents in which there is a release of radioactive material

Neutron shielding is always assumed to be lost in an accident because it is not designed to be accident resistant.

This analysis considers the first three types of accidents together. Chapter 5, Section 5.3 discusses the radiation doses and risks from these types of accidents. This appendix evaluates the last three types of accidents in detail. Only very severe accidents (those resulting in conditions much more severe than the regulatory accident) have the possibility of causing a loss of lead gamma shielding or release of radioactive material.

The analyses from Chapters 3 and 4 and Appendices C and D indicate that none of the accidents studied for this report lead to loss of radioactive material or gamma shielding effectiveness for the Rail-Steel or Truck-DU casks. These casks can only suffer a loss of neutron shielding. Some of the accident environments studied did lead to a loss of effectiveness of the gamma shielding for the Rail-Lead cask. When spent fuel is transported in this cask without an inner welded canister, some of the accident environments studied could result in a release of radioactive material. This appendix evaluates the probability and consequence of accidents that lead to a loss of shielding or release of radioactive material.

---

[1] In U.S. Department of Transportation parlance, an "accident" is an event that results in a death, an injury, or enough damage to a vehicle that it cannot move under its own power. All other events that result in nonroutine transportation are termed "incidents." This document uses the term "accident" for both accidents and incidents.

E.2 Accident Probabilities

E.2.1 Historic Accident Frequencies

The probability that a traffic accident occurs is based on historic accident frequencies. These have been developed and the statistics validated by the U.S. Department of Transportation (DOT). Table E-1 shows truck and railcar accidents from 1991 through 2007 (U.S. Department of Transportation, 2008). The following are the average accident frequencies for this period:

- 1.98×10^{-6} per kilometer (km) (3.19×10^{-6} per mile) for large trucks on Interstates and primary highways
- 1.32×10^{-7}/railcar-km (2.12×10^{-7}/railcar-mile) for freight rail

Accident frequencies decreased 33.5 percent for trucks and 53.8 percent for railcars between 1991 and 2007. This document uses the average because there are annual fluctuations. Figure 5.1 in Chapter 5 shows the accident frequency trends.

Table E-1 Truck and Railcar Accidents per km, 1991 through 2007

YEAR	TRUCK ACCIDENTS/KM	RAILCAR ACCIDENTS PER RAILCAR-KM
1991	2.39×10^{-6}	2.08×10^{-7}
1992	1.99×10^{-6}	1.91×10^{-7}
1993	2.19×10^{-6}	1.68×10^{-7}
1994	2.19×10^{-6}	1.64×10^{-7}
1995	2.39×10^{-6}	1.53×10^{-7}
1996	1.90×10^{-6}	1.39×10^{-7}
1997	1.89×10^{-6}	1.32×10^{-7}
1998	2.04×10^{-6}	1.19×10^{-7}
1999	1.84×10^{-6}	1.12×10^{-7}
2000	2.08×10^{-6}	1.12×10^{-7}
2001	1.99×10^{-6}	1.18×10^{-7}
2002	1.83×10^{-6}	1.12×10^{-7}
2003	1.85×10^{-6}	1.02×10^{-7}
2004	1.90×10^{-6}	1.00×10^{-7}
2005	1.73×10^{-6}	1.06×10^{-7}
2006	1.83×10^{-6}	1.04×10^{-7}
2007	1.59×10^{-6}	9.60×10^{-8}

E.2.2 Development of Conditional Accident Probabilities

Each specific accident scenario is described by a conditional probability ("conditional" on an accident occurring). The total probability of a specific accident scenario is the product of the accident frequency and the conditional probability for that scenario. Conditional probabilities are derived from event trees, as described below.

E.2.2.1 Conditional Probabilities of Truck Accidents

A transportation accident scenario can be disaggregated into a series of events. The conditional probability of a particular event in the scenario is best illustrated with an event tree, which is a diagram that includes all possible accident scenarios. Each branch of the tree is the series of events that comprise a particular accident scenario. The conditional probability is the product of the probabilities along a particular branch.

Figure E-1 is an event tree for truck accidents (Mills et al., 2006). An illustrative example would be the calculation of the conditional probability of a truck colliding with another vehicle on a bridge and then falling from the bridge onto a rocky embankment.

$$P_{conditional} = P_{collision} * P_{bridge\ accident} * P_{fall\ off\ bridge} * P_{soft\ rock}$$

$$P_{conditional} = (0.054)*(0.064)*(0.02)*(0.046) = 3.18 \times 10^{-6}$$

The far right column of Figure E-1 lists the conditional probabilities.

Mills et al. (2006) describes in detail the construction of the event tree in Figure E-1. Appendix C discusses details of collision accidents, and Appendix D provides additional information on fire accidents.

E.2.2.2 Conditional Probabilities of Rail Accidents

This study uses the event tree for rail found in Volpe, 2006, shown in Figure E-2.

E.2.2.3 Uncertainty in Event Trees

Event trees are excellent tools for dividing the universe of accidents into categories. The resultant probabilities are only as precise as the data that were available to develop the event tree. This becomes especially problematic for events that occur very rarely, such as the most severe accidents. For these events, the branch point distributions are assumed to be the same as those distributions for events that occur more frequently. NUREG/CR-6672, "Re-Examination of Spent Fuel Risk Estimates," issued in 2000 (Sprung et al., 2000), investigated uncertainties associated with event trees and found the total effect of all uncertainties to be approximately an order of magnitude. No further attempt was made to quantify the uncertainty associated with the event trees in this study.

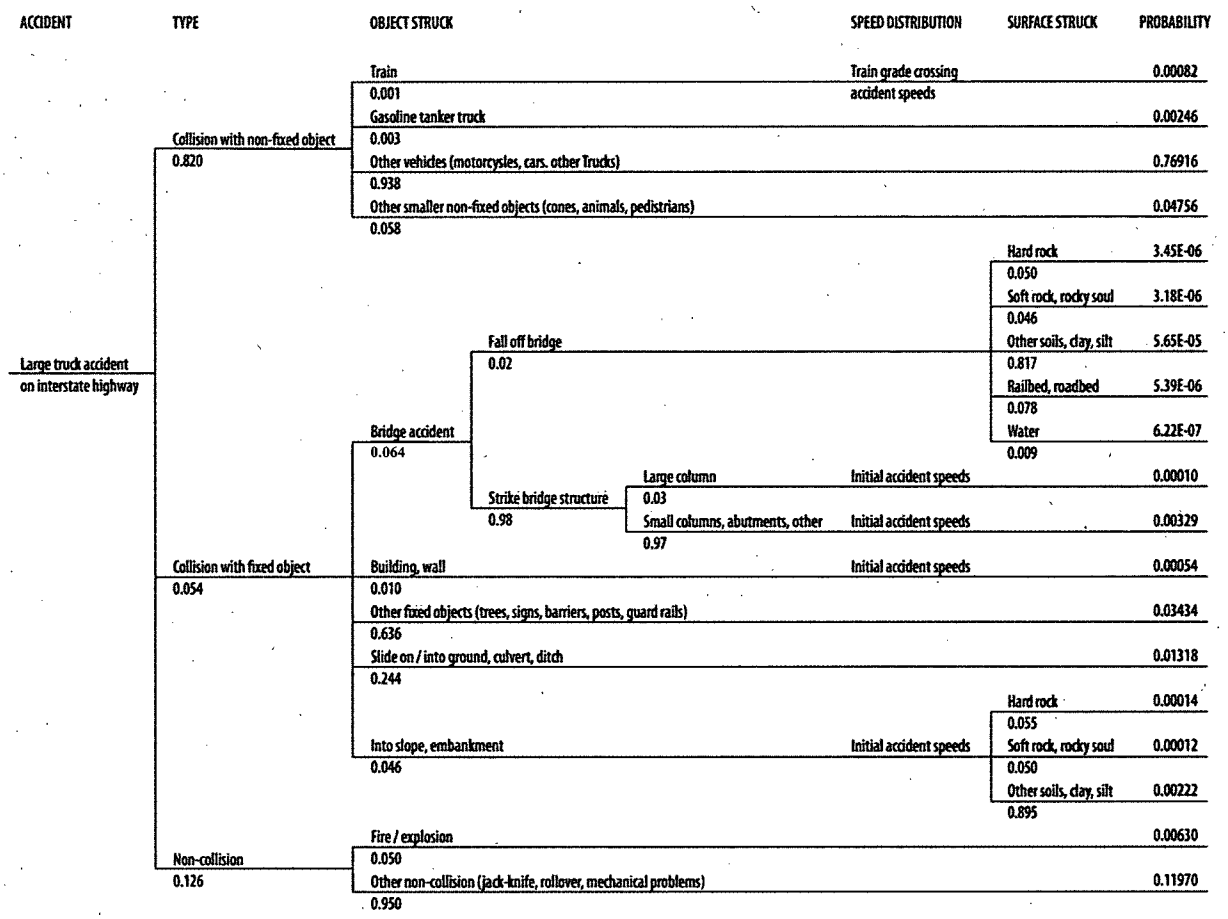

Figure E-1 Event tree for highway accidents (from Mills et al., 2006)

Rail Event Tree

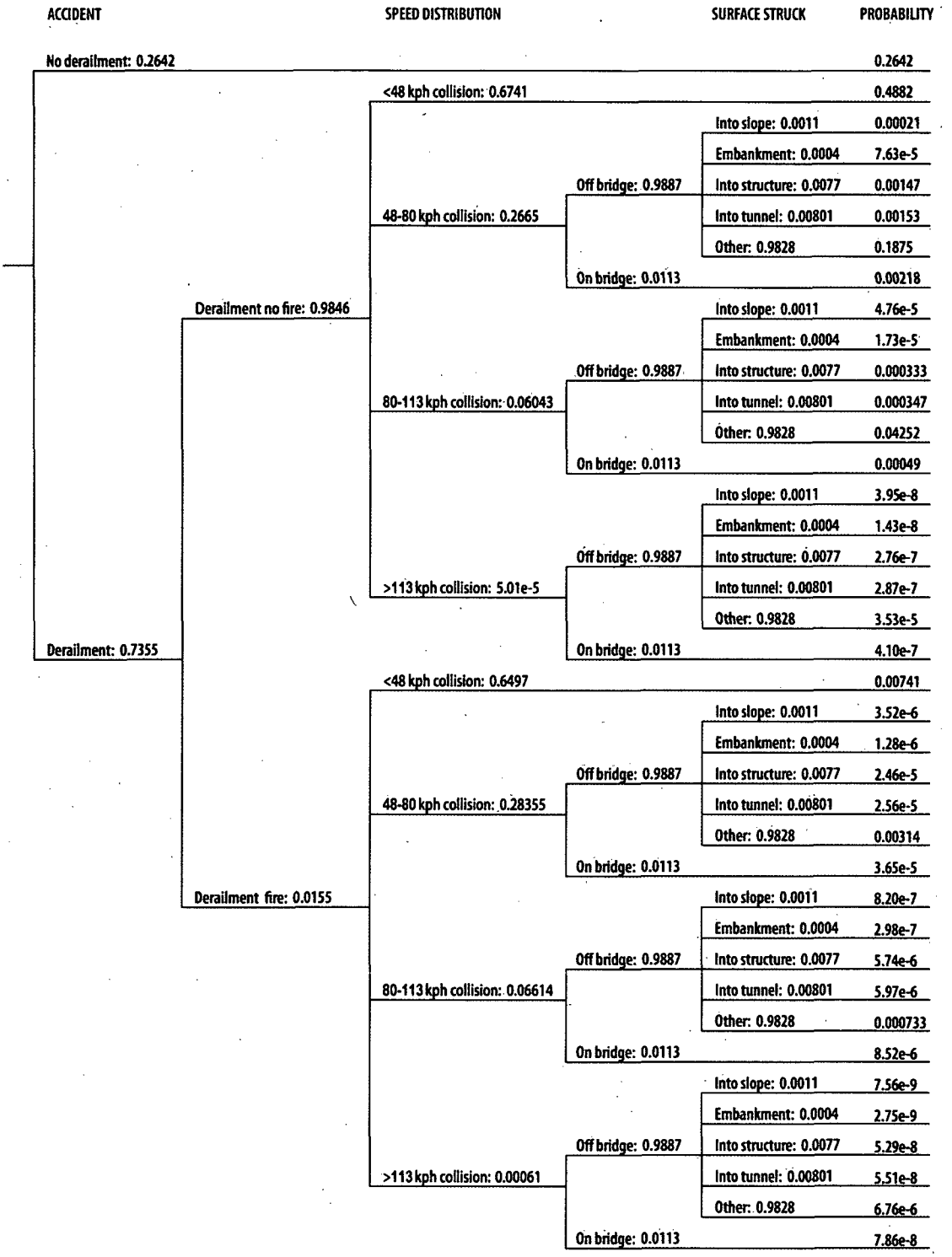

Figure E-2 Rail accident event tree (from Volpe, 2006)

E.3 Accident Risks and Consequences

E.3.1 Loss of Lead Gamma Shielding

The Rail-Lead cask is the only cask studied that uses lead as a gamma shield, so loss of the shielding would occur only in rail accidents. The Rail-Lead gamma shield is an annular lead cylinder about 0.127 meter (5 inches) thick. The lead shell can slump in a sufficiently severe impact, leaving a gap in the lead shield that results in increased external gamma radiation. The RADTRAN computer code models a gap in the shield from an impact and translates this to an increase in the dose from the virtual radiation source (O'Donnell et al., 2004; Dennis et al., 2009) that is the basis for the incident-free transportation model (Figure B-1, Appendix B). Figure E-3 is a diagram of the loss-of-shielding model, which recognizes the two-dimensional symmetry of the lead-shielded cask.

This study used the Monte Carlo N-Particle (MCNP) transport code to calculate the photon density along the line of receptor points (Figure E-3), both with and without a void (gap) in the lead shield. The difference in photon density, which is a function of the gap size, was expressed as a multiplier of the external dose rate at 1 meter (i.e., the transport index (TI)) from the fully shielded cask. Different gap sizes are modeled using different values of this multiplier.

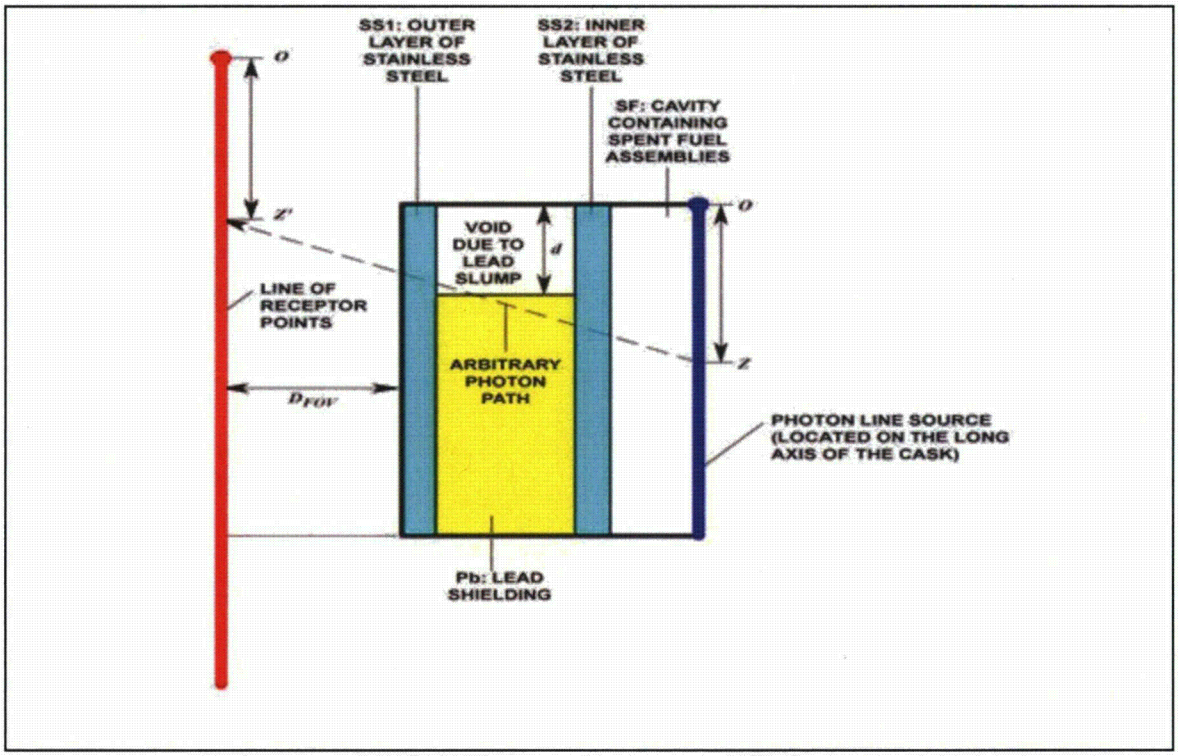

Figure E-3 The RADTRAN loss-of-shielding two-dimensional model (from O'Donnell et al., 2004)

The product of the multiplier and the TI of the fully shielded cask provides a new value of the TI, which RADTRAN then uses to calculate doses to receptors. Thus, the results of MCNP calculations provide a RADTRAN source for various gap sizes. The RADTRAN model

overestimates the dose to a receptor because it models all loss of lead shielding as a gap in the lead shield, rather than thinning of the lead shield, for example. Therefore, the doses calculated using RADTRAN are larger than what would be calculated using MCNP.

Figure E-3 shows only one side of the model because the model is symmetric and can apply to either side of the cask. All of the loss of lead shielding calculations in this study assumed the void was uniform around the cask.

E.3.1.1 Loss of Lead Shielding from Impact

Section 3.2.2 described the various amounts of lead slump that result from impact speed and orientation. Table E-2 shows the conditional probabilities of each combination of impact speed and orientation. The rail event tree does not include information on the hardness of the surfaces struck for any of its branches and only impacts into hard rock surfaces are severe enough to cause lead slump (see Section 3.3 for a discussion on impacts into yielding targets). To account for this, researchers used the impact surface distributions from the truck event tree (Figure E-1). This event tree indicated that only 5.5 percent of impacts are into hard rock surfaces. Only impacts that are at angles greater than 45 degrees are severe enough to cause lead slump (see Section 3.4).

Using the triangular distribution of impact angles, 33.3 percent of accidents have an impact angle greater than 45 degrees. The rail event tree also does not include any information about what happens after an accident that occurs on a bridge. Again, the detail for this is taken from the truck event tree, which indicates that 2 percent of the accidents that occur on a bridge result in the vehicle falling off the bridge, and 5 percent of those cases result in an impact onto hard rock. For falling off a bridge, the impact angle distribution is uniform rather than triangular, so the probability that the angle is greater than 45 degrees is 50 percent. Using this information, researchers calculated the conditional probabilities for accident scenarios in which an impact could result in lead slump by adding the probabilities at a particular impact speed for impacts into a slope and impacts into an embankment multiplied by 0.055 for hard rock and multiplied by 0.333 for impact angle. Added to this is the probability that the impact occurs on a bridge, multiplied by 0.02 for falling off the bridge, multiplied by 0.05 for hard rock, and multiplied by 0.5 for impact angle. An example calculation for calculating the conditional probability for a 193 kilometers per hour (kph) (120 mph) impact is shown below:

Rail event tree impact onto slope > 113 kph (70 mph) = 3.95×10^{-8} (from the derailment no fire branch)

Rail event tree impact onto embankment > 113 kph (70 mph) = 1.43×10^{-8}

Rail event tree accident on bridge > 113 kph (70 mph) = 4.10×10^{-7}

Fraction of accidents >113 kph (70 mph) that are > 145 kph (90 mph) = 0.05

Conditional probability = $\{[(3.95\times10^{-8} + 1.43\times10^{-8}) \times 0.055 \times 0.333] + [(4.10\times10^{-7}) \times 0.02 \times 0.05 \times 0.5]\} \times 0.05 = 5.96\times10^{-11}$

Table E-2 also shows the amount of lead slump, both as an absolute amount and as a fraction of the longest dimension of the lead shield.

Table E-3 shows dose rates to the maximally exposed individual (MEI) at various distances from the cask. The populations within 800 meters (1/2 mile) of the rail routes, as shown in Table 2-5, are the populations that could be exposed for each of the 16 rail routes modeled.

Table E-2 Parameters of Lead Shield Slumping from Impact
(These are input parameters to the RADTRAN calculation.)

Orientation	Impact Speed kph	Event Tree Impact Speed (kph)[a]	Maximum Slump (mm)[b]	Slumped fraction	Conditional Probability from Rail Event Tree[c]	Conditional Probability including Orientation
End (Probability = 0.1)	193	>113 (5%)[d]	355.48	0.0725	5.96×10^{-11}	5.96×10^{-12}
	145	>113 (95%)	83.2	0.0170	1.13×10^{-9}	1.13×10^{-10}
	97	80 to 113	18.28	0.00373	1.44×10^{-6}	1.44×10^{-7}
	48	48 to 80	6.43	0.00131	6.34×10^{-6}	6.34×10^{-7}
Corner (Probability = 0.6)	193	>113 (5%)[d]	310.48	0.0634	5.96×10^{-11}	3.57×10^{-11}
	145	>113 (95%)	114.52	0.0234	1.13×10^{-9}	6.79×10^{-10}
	97	80 to 113	25.11	0.00512	1.44×10^{-6}	8.62×10^{-7}
	48	48 to 80	1.65	0.000337	6.34×10^{-6}	3.80×10^{-6}
Side (Probability = 0.3)	193	>113 (5%)[d]	15.47	0.00316	5.96×10^{-11}	1.79×10^{-11}
	145	>113 (95%)	20.88	0.00426	1.13×10^{-9}	3.40×10^{-10}
	97	80 to 113	1.37	0.000280	1.44×10^{-6}	4.31×10^{-7}
	48	48 to 80	0.09	0.0000184	6.34×10^{-6}	1.90×10^{-6}

[a] Event tree impact speeds are binned. This column relates the binned speeds to the modeled impact speed.

[b] These values are derived from the finite element analysis (Chapter 3 and Appendix C).

[c] These values are the sum of probabilities of collision scenarios at a particular impact speed into slope and embankment multiplied by 0.055, because only impacts onto hard surfaces can cause lead slump, multiplied by 0.333, because only impacts that are at angles greater than 45 degrees can cause lead slump, plus the probability the accident occurs on a bridge, multiplied by 0.02 for accidents that fall off the bridge, multiplied by 0.055 for hard targets, multiplied by 0.5 for impact angles greater than 45 degrees.

[d] The event tree did not distinguish between impacts from 113 kph to 145 kph and from 145 kph to 193 kph. It is assumed that 5 percent of the impacts are greater than145 kph and 95 percent are between 113 kph and 145 kph.

Figure E-4 and Figure E-5 show dose rates to the MEI as a function of the fraction of shielding lost and as a function of distance from the cask. Exposure to the highest dose rate for 30 minutes would lead to a dose similar to a head computerized tomography (CT) scan (Shleien et al., 1998).

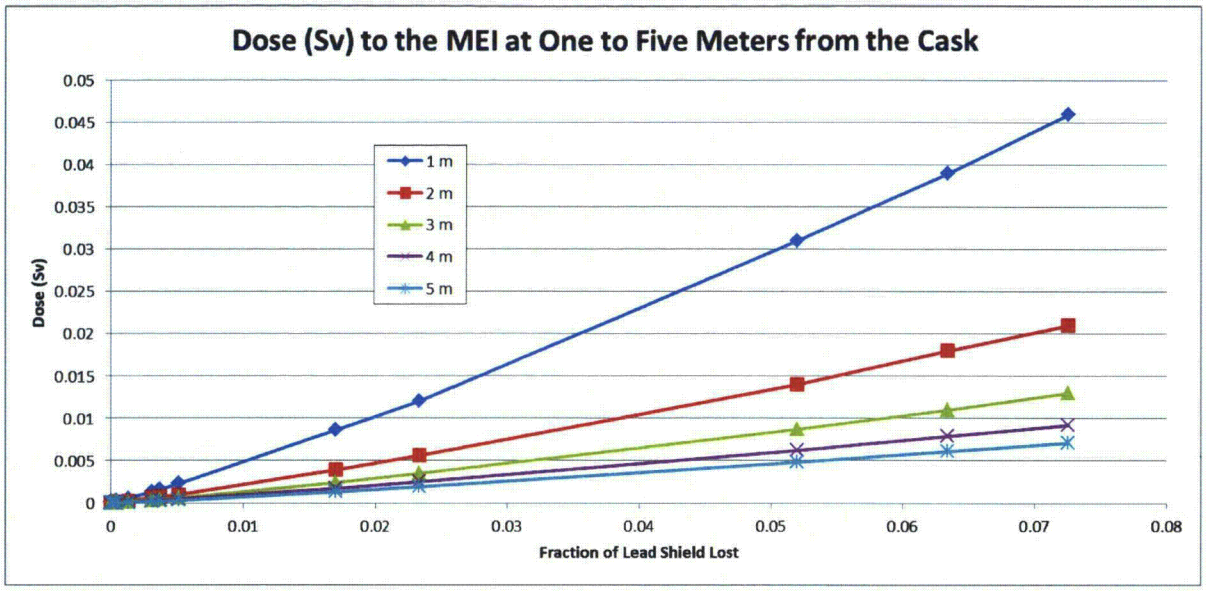

Figure E-4 Radiation dose rates to the MEI from loss of lead gamma shielding at distances from 1 to 5 meters from the cask carrying spent fuel

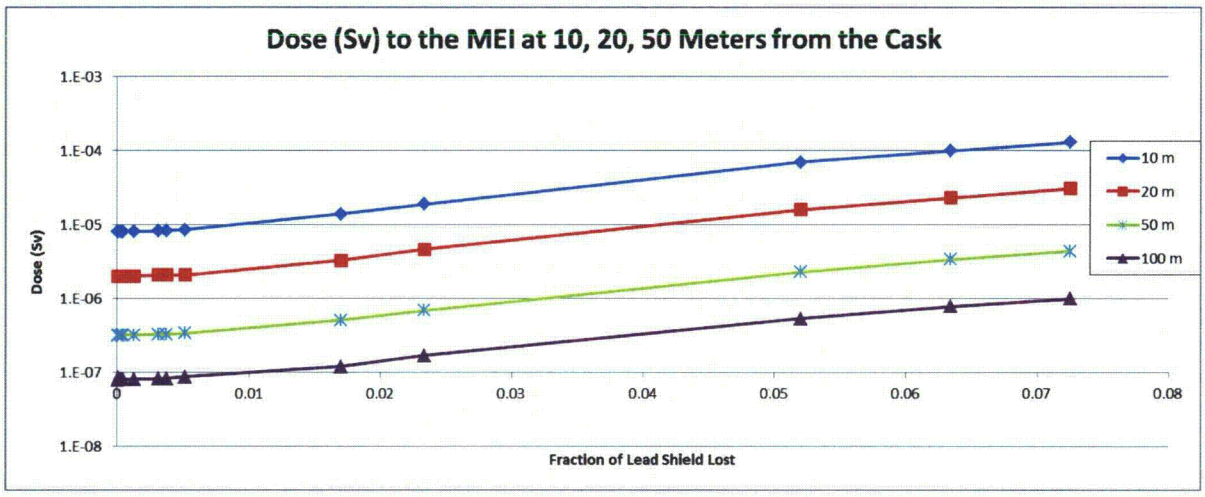

Figure E-5 Radiation dose rates to the MEI from loss of lead gamma shielding at distances from 10 to 100 meters from the cask carrying spent fuel. The vertical axis is logarithmic so that all of the dose rates can be shown on the same graph.

Table E-3 shows how the dose rate to the MEI depends on the fraction of the lead shield lost and the distance from the cask. The far left column of Table E-3 shows lead slump of the cask as computed from the finite element analyses discussed in Chapter 3 and Appendix C. RADTRAN computed the dose rates shown in the table using the model discussed in Section E.3.1. Only a few of the dose rates in the table exceed the regulatory dose rate of 0.01 sieverts per hour (Sv/h) (100 mrem/hr) from Title 10 of the *Code of Federal Regulations* (10 CFR) 71.51, "Additional Requirements for Type B Packages." These dose rates, which are shown in bold italics in the table, are the result of accidents that are much more severe than the

regulatory accident and occur with a very small probability (less than one in a billion accidents would produce the amount of lead slump required to result in these dose rates).

Table E-3 Radiation Dose Rates (Sv/h) to the MEI at Various Distances for the Cask (The numbers in bold italics exceed the external dose rate of 10 CFR 71.51. The dose rates are the direct output of the RADTRAN loss-of-shielding model.[2])

Fraction of slumped lead	1 m	2 m	3 m	4 m	5 m	10 m	20 m	50 m
7.25×10^{-2}	***4.6×10^{-2}***	***2.1×10^{-2}***	***1.3×10^{-2}***	9.2×10^{-3}	7.1×10^{-3}	1.3×10^{-4}	3.1×10^{-5}	4.4×10^{-6}
6.34×10^{-2}	***3.9×10^{-2}***	***1.8×10^{-2}***	***1.1×10^{-2}***	7.9×10^{-3}	6.1×10^{-3}	1.0×10^{-4}	2.3×10^{-5}	3.4×10^{-6}
2.34×10^{-2}	***1.2×10^{-2}***	5.6×10^{-3}	3.5×10^{-3}	2.5×10^{-3}	1.9×10^{-3}	1.9×10^{-5}	4.6×10^{-6}	6.9×10^{-7}
1.70×10^{-2}	8.6×10^{-3}	3.9×10^{-3}	2.4×10^{-3}	1.7×10^{-3}	1.3×10^{-3}	1.4×10^{-5}	3.3×10^{-6}	5.1×10^{-7}
5.12×10^{-3}	2.3×10^{-3}	1.0×10^{-3}	6.4×10^{-4}	4.6×10^{-4}	3.5×10^{-4}	8.5×10^{-6}	2.1×10^{-6}	3.4×10^{-7}
4.26×10^{-3}	1.9×10^{-3}	8.3×10^{-4}	5.2×10^{-4}	3.8×10^{-4}	2.9×10^{-4}	8.4×10^{-6}	2.1×10^{-6}	3.3×10^{-7}
3.73×10^{-3}	1.6×10^{-3}	7.2×10^{-4}	4.5×10^{-4}	3.3×10^{-4}	2.5×10^{-4}	8.3×10^{-6}	2.1×10^{-6}	3.3×10^{-7}
3.16×10^{-3}	1.3×10^{-3}	6.1×10^{-4}	3.8×10^{-4}	2.8×10^{-4}	2.1×10^{-4}	8.2×10^{-6}	2.1×10^{-6}	3.3×10^{-7}
1.31×10^{-3}	5.7×10^{-4}	2.6×10^{-4}	1.7×10^{-4}	1.2×10^{-4}	9.5×10^{-5}	8.1×10^{-6}	2.0×10^{-6}	3.2×10^{-7}
3.37×10^{-4}	2.3×10^{-4}	1.1×10^{-4}	7.2×10^{-5}	5.3×10^{-5}	4.2×10^{-5}	8.1×10^{-6}	2.0×10^{-6}	3.2×10^{-7}
2.80×10^{-4}	2.1×10^{-4}	1.0×10^{-4}	6.7×10^{-5}	5.0×10^{-5}	4.0×10^{-5}	8.1×10^{-6}	2.0×10^{-6}	3.2×10^{-7}
1.84×10^{-5}	1.4×10^{-4}	7.2×10^{-5}	4.8×10^{-5}	3.6×10^{-5}	2.9×10^{-5}	8.1×10^{-6}	2.0×10^{-6}	3.2×10^{-7}

Emergency responders would sustain the large dose rates that occur near the cask (1 to 5 meters (3.3 to 16.4 feet) from the cask). The 1- to 5-meter dose rates can be considered occupational rather than public doses. Exposure at the maximum dose rate (maximum slump at 1 meter (3.3 feet)) for 1 hour would approximate the annual occupational dose limit from 10 CFR Part 20, "Standards for Protection against Radiation." If a loss-of-shielding accident occurred on a public right of way (a railroad track in this case) no member of the public would be closer than 10 meters (33 feet). The public MEI dose rate (from the largest gap in the lead shield) would be 0.13 mSv/h (13 mrem/hr) (the 10-meter curve in Figure E-5).

The "dose risk" combines the probability of a particular accident with the consequence (the dose). Table E-3 estimates accident consequences (dose rates) only; it does not consider the probability of an accident severe enough to produce those consequences. The dose risk is much smaller than the dose because of the very low probability of an accident that produces a loss of shielding. Tables E-4and E-5 show the conditional dose risk (i.e., the product of the conditional probability with the dose consequence) for each fractional loss of lead shielding. For distances less than 10 meters (33 feet) from the cask, these doses are for a 1-hour exposure

---

[2] A rigorous calculation was performed at Oak Ridge National Laboratory (ORNL) using a three-dimensional radiation shielding model. The comparison of results with those in Table E-3 indicate that the results are acceptable. Results of the more rigorous calculation show generally good agreement; however, the ORNL 1-m values are 33 to 67 percent higher than the Table E-3 values. The differences may be the result of the manner in which the loss-of-shielding model was incorporated into RADTRAN—the additional dose caused by the shielding gap was expressed by a multiplier to the external dose rate.

and represent an occupational dose to emergency responders. For distances of 10 meters (33 feet) and greater, these doses are for a 10-hour exposure and represent the dose to the public. These dose risks are the risk of a particular accident scenario if there is an accident; they do not include the probability of an accident.

Table E-4 The "Conditional Dose Risk" in Sv to the MEI at Distances from the Cask from 1 to 5 Meters for 1 Hour

(The "conditional dose risk" is the product of conditional probabilities from Table E-2 and the 1 to 5 meter doses from Table* E-3.*)

Fraction of slumped lead	Conditional Probability	Distance from the cask (m)				
		1	2	3	4	5
7.25×10^{-2}	5.96×10^{-12}	2.74×10^{-13}	1.25×10^{-13}	7.74×10^{-14}	5.48×10^{-14}	4.23×10^{-14}
6.34×10^{-2}	3.57×10^{-11}	1.39×10^{-12}	6.43×10^{-13}	3.93×10^{-13}	2.82×10^{-13}	2.18×10^{-13}
2.34×10^{-2}	6.79×10^{-10}	8.15×10^{-12}	3.80×10^{-12}	2.38×10^{-12}	1.70×10^{-12}	1.29×10^{-12}
1.70×10^{-2}	1.13×10^{-10}	9.73×10^{-13}	4.41×10^{-13}	2.72×10^{-13}	1.92×10^{-13}	1.47×10^{-13}
5.12×10^{-3}	8.62×10^{-7}	1.98×10^{-9}	8.62×10^{-10}	5.52×10^{-10}	3.97×10^{-10}	3.02×10^{-10}
4.26×10^{-3}	3.40×10^{-10}	6.34×10^{-13}	2.81×10^{-13}	1.77×10^{-13}	1.29×10^{-13}	9.78×10^{-14}
3.73×10^{-3}	1.44×10^{-7}	2.30×10^{-10}	1.03×10^{-10}	6.47×10^{-11}	4.74×10^{-11}	3.59×10^{-11}
3.16×10^{-3}	1.79×10^{-11}	2.32×10^{-14}	1.09×10^{-14}	6.79×10^{-15}	5.00×10^{-15}	3.75×10^{-15}
1.31×10^{-3}	6.34×10^{-7}	3.61×10^{-10}	1.65×10^{-10}	1.08×10^{-10}	7.61×10^{-11}	6.02×10^{-11}
3.37×10^{-4}	3.80×10^{-6}	8.75×10^{-10}	4.18×10^{-10}	2.74×10^{-10}	2.02×10^{-10}	1.60×10^{-10}
2.80×10^{-4}	4.31×10^{-7}	9.19×10^{-11}	4.44×10^{-11}	2.91×10^{-11}	2.15×10^{-11}	1.71×10^{-11}
1.84×10^{-5}	1.90×10^{-6}	2.66×10^{-10}	1.37×10^{-10}	9.13×10^{-11}	6.84×10^{-11}	5.51×10^{-11}

Table E-5 The "Conditional Dose Risk" in Sv to the MEI at Distances 10 to 100 Meters from the Cask for 10 Hours

***(The "conditional dose risk" is the product of conditional probabilities from Table E-2 and the 10-, 20-, and 50-meter doses from Table E-3 and the 100-meter dose from Figure* E-5.)**

Fraction of slumped lead	Conditional Probability	Distance from the cask (m)			
		10	20	50	100
7.25×10^{-2}	5.96×10^{-12}	7.74×10^{-15}	1.85×10^{-15}	2.62×10^{-16}	5.93×10^{-17}
6.34×10^{-2}	3.57×10^{-11}	3.57×10^{-14}	8.22×10^{-15}	1.22×10^{-15}	2.82×10^{-16}
2.34×10^{-2}	6.79×10^{-10}	1.29×10^{-13}	3.12×10^{-14}	4.69×10^{-15}	1.16×10^{-15}
1.70×10^{-2}	1.13×10^{-10}	1.58×10^{-14}	3.74×10^{-15}	5.77×10^{-16}	1.37×10^{-16}
5.12×10^{-3}	8.62×10^{-7}	7.33×10^{-11}	1.81×10^{-11}	2.93×10^{-12}	7.53×10^{-13}
4.26×10^{-3}	3.40×10^{-10}	2.84×10^{-14}	7.13×10^{-15}	1.13×10^{-15}	2.87×10^{-16}
3.73×10^{-3}	1.44×10^{-7}	1.19×10^{-11}	3.02×10^{-12}	4.74×10^{-13}	1.19×10^{-13}
3.16×10^{-3}	1.79×10^{-11}	1.47×10^{-15}	3.75×10^{-16}	5.90×10^{-17}	1.47×10^{-17}
1.31×10^{-3}	6.34×10^{-7}	5.13×10^{-11}	1.27×10^{-11}	2.03×10^{-12}	5.15×10^{-13}
3.37×10^{-4}	3.80×10^{-6}	3.08×10^{-10}	7.61×10^{-11}	1.22×10^{-11}	3.07×10^{-12}
2.80×10^{-4}	4.31×10^{-7}	3.49×10^{-11}	8.62×10^{-12}	1.38×10^{-12}	3.47×10^{-13}
1.84×10^{-5}	1.90×10^{-6}	1.54×10^{-10}	3.80×10^{-11}	6.08×10^{-12}	1.50×10^{-12}

The collective dose risk to an exposed population within a radius *r* of the cask may be calculated by Equation E-1:

(E-1)
$$Dose\ Risk = A * L * PD * S * \sum_i^n P_{ci} * 10^{-6} * \int_{20}^{800} D_{ir} * 2\pi r dr$$
$$= A * L * PD * S * 1.46 * 10^{-12}$$

Where:

A is the accident frequency per kilometer (km) on the route segment under consideration

L is the length of the route segment in km

PD is the population density per square kilometer (km^2)

S is the shielding factor caused by residence type from Table II-3

P_{ci} is the conditional probability of the i^{th} fractional loss of shielding

10^{-6} is used to convert the integrated area from m^2 to km^2

r is the distance from the cask: 20 to 800 meters

D_{ir} is the dose from the i^{th} fractional loss of shielding at a distance *r* from the cask (these values are tabulated in Table E-3)

$2\pi r dr$ is the incremental area of the band at distance *r* from the cask (in square meters (m^2))

The index *i* indicates a particular fractional shielding loss, which Table E-3 summarizes. The summation in Equation E-1 is the conditional dose risk of all of the accidents considered, that is the "universe" of accidents. Only one accident is modeled, which is assumed to occur on any route segment, but not on more than one route segment. The summation in Equation E-1 is independent of accident location.

Population dose risk ultimately depends on the accident frequency, as well as on the population along the route where the accident happens. The accident frequency, accidents per kilometer, is equated to the accident probability. U.S. Department of Transportation (2008) provides the rail accident frequencies used in this analysis. Table E-6 shows the average railcar accident frequencies for each of the 16 rail routes analyzed. These accident frequencies are combined with the average dose risk integrated over the potentially exposed population.

Table E-6 Average Railcar Accident Frequencies and Accidents per Shipment on the Routes Studied

ORIGIN	DESTINATION	AVERAGE ACCIDENTS PER KM	ROUTE LENGTH (KM)	PROBABILITY OF AN ACCIDENT FOR THE TOTAL ROUTE
MAINE YANKEE	ORNL	6.5×10^{-7}	2,125	0.00139
	DEAF SMITH	5.8×10^{-7}	3,362	0.00194
	HANFORD	4.2×10^{-7}	5,084	0.00214
	SKULL VALLEY	5.1×10^{-7}	4,086	0.00208
KEWAUNEE	ORNL	4.3×10^{-7}	1,395	0.00060
	DEAF SMITH	3.3×10^{-7}	1,882	0.00062
	HANFORD	2.4×10^{-7}	3,028	0.00073
	SKULL VALLEY	3.7×10^{-7}	2,755	0.00103
INDIAN POINT	ORNL	8.8×10^{-6}	1,264	0.0112
	DEAF SMITH	6.2×10^{-7}	3,088	0.00192
	HANFORD	4.4×10^{-7}	4,781	0.00212
	SKULL VALLEY	5.5×10^{-7}	3,977	0.00217
INL	ORNL	3.6×10^{-7}	3,306	0.0012
	DEAF SMITH	3.5×10^{-7}	1,913	0.00067
	HANFORD	3.2×10^{-7}	1,062	0.00034
	SKULL VALLEY	2.8×10^{-7}	455	0.00013

Table E-7 shows the collective dose risks to populations on each side of the rail cask that has lost lead shielding on impact. These estimates include both the conditional probabilities and the accident frequencies on each route, as in Equation E-1.

Table E-7 Collective Dose Risks per Shipment (Person-Sv) from Loss of Lead Shielding, Including Accident and Conditional Probabilities

ORIGIN	TYPE	Destination			
		ORNL	DEAF SMITH	HANFORD	SKULL VALLEY
MAINE YANKEE	Rural	2.11×10^{-14}	2.65×10^{-14}	4.74×10^{-14}	3.59×10^{-14}
	Suburban	2.23×10^{-13}	2.34×10^{-13}	**2.16×10^{-13}**	2.19×10^{-13}
	Urban	5.95×10^{-15}	7.17×10^{-15}	8.19×10^{-15}	4.83×10^{-15}
KEWAUNEE	Rural	9.64×10^{-15}	6.29×10^{-15}	8.06×10^{-15}	1.34×10^{-14}
	Suburban	9.07×10^{-14}	5.49×10^{-14}	4.50×10^{-14}	9.41×10^{-14}
	Urban	3.35×10^{-15}	2.25×10^{-15}	8.24×10^{-16}	2.38×10^{-15}
INDIAN POINT	Rural	1.12×10^{-13}	2.25×10^{-14}	3.02×10^{-14}	3.04×10^{-14}
	Suburban	3.04×10^{-12}	2.07×10^{-13}	2.16×10^{-13}	2.33×10^{-13}
	Urban	3.72×10^{-13}	8.15×10^{-15}	7.27×10^{-15}	7.21×10^{-15}
IDAHO NATIONAL LAB	Rural	1.66×10^{-14}	4.00×10^{-15}	2.56×10^{-15}	1.62×10^{-15}
	Suburban	8.09×10^{-14}	3.60×10^{-14}	1.76×10^{-14}	1.26×10^{-14}
	Urban	1.34×10^{-15}	6.49×10^{-16}	3.71×10^{-16}	4.38×10^{-16}

Example: For the suburban route segment of the Maine Yankee–to–Hanford route:

Accident rate: 4.2×10^{-7}/km (from Table E-6)

Segment Length: 1,135 km

Population density: 357 persons/km^2

Suburban shielding factor: 0.87

Dose risk = 4.2×10^{-7} accident/km * 1135 km * 357persons/km^2 * 0.87 * 1.46×10^{-12} SE-km^2/accident = 2.16×10^{-13} person-Sv (2.16×10^{-8} person-mrem)

E.3.1.2 Loss of Lead Shielding with Fire

The loss of lead shielding because of a fire occurs after the end of the fire when the cask cools. Lead expands as it melts and can buckle the innermost cask shell. When the melted lead cools and solidifies, it occupies the same volume as before expansion, but the volume available between the steel cask shells is larger because of the buckling of the inner shell, leaving a gap. Appendix D describes in full detail the melting of lead and the formation of a gap. Briefly, if the cask is offset from the fire, the gap would be in the section of lead shield facing the fire. In an engulfing fire, the gap would be at the upper surface of the cask. For conservatism, this study assumes that the loss of lead shielding is uniform around the cask and people in all directions are equally exposed. Therefore, in both cases, anyone facing the side of the cask with the shielding gap could sustain an increased radiation dose.

Two accidental fire scenarios can result in a loss of lead shielding:

- Fire Scenario 1: A sufficiently hot pool fire engulfs a cask on the ground and can melt enough lead in 3 hours to create an 8.14-percent fractional shield loss.
- Fire Scenario 2: A sufficiently hot pool fire offset from the cask burns for more than 3 hours and can create a 2.01-percent fractional shield loss.

Appendix D fully describes these scenarios. Table E-8 shows the doses sustained by the MEI, exposed for 1 hour, at various distances from the cask.

Table E-8 Radiation Dose (Sv) to the MEI at Various Distances from a Cask that Has Been in a Fire (Direct RADTRAN Output)

Reduction of lead shielding[a]	1 m	2 m	5 m	10 m	20 m	50 m	100 m
0.0201	7.0×10^{-3}	3.1×10^{-3}	1.1×10^{-3}	1.1×10^{-5}	2.6×10^{-6}	3.9×10^{-7}	9.4×10^{-8}
0.0814	3.5×10^{-2}	1.6×10^{-2}	5.4×10^{-3}	1.1×10^{-4}	2.6×10^{-5}	3.7×10^{-6}	8.5×10^{-7}

[a] From the thermal analyses in Chapter 4 and Appendix D.

No lead shielding would be lost until after the fire was out and the cask had cooled enough for the lead to solidify; only then would there be a gap in the lead shield. Differential heating of the lead shield could result in geometry and associated volume changes that could impact the shielding effectiveness locally. Such effects would have minimal impact on the dose. Thus, no one would be exposed for many hours after the accident, and with a fire this severe, nearby residents and the public would probably have been evacuated. The MEI in this case would be an emergency responder. Under these circumstances, measures could be taken to mitigate emergency responder exposures.

Volpe (2006), Figure 16, postulates a chain of events leading to a fire, from which the probability of these scenarios can be calculated. Figure E-6 shows the relevant portion of the Volpe figure.

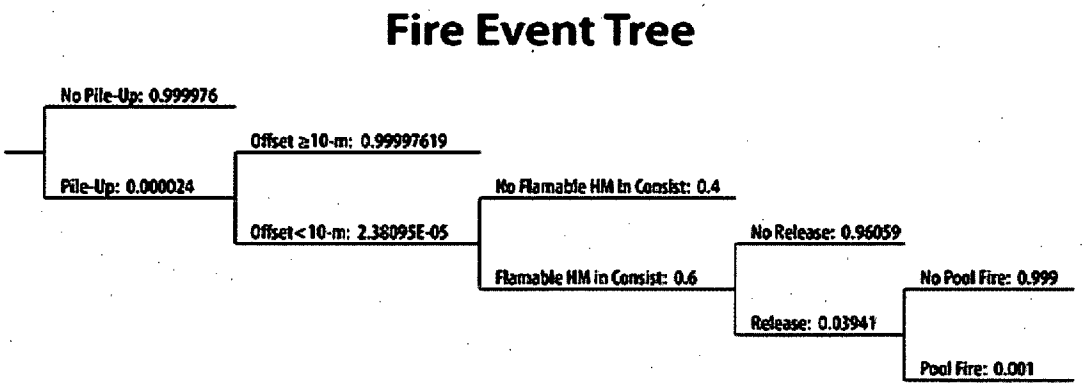

Figure E-6 Event tree branch for a rail fire accident (from Volpe, 2006, Figure 16)

To get to the starting point of the fire event tree, certain other events must occur. The first of these events is a major derailment, as shown in Table E-9. Volpe estimates that the speed at the time of the accident for such a derailment is at least 80 kph (50 miles per hour). If a pileup could occur in any kind of derailment other than in a tunnel, from Figure E-2, the probability of such a major collision/derailment/fire can be calculated as follows:

$$P_{derailment} * P_{fire} * (P_{80–113\text{-}kph\ collision} + P_{>113\text{-}kph\ collision})) * [P_{offbridge} * (P_{slope} + P_{embankment} + P_{structure}) + P_{onbridge}] = P$$

$$(0.7355) * (0.0155) * (0.06614 + 0.00061) * [0.9887 * (0.0011 + 0.0004 + 0.0077) + 0.0113] = 1.55\times10^{-5}$$

The summation of surfaces struck does not include the "other" branch of the event tree because this branch represents the most common case for derailments—where the derailed cars remain upright on the side of the track. Table E-9 lists the other events in the scenario, together with the probability of each event. These events are a pileup, a flammable hazardous cargo within 10 meters (33 feet) (about half a railcar length), leaking of that hazardous substance, and ignition of a pool fire. The net probability of the sequence of events shown in Table E-9 following a major pileup is 1.35×10^{-14}. The net probability depends on the very small pileup probability of 2.4×10^{-5}. Thus, it is instructive to estimate the probability without the assumption of a pileup. Using the "no pileup" branch, the net probability for the events of Table E-9 is 5.6×10^{-10}, still an exceptionally small number. The uncertainties in this analysis are exceedingly large compared to the probabilities. Essentially, the sequence of events in Figure E-6, with or without the pileup, is unlikely to happen.

The conditional probability of Fire Scenario 1, a major derailment, with or without a pileup, that leads to a 3-hour pool fire that surrounds the cask is—

$$(1.55\times10^{-5}) * (5.6\times10^{-10}) = 8.7\times10^{-15}$$

The conditional probability of Fire Scenario 2, a major derailment that does not involve a pileup but leads to a 3-hour fire offset from the cask by more than 10 meters (33 feet), is—

$$(1.55\times10^{-5}) * (2.36\times10^{-5}) = 3.7\times10^{-10}$$

Table E-9 Events Leading to a Train Fire That Could Involve a Spent Fuel Cask

Event	Probability	Alternative event	Probability
Major derailment (>48 kph)	8×10^{-5}	No major derailment	0.99992
Pileup	2.4×10^{-5}	No pileup	0.99998
Offset < 10 m	2.38×10^{-5}	Offset >10 m	0.99998
Flammable hazardous material in another railcar	0.6	No flammable material available	0.4
Release of flammable material	0.0394	No release of flammable material	0.9606
Pool fire	0.001	No pool fire	0.999

The average accident frequency for the 16 rail routes studied is 1.9×10^{-3} (the range is from 1.3×10^{-4} to 1.1×10^{-2}).[3] Thus, the average probability of an accidental fire that could cause loss of lead shielding in a rail cask is $1.9\times10^{-3} * 8.7\times10^{-15} = 1.7\times10^{-17}$ if the cask is concentric with the fire and $1.9\times10^{-3} * 3.7\times10^{-10} = 7.0\times10^{-13}$ if the cask and fire are offset by 10 meters (33 feet) or more. The largest dose risk to a person 1 meter (3.3 feet) away from the cask with 2-percent lead loss for 1 hour would be $7.0\times10^{-13} * 7.0\times10^{-3} = 4.9\times10^{-15}$ Sv (this dose risk is larger than that from the cask in the engulfing fire).

E.3.2 Loss of Neutron Shielding

The neutron shield is usually a hydrocarbon or carbohydrate polymer, sometimes borated, since boron and organic polymers are good neutron absorbers. Neutron shielding burns, and it could be destroyed in a fire. The neutron dose from loss of shielding in a fire is estimated using the parameters listed in Table E-10. The conditional probability of a truck fire is from Figure E-1. The conditional probability of a rail fire is a combination of the fire probability in Figure E-2 and the following steps from Table E-9:

- a pileup
- flammable cargo on the train
- release of the flammable cargo

The other parameters are the same as those used in calculating doses from an accident in which there is no release of radioactive material and no loss of lead shielding (Chapter 5, Section 5.4).

---

[3] This value is obtained by multiplying the appropriate accident frequency per kilometer from Table E-7 by the appropriate route length in kilometers from Table 2-5.

Table E-10 Some Parameters Used in Calculating Loss of Neutron Shielding

Parameter	Truck-DU	Rail-Lead	Rail-Steel
Conditional probability of a fire[a]	0.0063[b]	8.9×10^{-8}	8.9×10^{-8}
Neutron dose rate at one meter from the cask in mSv/h (mrem/h)[c]	1.78 (178)	1.81 (181)	1.82 (182)
Shielding of residents	none	none	none
Time until the cask is removed (h)	10	10	10

[a] The truck fire probability comes from Figure E-1, and the rail fire probability comes from Volpe (2006).

[b] The conditional probability of a fire for the Truck-DU cask is much higher than that for the two rail casks, in part because truck accidents always involve a source of fuel (the gas tanks of the truck) while many railcar accidents do not involve the locomotive and because of the way the event trees were constructed. The truck event tree does not distinguish between minor fires and ones that are severe enough to damage the neutron shielding, while the rail event tree only considers severe fires. Therefore, the conditional probability of a truck fire is quite conservative.

[c] The neutron dose at 2 meters from the Truck-DU cask is from General Atomics (1998); for the Rail-Lead cask, from Nuclear Acceptance Corporation International (2002); and for the Rail-Steel cask, from Holtec International (2004). The respective TI values were calculated from these numbers using RADTRAN, which slightly overestimates results (Steinman et al., 2002). The RADTRAN external dose rate is then modeled as entirely neutron emission.

Table E-11 shows the neutron doses to an emergency responder (5 meters from the cask), and Figure E-7 shows the RADTRAN output that was used to generate the doses.

Table E-12 shows the collective doses to nearby residents on the 16 truck and 16 rail routes analyzed, and Table E-13 shows the total collective dose risks, including accident frequency. For the Rail-Lead cask, the neutron doses would add to the gamma dose from the loss of lead shielding in the cases in which the fire was severe enough to result in a loss of lead shielding.

Table E-11 Doses to an Emergency Responder 5 Meters from the Cask from a Loss of Neutron Shielding Accident

Cask	10-hour 10 CFR 71.51 dose in Sv
Truck-DU	0.0073
Rail-Lead	0.0076
Rail-Steel	0.0077

RADTRAN STOP INPUT FILE

STOP RESPONDERT GA_4 1.0 5.0 5.0 1.0 10.0
STOP RESPONDERNAC NAC-STC 1.0 5.0 5.0 1.0 10.0
STOP RESPONDERHI HISTAR 1.0 5.0 5.0 1.0 10.0

RADTRAN OUTPUT FILE

STOP EXPOSURE IN PERSON-REM

LINE-SOURCE RESPONDERT 7.29E-01
LINE-SOURCE RESPONDERNAC 7.61E-01
LINE-SOURCE RESPONDERHI 7.73E-01

Figure E-7 RADTRAN input and output for Table E-11

Table E-12 Collective Conditional Doses to Nearby Residents in Person-Sv from Loss of Neutron Shielding

FROM	TO	Truck-DU	Rail-Lead	Rail-Steel
MAINE YANKEE	ORNL	7.49×10^{-4}	7.17×10^{-4}	7.40×10^{-4}
	DEAF SMITH	7.01×10^{-4}	6.71×10^{-4}	6.93×10^{-4}
	HANFORD	6.23×10^{-4}	5.96×10^{-4}	6.15×10^{-4}
	SKULL VALLEY	6.38×10^{-4}	6.11×10^{-4}	6.31×10^{-4}
KEWAUNEE	ORNL	6.87×10^{-4}	6.57×10^{-4}	6.78×10^{-4}
	DEAF SMITH	6.41×10^{-4}	6.13×10^{-4}	6.33×10^{-4}
	HANFORD	5.98×10^{-4}	5.72×10^{-4}	5.91×10^{-4}
	SKULL VALLEY	6.17×10^{-4}	5.91×10^{-4}	6.10×10^{-4}
INDIAN POINT	ORNL	7.28×10^{-4}	6.97×10^{-4}	7.20×10^{-4}
	DEAF SMITH	6.95×10^{-4}	6.65×10^{-4}	6.87×10^{-4}
	HANFORD	6.38×10^{-4}	6.11×10^{-4}	6.31×10^{-4}
	SKULL VALLEY	6.63×10^{-4}	6.34×10^{-4}	6.55×10^{-4}
INL	ORNL	5.78×10^{-4}	5.53×10^{-4}	5.71×10^{-4}
	DEAF SMITH	6.16×10^{-4}	5.89×10^{-4}	6.08×10^{-4}
	HANFORD	3.78×10^{-4}	3.62×10^{-4}	3.73×10^{-4}
	SKULL VALLEY	6.41×10^{-4}	6.13×10^{-4}	6.33×10^{-4}

Table E-13 Collective Conditional Dose Risks in Person-Sv from Loss of Neutron Shielding

FROM	TO	Truck-DU	Rail-Lead	Rail-Steel
MAINE YANKEE	ORNL	4.7×10^{-6}	6.4×10^{-11}	6.6×10^{-11}
	DEAF SMITH	4.4×10^{-6}	6.0×10^{-11}	6.2×10^{-11}
	HANFORD	3.9×10^{-6}	5.3×10^{-11}	5.5×10^{-11}
	SKULL VALLEY	4.0×10^{-6}	5.4×10^{-11}	5.6×10^{-11}
KEWAUNEE	ORNL	4.3×10^{-6}	5.8×10^{-11}	6.0×10^{-11}
	DEAF SMITH	4.0×10^{-6}	5.5×10^{-11}	5.6×10^{-11}
	HANFORD	3.8×10^{-6}	5.1×10^{-11}	5.3×10^{-11}
	SKULL VALLEY	3.9×10^{-6}	5.3×10^{-11}	5.4×10^{-11}
INDIAN POINT	ORNL	4.6×10^{-6}	6.2×10^{-11}	6.4×10^{-11}
	DEAF SMITH	4.4×10^{-6}	5.9×10^{-11}	6.1×10^{-11}
	HANFORD	4.0×10^{-6}	5.4×10^{-11}	5.6×10^{-11}
	SKULL VALLEY	4.2×10^{-6}	5.6×10^{-11}	5.8×10^{-11}
INL	ORNL	3.6×10^{-6}	4.9×10^{-11}	5.1×10^{-11}
	DEAF SMITH	3.9×10^{-6}	5.2×10^{-11}	5.4×10^{-11}
	HANFORD	2.4×10^{-6}	3.2×10^{-11}	3.3×10^{-11}
	SKULL VALLEY	4.0×10^{-6}	5.5×10^{-11}	5.6×10^{-11}

To get the collective dose risk for loss of neutron shielding, the collective conditional dose risks from Table E-13 must be multiplied by the probability that an accident occurs. Table E-6 gives the accident probability for the rail routes. For the truck routes, the route length (from Table 2-5) is multiplied by the national average accident rate, 1.98×10^{-6}/km (3.19×10^{-6}/mile). Table E-14 shows the resulting collective dose risks. Comparing these results to those from the loss of lead shielding in Table E-7, it can be seen that loss of lead shielding produces a higher collective dose risk, even though it is a much lower probability event.

Table E-14 Collective Dose Risks in Person-Sv from Loss of Neutron Shielding

FROM	TO	Truck-DU	Rail-Lead	Rail-Steel
MAINE YANKEE	ORNL	4.67×10^{-8}	8.90×10^{-14}	9.17×10^{-14}
	DEAF SMITH	3.13×10^{-8}	1.16×10^{-13}	1.20×10^{-13}
	HANFORD	3.22×10^{-8}	1.13×10^{-13}	1.18×10^{-13}
	SKULL VALLEY	1.41×10^{-8}	1.12×10^{-13}	1.16×10^{-13}
KEWAUNEE	ORNL	2.94×10^{-8}	3.48×10^{-14}	3.60×10^{-14}
	DEAF SMITH	1.70×10^{-8}	3.41×10^{-14}	3.47×10^{-14}
	HANFORD	1.97×10^{-8}	3.72×10^{-14}	3.87×10^{-14}
	SKULL VALLEY	9.83×10^{-9}	5.46×10^{-14}	5.56×10^{-14}
INDIAN POINT	ORNL	4.11×10^{-8}	6.94×10^{-13}	7.17×10^{-13}
	DEAF SMITH	2.68×10^{-8}	1.13×10^{-13}	1.17×10^{-13}
	HANFORD	2.91×10^{-8}	1.14×10^{-13}	1.19×10^{-13}
	SKULL VALLEY	1.04×10^{-8}	1.22×10^{-13}	1.26×10^{-13}
INL	ORNL	6.85×10^{-9}	5.88×10^{-14}	6.12×10^{-14}
	DEAF SMITH	1.77×10^{-8}	3.48×10^{-14}	3.62×10^{-14}
	HANFORD	2.24×10^{-9}	1.09×10^{-14}	1.12×10^{-14}
	SKULL VALLEY	2.61×10^{-8}	7.15×10^{-15}	7.28×10^{-15}

E.4 Release of Radioactive Materials in Accidents

E.4.1 Spent Fuel Inventory

A Rail-Lead cask is the only cask studied that would release any radioactive material in an accident. Since there is no traffic accident that would result in a release from the Truck-DU or Rail-Steel cask, the inventory of those casks is not relevant to this analysis. The fuel used in this analysis is pressurized-water reactor (PWR) fuel, with a burnup of 45,000 megawatt-days per metric ton of uranium (MTU) (the maximum burnup that a Rail-Lead cask would transport), which has cooled for 9 years before transport (Appendix A). The radionuclide inventory of this fuel was determined using ORIGEN (Croff, 1980). The radionuclide activities in the inventory were "normalized" by dividing each activity by the A_2 value for that radionuclide. The A_2 value, the amount of the radionuclide that could be transported in a Type A container, is an indication of the radiotoxicity; the larger the A_2 value, the smaller the radiotoxicity of that nuclide. Researchers then sorted and added the normalized radioactivities until they reached 99.99 percent of the total normalized radioactivity. The "total normalized activity" referred to here is not the total A_2 value as calculated by the formula in Appendix A, "Determination of A_1 and A_2," to 10 CFR Part 71, "Packaging and Transportation of Radioactive Material." Table E-15 lists the radionuclides selected this way, together with their actual radioactivities (not the normalized radioactivities). Normalized radioactivities are used only to identify 99.9 percent of the radiotoxicity. The actual activity is the basis for the release fraction of each radionuclide.

Table E-15 Inventory for the Rail-Lead Cask

Radionuclide	Name	Form	Terabecquerels (TBq) 26 Assemblies	Curies (Ci) 26 Assemblies
^{241}Am	americium	particle	193	5,210
^{240}Pu	plutonium	particle	184	4,970
^{238}Pu	plutonium	particle	180	4,850
^{241}Pu	plutonium	particle	10,440	282,000
^{90}Y	yttrium	particle	40,400	1,090,000
^{90}Sr	strontium	particle	40,400	1,090,000
^{137}Cs	cesium	volatile	50,400	1,360,000
^{239}Pu	plutonium	particle	71.9	1,940
^{244}Cm	curium	particle	31.5	852
^{134}Cs	cesium	volatile	3030	81,800
^{154}Eu	europium	particle	146	3,950
^{106}Ru	ruthenium	particle	467	12,600
^{243}Cm	curium	particle	1.16	31.3
^{243}Am	americium	particle	0.995	26.9
^{144}Ce	cerium	particle	180	4,850
^{242}Pu	plutonium	particle	0.614	16.6
^{125}Sb	antimony	particle	431	11,600
^{155}Eu	europium	particle	607	16,400
^{242m}Am	americium	particle	0.163	4.40
^{242}Am	americium	particle	0.162	4.38
^{60}Co	cobalt	CRUD	55.6	1,500
^{125m}Te	tellerium	particle	105	2,840
^{234}U	uranium	particle	0.572	15.5
^{85}Kr	krypton	gas	3,340	90,100

E.4.2 Dispersion of Released Radionuclides

If a spent fuel cask transportation accident did result in the release of radioactive material, the public could be exposed if the material were to be dispersed through the air. Experimental work reviewed by Sprung et al. (2000) indicates that only very small particles with an activity mean aerodynamic diameter (AMAD)[4] of 10 microns or less would be released from a cask in an accident because the only release path is through the seals at the ends of the cask. Ten microns is generally considered the upper limit of respirability. Thus, particles accidentally released from a cask would be released as a respirable aerosol.

[4] The AMAD is the diameter of a sphere of density one gram per cubic centimeter that has the same inertial properties as the actual particle.

The discussion below is an abbreviated discussion of air dispersion, a subject that is treated extensively and in detail in textbooks like Wark and Warner (1981).

The basic equation for atmospheric dispersion of an aerosol is the Gaussian dispersion equation (Turner, 1994, Chapter 2):

(E-2)
$$\frac{CHI}{Q} = \frac{1}{2\pi u \sigma_y \sigma_z} \exp\left[\frac{-y^2}{2\sigma_y^2}\right] \exp\left[\frac{-z^2}{2\sigma_z^2}\right]$$

Where:

CHI[5] = the concentration of particles in the air

Q = the radioactivity or mass of airborne particles

u = the windspeed

σ_y, σ_z are meteorological constants and are functions of the downwind distance *x* and the meteorological conditions

The wind direction is traditionally along the x axis of a Cartesian coordinate system, the crosswind direction is y, and z represents the altitude above ground. When the plume of released material rises buoyantly to a height *H*, the Gaussian equation becomes—

(E-3)
$$\frac{CHI}{Q} = \frac{1}{2\pi u \sigma_y \sigma_z} \exp\left[\frac{-y^2}{2\sigma_y^2}\right]\left[\exp\left[\frac{-(z-H)^2}{2\sigma_z^2}\right] + \exp\left[\frac{-(z+H)^2}{2\sigma_z^2}\right]\right]$$

Where *H* is the height to which the plume rises before being blown downwind. For a ground-level release along the plume centerline, Equations E-2 and E-3 reduce to the following:

(E-4)
$$\frac{CHI}{Q} = \frac{1}{2\pi u \sigma_y \sigma_z}$$

Radioactive gases released in an accident will disperse in the air according to Equations E-1 and E-3. Particles, however, have mass and will settle on the ground. Equation E-5 gives the settling velocity V_t—the terminal velocity of a particle in the indicated size range:

(E-5)
$$V_t = \frac{g\rho d^2}{18\mu}$$

---

5 The Greek letter *X* is traditionally used to represent air concentration, but is so easily confused in typescript with the 24th letter of the alphabet that it is often written phonetically ("chi").

Where:

g = gravitational acceleration

d = particle aerodynamic diameter

ρ = particle density

μ = air viscosity at ambient temperature

Equation E-6 (Wark and Warner, 1981, Chapter 5) describes the ground deposition rate:

(E-6)
$$\frac{w_p}{Q} = \frac{V_t}{2\pi u \sigma_y \sigma_z} \exp\left[\frac{-y^2}{2\sigma_y^2}\right] \exp\left[\frac{-\left(H - \frac{xV_t}{u}\right)^2}{2\sigma_z^2}\right]$$

Where w_p is the particle deposition rate. These equations are programmed in RADTRAN.

Both wind and air temperature profiles affect the dispersion of airborne material. The predominant motion of airborne material is downwind, while crosswind motion is diffusive. Light winds, stable air, and temperature inversions result in less dispersion and higher airborne and ground concentrations of radionuclides. Strong winds and turbulent air are good conditions for dispersion and result in lower airborne and deposited radionuclide concentrations and consequently result in lower radiation doses to the public, even though the plume of radioactive material may spread over a large area.

RADTRAN calculates external doses from deposited material ("groundshine") and from material that remains suspended in the air ("cloudshine"). The code also calculates internal committed doses from airborne material that is inhaled, and from material that becomes resuspended in the air. The doses reported are the sums of the groundshine, cloudshine, inhaled, and resuspended inhaled doses, unless otherwise indicated. To determine public exposure, as discussed in 10 CFR 20.1301, "Dose Limits for Individual Members of the Public," the U.S. Nuclear Regulatory Commission adds these doses to sum to a "total effective dose equivalent." RADTRAN accommodates a number of atmospheric dispersion conditions.

E.4.3 Release Fractions

Release of radionuclides into the environment from a cask depends on releases from the fuel rods into the cask and from the cask to the environment. If the cask contains canistered fuel, the cask structural and thermal analyses in Chapters 3 and 4 show that the canister does not rupture, even under the most severe accidents analyzed, so no radioactive material can exit the cask. In the present study, therefore, only the Rail-Lead cask transporting uncanistered fuel could release any radioactive material or Chalk River unidentified deposit (CRUD) as a consequence of a traffic accident. This section only considers PWR spent fuel.

E.4.3.1 Spent Fuel Radionuclides

When fuel rods are fractured in an impact, they depressurize, and the consequent overpressure sweeps fuel particles out of the cask if there is a breach in the seal. The depressurization and release of material from the rod is described very clearly by Hanson et al. (2008):

> When commercial spent nuclear fuel (CSNF) is handled in a dry environment, whether as fuel assemblies, canned, or within a container, one possible mechanism for radionuclide release is a drop accident scenario, [in which] it is possible that the cladding could fracture, and cans or containers could breach... (Sprung et al. 2000). Upon clad breach, it is expected that the rod would rapidly depressurize, releasing its fill gas (e.g., He) and fission gases (e.g., Kr, Xe) that have been released from the fuel matrix, depending on the size of the cladding defect and fuel burnup characteristics (Einziger and Beyer 2007).... It is also possible for fuel fines to be ejected as the high-pressure fill and fission gases rapidly escape through the defect.... (Hanson, et al., 2008, Section 1)

The release fractions from the rods to the cask, under the described conditions, are developed from the data in Hanson et al. (2008) for 45,000 megawatt-days per MTU spent fuel.

Hanson et al. (2008) suggest that volatile fission products, like the cesium isotopes, exhibit release behavior similar to fission gases. However, any cesium isotope would be released as the oxide or chloride and would therefore behave more like volatile compounds than like gases. Because the volatile compounds tend to migrate to the fuel rim, and Einziger (2007) recommends 3×10^{-5} as an appropriate release fraction for rim material, the present analysis uses this release fraction for volatiles, including ruthenium.

Hanson et al. (2008) describe a number of mechanical tests performed on unoxidized fuel of varying burnup. Page 4.12 of Hanson et al. (2008) summarizes release fractions from these tests for the fuel that appears to be the most appropriate. This analysis uses a release fraction of 4.8×10^{-6}, based on the information in Hanson et al. (2008), for release of fine particles from the rod to the cask. An analysis that recognizes and accommodates the uncertainty in estimating release fractions would be appropriate but is beyond the scope of this study.

Figure 7.11 in Sprung et al. (2000) presents release fractions of several compounds as functions of the available leak area. The compounds studied represent the physical and chemical groups present in spent nuclear fuel—gas, volatiles, and particulate matter. This figure served as the basis for estimating the cask-to-environment release fractions of the physical and chemical groups studied.

Table E-16 summarizes the parameters from which release fractions were developed.

Table E-16 Parameters for Determining Release Functions for the Accidents That Would Result in Release of Radioactive Material

	Cask Orientation	End	Corner	Side	Side	Side	Side	Corner
	Impact Speed (kph)	193	193	193	193	145	145	145
	Seal	metal	metal	elastomer	metal	elastomer	metal	metal
Cask to Environment Release Fraction	Gas	0.800	0.800	0.800	0.800	0.800	0.800	0.800
	Particles	0.70	0.70	0.70	0.70	0.70	0.70	0.64
	Volatiles	0.50	0.50	0.50	0.50	0.50	0.50	0.45
	Crud	0.001	0.001	0.001	0.001	0.001	0.001	0.001
Rod to Cask Release Fraction	Gas	0.12	0.12	0.12	0.12	0.12	0.12	0.12
	Particles	4.80×10^{-6}	4.80×10^{-6}	4.80×10^{-6}	4.80×10^{-6}	4.80×10^{-6}	4.80×10^{-6}	2.40×10^{-6}
	Volatiles	3.00×10^{-5}	3.00×10^{-5}	3.00×10^{-5}	3.00×10^{-5}	3.00×10^{-5}	3.00×10^{-5}	1.50×10^{-5}
	Crud	1.00	1.00	1.00	1.00	1.00	1.00	1.00
Conditional Probability for combined rod-cask-environment release		5.96×10^{-12}	3.57×10^{-11}	1.79×10^{-11}	1.79×10^{-11}	3.40×10^{-10}	3.40×10^{-10}	1.13×10^{-10}

Table E-17 shows sources of the parameter values in Table E-16. The parameter values are consistent with Sanders et al. (1992).

Table E-17 Sources of the Parameter Values in Table E-16

		Release fraction	Comment
Cask-to-Environment Release Fraction	Gas	0.800	The basis of each release fraction is the size of the gap in the seal—the leak area—provided for each combination of impact speed and orientation by Table C-1 of Appendix C. Release fractions were obtained from the graph of Figure 7.11 (p. 7-53) in Sprung et al. (2000).
	Particles	0.70	
	Particles—Corner Impact	0.64	
	Volatiles	0.50	
	Volatiles—Corner Impact	0.45	
	CRUD	0.001	This release fraction is based on Einziger and Beyer (2007) and discussed in Section E.5.4.1.
Rod-to-Cask Release Fraction	Gas	0.12	From Einziger, personal communication.
	Particles	4.80×10^{-6}	From the release fraction in Hanson et al. (2008), Table 4.10.
	Particles—Corner Impact	2.4×10^{-6}	
	Volatiles	3.00×10^{-5}	Average of values in Hanson et al. (2008), Section 4.3, p. 4.12.
	Volatiles—Corner Impact	1.5×10^{-5}	
	CRUD	1.00	CRUD is on the outside of the rod.

The release from these potential accidents is not at ground level but at about 2 meters (6.6 feet) above ground, taking into account the height of the flatcar and the diameter of the horizontally

mounted cask. The factor *H* in Equation (E-4) is the release height, 2 meters (6.6 feet) in this case. The gas flowing from the cask is warmer than ambient and the heat rate is about 660 watts per assembly[6], so that the plume of material will be lofted slightly. Results of the RADTRAN model of Equation E-4 indicate a maximum air concentration and ground deposition at about 21 meters (69 feet) downwind from the cask. Since the release is slightly elevated above ground level and the maximum air concentration at the ground and the maximum deposition are downwind from the release point,[7] based on the postulated meteorological conditions, the MEI would be located at this point. Figures 5-4a and 5-4b in Chapter 5 present a graph of the plume. Results of the RADTRAN calculation, the radiation dose (consequence) that could result if radioactive material was released in a spent fuel cask accident, are shown in Table E-18.

When the doses in Table E-18 are multiplied by the probabilities in Table E-16, the "conditional dose risks" of Table E-19 result.

Table E-18 MEI Doses (Consequences) in Sv from Accidents That Involve a Release

Cask Orientation	Impact Speed (kph)	Seal	Inhalation	Re-suspension	Cloud-shine	Ground-shine	Total
End	193	metal	1.6	0.014	8.8×10^{-5}	9.4×10^{-4}	1.6
Corner	193	metal	1.6	0.014	8.8×10^{-5}	9.4×10^{-4}	1.6
Side	193	elastomer	1.6	0.014	8.8×10^{-5}	9.4×10^{-4}	1.6
Side	193	metal	1.6	0.014	8.8×10^{-5}	9.4×10^{-4}	1.6
Side	145	elastomer	1.6	0.014	4.5×10^{-6}	3.6×10^{-5}	1.6
Side	145	metal	1.6	0.014	8.8×10^{-5}	9.4×10^{-4}	1.6
Corner	145	metal	0.73	0.0063	5.1×10^{-5}	9.2×10^{-4}	0.74

Table E-19 MEI Conditional Dose Risks in Sv from Accidents That Involve a Release

Cask Orientation	Impact Speed (kph)	Seal	Inhalation	Re-suspension	Cloud-shine	Ground-shine	Total
End	193	metal	9.5×10^{-12}	8.3×10^{-14}	5.2×10^{-16}	5.6×10^{-15}	9.5×10^{-12}
Corner	193	metal	5.7×10^{-11}	5.0×10^{-13}	3.1×10^{-15}	3.4×10^{-14}	5.7×10^{-11}
Side	193	elastomer	2.9×10^{-11}	2.5×10^{-13}	1.6×10^{-15}	1.7×10^{-14}	2.9×10^{-11}
Side	193	metal	2.9×10^{-11}	2.5×10^{-13}	1.6×10^{-15}	1.7×10^{-14}	2.9×10^{-11}
Side	145	elastomer	5.4×10^{-10}	4.8×10^{-12}	3.0×10^{-14}	3.2×10^{-13}	5.4×10^{-10}
Side	145	metal	5.4×10^{-10}	4.8×10^{-12}	3.0×10^{-14}	3.2×10^{-13}	5.4×10^{-10}
Corner	145	metal	8.3×10^{-11}	7.1×10^{-13}	5.8×10^{-15}	1.0×10^{-13}	8.3×10^{-11}

---

6 For 9-year-cooled PWR fuel from the ORIGEN analysis. 660 watts per assembly = 17,160 watts per cask = 4.1 Kcal/sec.

7 Earlier versions of RADTRAN (before RADTRAN 5.6) could not model elevated releases.

Population doses are calculated by integrating the rural, suburban, and urban population densities, respectively, over the largest plume footprint in the dispersion calculation: 1,420 km^2 (548 mi^2) for average meteorological stability (Pasquill Class D, windspeed of 4.7 meters per second (m/s) (10.5 mph). The calculation was repeated using very stable meteorology (Pasquill: stability F, windspeed 0.5 m/s (1.1 mph)), but the difference was negligible because of the relatively low elevation of the release. Collective dose risks are calculated by multiplying each population dose by the appropriate conditional probability. As an example,

Table E-20 presents the collective doses for the end impact, 193-kph (120 mph) impact speed accident.

Table E-20 Collective Inhalation and External Dose Risks for the End Impact, 193-kph Impact Speed Accident for the 16 Rail Routes Analyzed

	Collective Internal Dose Risk (person-Sv)				Collective External Dose Risk (person-Sv)			
	ORNL	DEAF SMITH	HANFORD	SKULL VALLEY	ORNL	DEAF SMITH	HANFORD	SKULL VALLEY
MAINE YANKEE								
Rural	$5.9x10^{-13}$	$7.5x10^{-13}$	$1.4x10^{-12}$	$1.0x10^{-12}$	$1.1x10^{-13}$	$1.4x10^{-13}$	$2.5x10^{-13}$	$1.9x10^{-13}$
Suburban	$7.2x10^{-12}$	$7.6x10^{-12}$	$6.4x10^{-12}$	$7.2x10^{-12}$	$1.3x10^{-12}$	$1.4x10^{-12}$	$1.2x10^{-12}$	$1.3x10^{-12}$
Urban	$2.7x10^{-11}$	$3.2x10^{-11}$	$2.5x10^{-11}$	$2.2x10^{-11}$	$4.9x10^{-12}$	$5.9x10^{-12}$	$4.4x10^{-12}$	$4.0x10^{-12}$
KEWAUNEE								
Rural	$2.7x10^{-13}$	$1.8x10^{-13}$	$2.3x10^{-13}$	$3.8x10^{-13}$	$4.9x10^{-14}$	$3.2x10^{-14}$	$4.1x10^{-14}$	$6.8x10^{-14}$
Suburban	$2.9x10^{-12}$	$1.8x10^{-12}$	$1.5x10^{-12}$	$3.0x10^{-12}$	$5.3x10^{-13}$	$3.2x10^{-13}$	$2.6x10^{-13}$	$5.5x10^{-13}$
Urban	$1.5x10^{-11}$	$1.0x10^{-11}$	$3.7x10^{-12}$	$1.1x10^{-11}$	$2.7x10^{-12}$	$1.8x10^{-12}$	$6.8x10^{-13}$	$2.0x10^{-12}$
INDIAN POINT								
Rural	$3.2x10^{-12}$	$6.3x10^{-13}$	$7.3x10^{-13}$	$8.5x10^{-13}$	$5.7x10^{-13}$	$1.1x10^{-13}$	$1.3x10^{-13}$	$1.5x10^{-13}$
Suburban	$8.6x10^{-11}$	$6.7x10^{-12}$	$6.0x10^{-12}$	$7.5x10^{-12}$	$1.6x10^{-11}$	$1.2x10^{-12}$	$1.1x10^{-12}$	$1.4x10^{-12}$
Urban	6.2E-10	$3.7x10^{-11}$	$2.8x10^{-11}$	$3.3x10^{-11}$	1.1E-10	$6.7x10^{-12}$	$5.1x10^{-12}$	$5.9x10^{-12}$
IDAHO NATIONAL LAB								
Rural	$4.7x10^{-13}$	$1.1x10^{-13}$	$7.2x10^{-14}$	$4.6x10^{-14}$	$8.5x10^{-14}$	$2.0x10^{-14}$	$1.3x10^{-14}$	$8.3x10^{-15}$
Suburban	$2.6x10^{-12}$	$1.2x10^{-12}$	$5.7x10^{-13}$	$4.1x10^{-13}$	$4.7x10^{-13}$	$2.1x10^{-13}$	$1.0x10^{-13}$	$7.4x10^{-14}$
Urban	$6.1x10^{-12}$	$2.9x10^{-12}$	$1.7x10^{-12}$	$2.0x10^{-12}$	$1.1x10^{-12}$	$5.3x10^{-13}$	$3.0x10^{-13}$	$3.6x10^{-13}$

The values in Table E-20 are calculated as in the following example. This example is for one accident scenario *i*: end impact, 193-kph (120 mph) impact speed accident.

Collective internal dose risk = (accident rate) * (route segment length) * P_{cond_i} * ($dose_{inhalation\_i}$ + $dose_{resuspension\_i}$) * $\int[(population\ density) * (plume\ footprint\ area)]$. Internal dose includes the doses from both direct inhalation and inhaled material resuspended in air. External doses include cloudshine and groundshine. The NRC cites the total effective dose equivalent, which includes both inhalation (internal) doses and external doses. The complete collective dose risk is the sum of the collective dose risks shown in Table E-20 over all accident scenarios, summed over the entire route:

Total dose risks (person-Sv) for each route = $\sum_{r,s,u} \sum_{i=1}^{7} [dose\ risk_{internal_i} + dose\ risk_{external\_i}]$.

Table E-21 shows the total dose risk for each route.

Table E-21 Total Collective Dose Risks (Person-Sv) for Each Route from an Accident Involving Release, per Shipment

	ORNL	DEAF SMITH	HANFORD	SKULL VALLEY
MAINE YANKEE	3.5×10^{-14}	4.1×10^{-14}	3.2×10^{-14}	3.0×10^{-14}
KEWAUNEE	1.8×10^{-14}	1.2×10^{-14}	5.4×10^{-15}	1.4×10^{-14}
INDIAN POINT	1.5×10^{-11}	5.9×10^{-13}	5.3×10^{-13}	1.9×10^{-13}
INL	9.4×10^{-14}	1.5×10^{-13}	4.1×10^{-14}	2.7×10^{-13}

E.5 Summary

The technical observations for the analysis of accidents are as follows:

- Event trees based on current accident statistics show that the conditional probability of a severe accident for either truck or rail is one in 100,000 or less. The probability of a fire that would damage a cask on a railcar enough to cause loss of gamma shielding or release of radioactive material is negligible.

- The analyses in Appendices C and D demonstrate that there could be no releases of radioactive material from a cask carrying canistered fuel, and the only cask that could suffer a loss of lead shielding or release of radioactive material is the Rail-Lead cask. Most accidents involving spent fuel casks—99.999999 percent—do not lead to either a release of radioactive material or a loss of lead gamma shielding.

- A dose larger than the 10 CFR 71.51 limit would be sustained only for the extra-regulatory impacts in which more than 2 percent of the lead shielding is lost and if the receptor is within 4 meters (13 feet) of the cask.

APPENDIX F

PUBLIC SUMMARY

Nuclear fission in power reactors produces a large amount of energy, which has been harnessed for the production of electricity. Fission also creates radioactive products that are contained in fuel rod pins in nuclear fuel assemblies. Therefore, spent nuclear fuel is very radioactive when first removed from a reactor, but it decays and becomes less radioactive over time. Because of this radioactivity, people understandably have some concerns when spent fuel is moved in trucks and by rail over public roads and railroads.

Thirty-five years ago, the U.S. Nuclear Regulatory Commission (NRC) responded to these concerns by estimating the radiological impact of transporting radioactive materials, including spent fuel. This analysis resulted in NUREG-0170, "Final Environmental Statement on the Transportation of Radioactive Material by Air and Other Modes," issued in 1977 (U.S. Nuclear Regulatory Commission, 1977). NUREG-0170 provided an environmental impact statement (EIS) for transportation of all types of radioactive material by road, rail, air, and water, and concluded the following:

- The average radiation dose to members of the public from routine transportation of radioactive materials is a fraction of their background dose.[1]

- The radiological risk from accidents in transporting radioactive materials is very small compared to the nonradiological risk from accidents involving large trucks or freight trains.

On the basis of this EIS, NRC regulations in 1981 were considered "adequate to protect the public against unreasonable risk from the transport of radioactive materials." However, the adequacy of these regulations continued to be questioned in part because the EIS was based on estimates of radiation dose and accident rates, for which not much data or information had been available. Among the questions not fully resolved: What constitutes "reasonable" risk and what are actual consequences should an accident happen?

The present work uses advanced models, risk assessment methods, and updated data to provide a current assessment of the risks and consequences of transporting spent nuclear fuel.

All commodities that are transported by truck or rail can be involved in accidents. Trucks and railcars carrying spent nuclear fuel transportation casks are no exception. The NRC recognizes this, and it requires that spent fuel casks be designed and built to withstand severe transportation accidents. NUREG-0170 and later studies of casks have considered accident conditions more severe than those the regulations require the cask to demonstrate their ability to withstand. A 1987 study applied actual accident statistics to projected spent fuel transportation (Fischer et al., 1987). This study, known as the "Modal Study," also recognized that accidents could be described in terms of the strains they produced in the cask (for impacts) and the increase in cask temperature (for fires). Like NUREG-0170, the 1987 study based risk estimates on models because the limited number of accidents that had occurred involving spent fuel shipments was not sufficient to support projections or predictions. The Modal Study's refinement of modeling techniques and use of accident frequency data resulted in smaller assessed risks than had been projected by NUREG-0170.

A 2000 study of two generic truck casks and two generic rail casks analyzed the cask structures and response to accidents by using computer modeling techniques (Sprung et al., 2000). The

[1] The background dose is the average dose any individual will receive over the period of a year while conducting routine, everyday activities (3.6 millisieverts).

study used semitrailer truck and rail accident statistics for general freight shipments because, even though more than 1,000 spent fuel shipments had been completed in the United States by 2000 and many thousands more had been completed safely internationally, there had been too few accidents involving spent fuel shipments to provide statistically valid accident rates.

Through a series of risk assessments, the release of radioactive material from a cask in an accident—and its subsequent dispersion—has been modeled with increasing refinement. NUREG-0170 assumed that most very severe accidents would result in release of all of the fuel particles created by the accident to the environment (the cask did not serve as a barrier to release). Although this engineering judgment overstated the release, it was nevertheless used because analytical capabilities at the time did not permit a more accurate assessment. The 2000 study analyzed the physical properties of spent fuel rods in a severe accident and revised estimates of material released to 1 percent or less of the NUREG-0170 estimates. Accordingly, risk estimates were revised downward. The 2000 study also verified that an accidental release of radioactive material could only be through the seals at the end of the cask where the lid is attached. In other words, an accident could cause seal failure, but would not breach the cask body (Sprung et al., 2000).

The present study models certified cask designs (rather than generic casks) and the commercial spent nuclear fuel that these casks are certified to transport. It evaluated two rail casks and a truck cask.

Almost all spent fuel casks are shipped without incident. However, even this routine, incident-free transportation causes radiation exposures because all loaded spent fuel casks emit some external radiation. The radiation dose rates for spent fuel shipments are measured before each shipment and must be maintained within regulatory limits. The radiation dose from this external radiation to any member of the public during routine transportation, including stops, is barely discernible compared to the public's natural background radiation. Figure F-1 illustrates a rail cask and the way in which the radiation to a member of the public is modeled. One hundred times the dose at 1 meter (3.3 feet) from the cask measured in milliSeiverts/hour (the dose measured in millirem/hour) is known as the Transport Index, which is used to represent the amount of radiation coming from the cask during routine transportation.

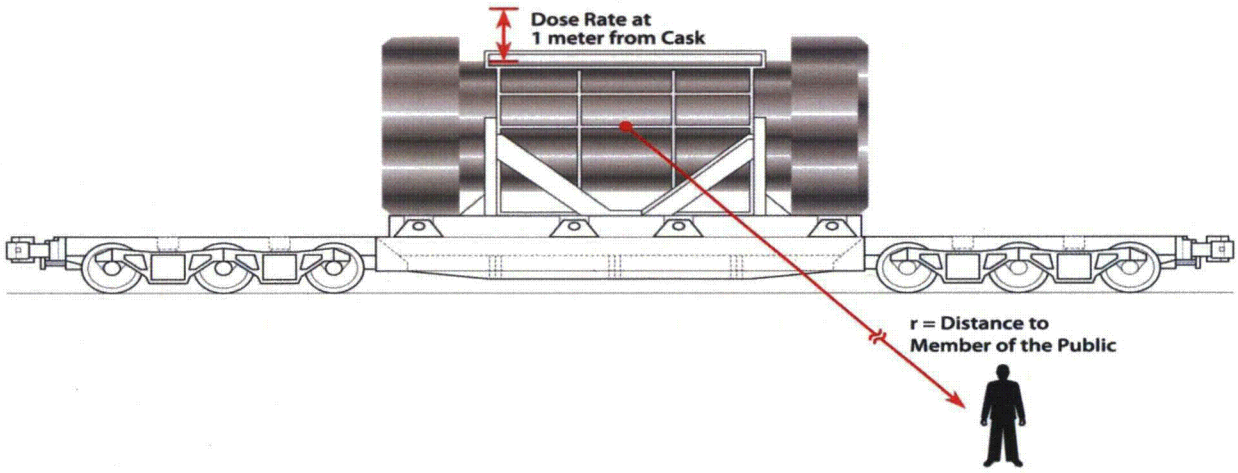

Figure F-1 Model of a spent fuel cask in routine, incident-free transportation and radiation dose to a member of the public. Relative sizes of the cask and member of the public are approximately to scale.

The external radiation from the spent fuel cask results in a very small dose to each member of the public along the route traveled by the cask. The collective dose from routine transportation is the sum of all of these doses. This study examined several example transportation routes considered to be representative of possible cross-country transport. No actual spent fuel transport has occurred, or is planned to occur, on the routes shown. Table F-1 and Figure F-2 show the possible total dose in person-sieverts (person-Sv) to all of the workers and members of the public who would be exposed to radiation along one of these routes—the truck shipment from the Maine Yankee Nuclear Power Plant to Oak Ridge National Laboratory. Table F-1 and Figure F-2 include the background radiation dose to exposed workers and members of the public during the time of the shipment.

Table F-1 Collective Dose from Routine Transport for the Truck Route from Maine Yankee Nuclear Power Plant to Oak Ridge National Laboratory (person-Sv) (1 Sv = 10^5 mrem)

Exposed Population	Rural	Suburban	Urban	Urban Rush Hour	Total
Residents near route	5.0×10^{-6}	8.9×10^{-5}	2.0×10^{-6}	4.5×10^{-7}	9.6×10^{-5}
Traffic on the route	1.3×10^{-4}	2.4×10^{-4}	5.4×10^{-5}	5.0×10^{-6}	4.6×10^{-4}
Residents near truck stops	5.6×10^{-7}	1.2×10^{-5}	*	*	1.2×10^{-5}
Truck crew	5.9×10^{-4}		7.6×10^{-5}		6.7×10^{-4}
Escort	4.7×10^{-8}		4.3×10^{-9}		5.1×10^{-8}
Inspectors (10 inspections)					1.6×10^{-3}
People at truck stops					8.6×10^{-4}
Truck stop workers					1.3×10^{-5}
	Total dose from spent fuel shipment				3.7×10^{-3}
Background					7.56

* Most truck stops are located in rural or suburban areas.

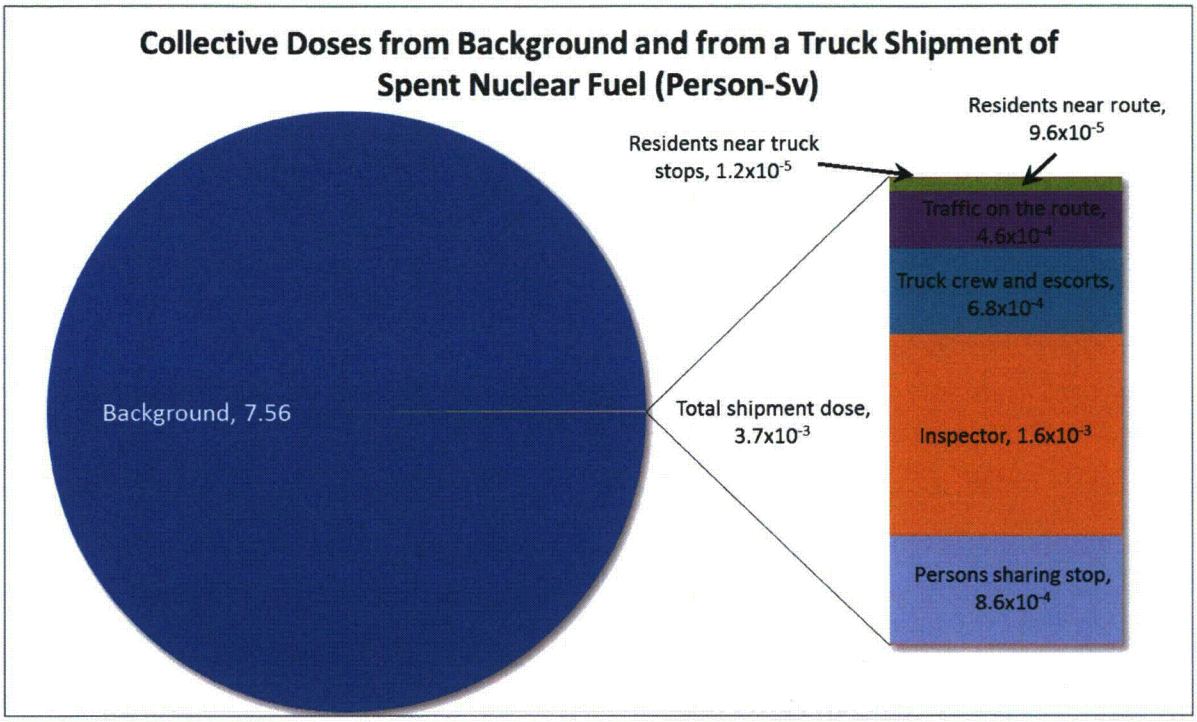

Figure F-2 Collective doses from background and from a truck shipment of spent nuclear fuel (person-Sv) (1 Sv = 10^5 mrem)

The collective doses calculated for routine transportation are higher for this study than for either NUREG/CR-6672, "Re-examination of Spent Fuel Shipment Risk Elements," (Sprung et al., 2000) or NUREG-0170 (NRC, 1977), but still a very small fraction of background dose. Figure F-3 compares the collective doses from truck transportation from the three studies. In NUREG-0170, the analysis was for a single route; in NUREG/CR-6672, the analysis was for 200 representative routes (Sprung et al., 2000); and in this study, the analysis is for 16 truck routes (as well as 16 rail routes). The collective average dose in the present study is larger than the NUREG/CR-6672 result because present populations are generally larger, particularly along rural routes; the number of vehicles sharing the highways with the spent fuel transport is now much larger (see Chapter 2); and the number and length of refueling stops is much greater. These increases were somewhat offset by the greater vehicle speeds used in the present study.

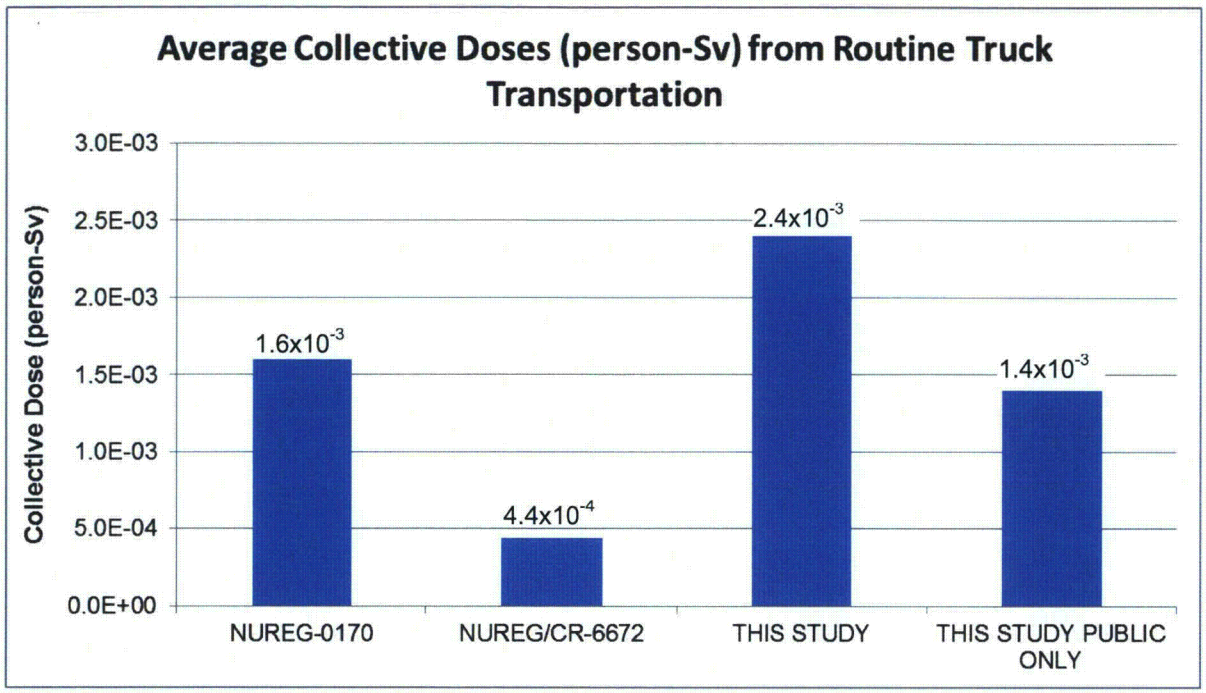

Figure F-3 Collective doses (person-Sv) from routine truck transportation

This study uses current (1991 to 2007) truck and rail accident statistics to determine the probability of an accident and the severity of that accident. Researchers performed detailed analyses to evaluate how the casks would respond to the accident scenarios. Figure F-4 shows a cask response to one impact scenario, a 97 kilometer per hour (kph) (60 mile per hour (mph)) corner impact onto a rigid target, and the resulting deformations. Almost all of the deformation is in the impact limiter, a device that is added to the cask to absorb energy, much like the bumper of a car. Similar analyses were performed for impacts at 48 kph (30 mph), 97 kph (60 mph), 145 kph (90 mph), and 193 kph (120 mph) in end-on (lid down), corner, and side-on orientations for two cask designs. These impact speeds encompass all accidents for truck and rail transportation.

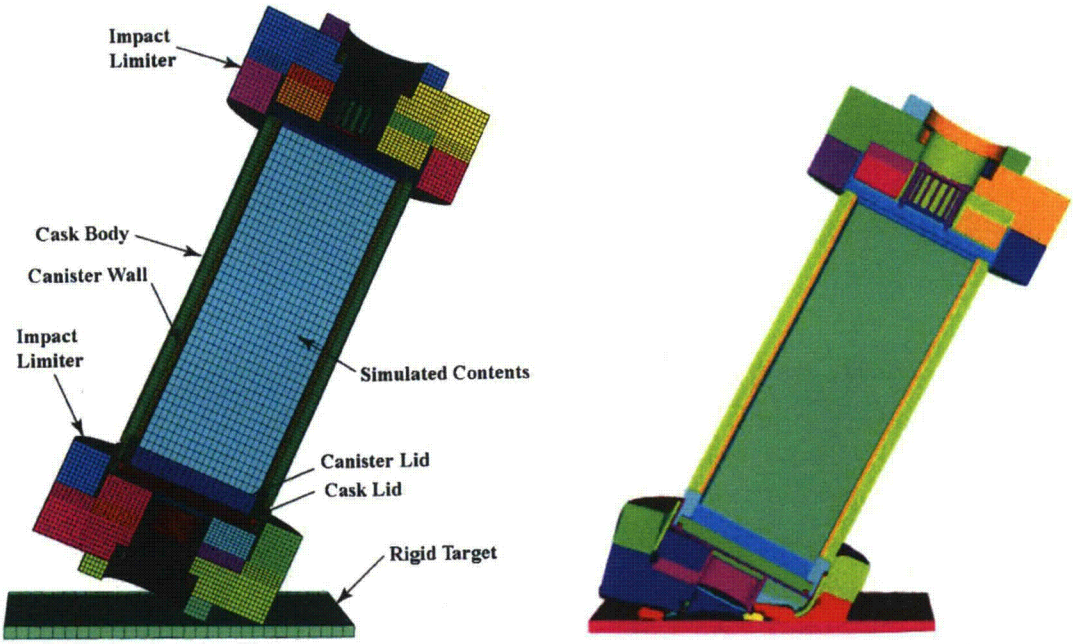

Figure F-4 Corner impact onto a rigid target at a 97-kph (60-mph) accident scenario for a spent fuel cask and the deformations produced by the impact

Figure F-5 shows one fire scenario, a 3-hour engulfing fire, and the resulting temperature distribution in the cask. Additional simulations were performed with the fire offset from the cask. These fires include all fire-related accidents in rail transportation. The longest duration for an engulfing fire during truck transportation is 1 hour because of the amount of fuel that is carried onboard a tanker truck.

Detailed impact simulations were performed for two spent fuel casks intended for transportation by railroad, the NAC-STC and the HI-STAR 100. In addition, the results for a third cask, the GA-4, which is intended for transportation by truck, were inferred from earlier analyses. Detailed fire simulations were performed for all three casks.

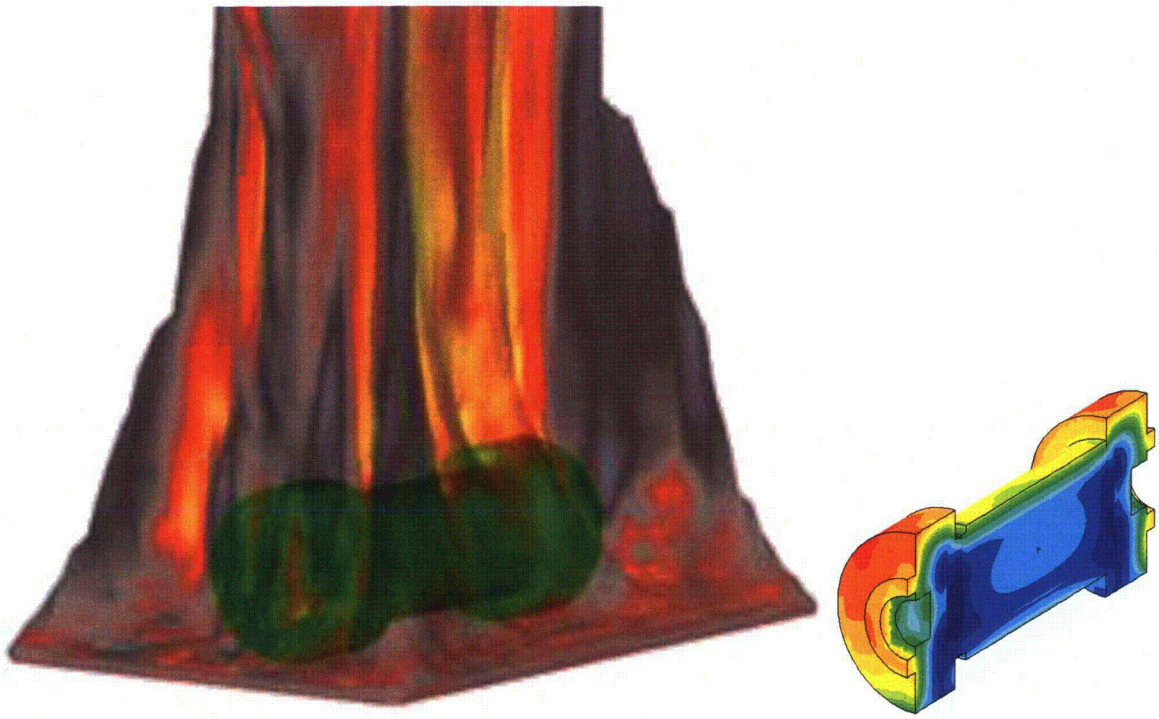

Figure F-5 Engulfing fire scenario and the temperature contours in the rail cask following a 3-hour fire duration. The transparency of the flames has been increased so the cask can be seen; in the actual fire simulation, and in a real fire, the flames are opaque.

The impact and thermal analysis results indicate that no accident involving the truck transportation cask would result in the release of radioactive material or reduction in the effectiveness of the gamma shielding. The only radiological consequence of an accident would be exposure to external radiation from the cask because of the long-duration stop associated with the accident. The stop needs to be long enough for responders to clear the accident scene and to arrange for shipment to resume. During this stop emergency, responders could be fairly close to the cask. Because there is no loss in effectiveness of the gamma shielding, the radiation dose to these responders would be a small fraction of the allowed occupational dose.

For rail transport of spent fuel that is in an inner welded canister, this study shows that there would be no release of radioactive material. For casks using lead gamma shielding, the most severe accidents evaluated led to a reduction in the effectiveness of that shielding, which results in an elevated external radiation level. In addition, for rail transport of spent fuel that is not in an inner welded canister, some radioactive material is released following exceptionally severe and improbable accidents.

The calculated collective dose risk from accidents has decreased with each successive risk assessment. Figure F-6 compares the average collective doses from releases and loss of lead shielding from the three studies (NUREG-0170 did not calculate loss of lead shielding). This study also considered accident doses from a source that was not analyzed in the prior studies—the dose that results from accidents in which there is neither release nor loss of lead shielding, but there is increased exposure to a cask that is stopped for an extended period of time. Figure F-7 shows the average collective doses for this scenario for the three casks studied. This

scenario is important because more than 99.999 percent of all accident scenarios do not lead to either release of radioactive material or loss of shielding.

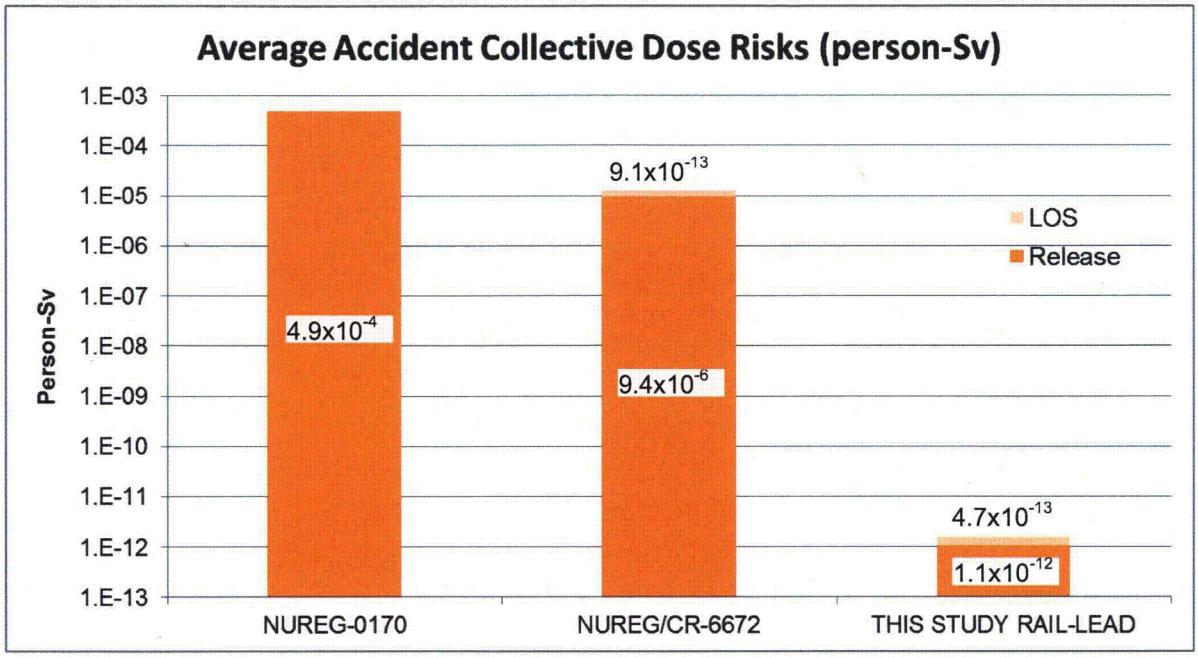

Figure F-6 Accident collective dose risks from release and loss-of-shielding accidents. The loss-of-shielding bars are not to scale.

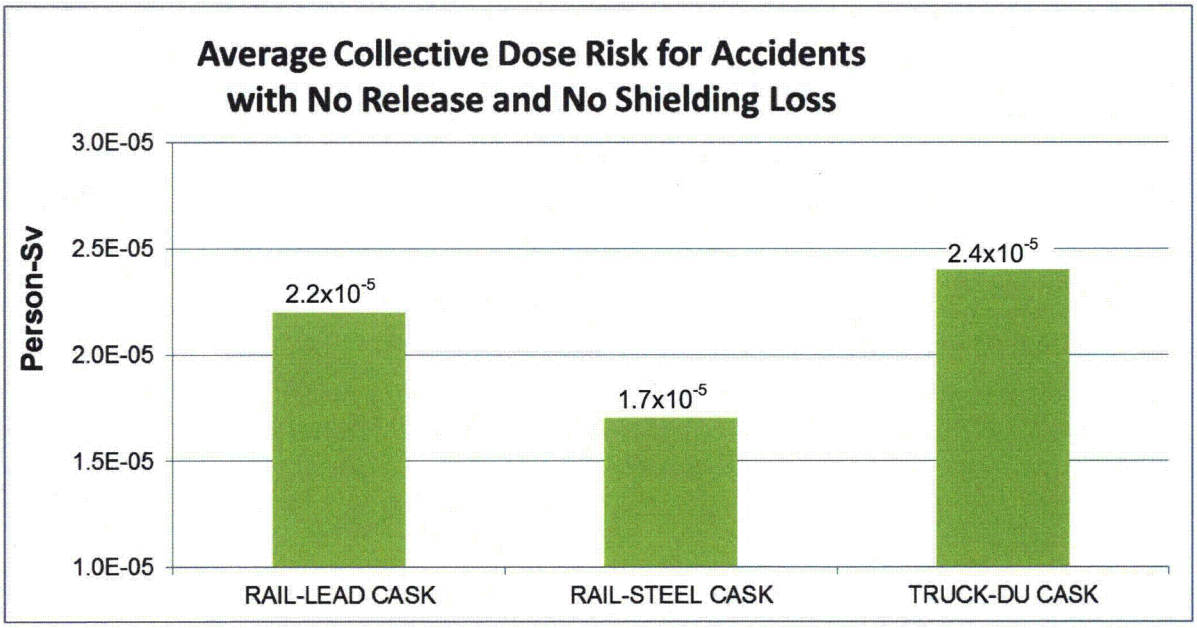

Figure F-7 Average collective dose from accidents that have no impact on the cargo

A final point of comparison between the studies is the maximum consequence of an accident. For NUREG-0170, this was about 110 person-Sv; for NUREG/CR-6672, it was about 9,000 person-Sv; and for this study, it is 2.2 person-Sv. The reduction in consequence is the result of using the actual spent fuel being shipped, a smaller release fraction, and improvements in the RADTRAN model. This study estimated the effects of an accident on the maximally exposed individual (a theoretical person located at the point of highest concentration of potentially released radioactive material for 10 hours). The estimate for such an individual is calculated to be a dose of 1.6 Sv, about the same dose that is received in a single radiotherapy session by a cancer patient.

As noted above, the purpose of this analysis was to reproduce (and, in some cases, extend) risk analyses previously considered in NUREG-0170, the Modal Study, and NUREG/CR-6672 using updated models and methods. The study reached the following findings:

- The collective dose risks from routine transportation are vanishingly small. These doses are about four to five orders of magnitude less than collective background radiation doses.

- The routes selected for this study adequately represent the routes for spent nuclear fuel transport, and there was relatively little variation in the risks per kilometer over these routes.

- Radioactive material would not be released in an accident if the fuel is contained in an inner welded canister inside the cask.

- Only rail casks without inner welded canisters would release radioactive material, and only then in exceptionally severe accidents.

- If there were an accident during a spent fuel shipment, there is only about a one in a billion chance the accident would result in a release of radioactive material.

- If there were a release of radioactive material in a spent fuel shipment accident, the dose to the maximally exposed individual would be less than 2 Sv (200 rem), and would be neither acute nor lethal.

- The collective dose risks for the two types of extraregulatory accidents (accidents involving a release of radioactive material and loss of lead shielding) are negligible compared to the risk from a no-release, no-loss-of-shielding accident.

- The risk of loss of shielding from a fire is negligible.

- None of the fire accidents investigated in this study resulted in a release of radioactive material.

Based on these findings, this study reconfirms that radiological impacts from spent fuel transportation conducted in compliance with NRC regulations are low. In fact, this study's radiological impact estimates are generally less than the already low estimates reported in earlier studies. Accordingly, with respect to spent fuel transportation, this study reconfirms the previous NRC conclusion that the regulations for transportation of radioactive material are adequate to protect the public against unreasonable risk.

BIBLIOGRAPHY

Adams, G. and Mintz, T., "Analysis of Severe Railway Accidents Involving Long Duration Fires," NUREG/CR-7035, Center for Nuclear Waste Regulatory Analysis, San Antonio, TX, February 2011.

Adams, G., Mintz, T., Necsoiu, M., and Mancillas, J., "Analysis of Severe Railway Accidents Involving Long Duration Fires," NUREG/CR-7034, Center for Nuclear Waste Regulatory Analysis, San Antonio, TX, February 2011.

Adkins, H.E., Cuta, J.M., Koeppel, B.J., Guzman, A.D., and Bajwa, C.S., "Spent Fuel Transportation Package Response to the Tunnel Fire Scenario," NUREG/CR-6886, Revision 2, PNNL-15313, Pacific Northwest National Laboratory, Richland, WA, November 2006.

Adkins, H.E., Koeppel, B.J., Cuta, J.M., Guzman, A.D., and Bajwa, C.S., "Spent Fuel Transportation Package Response to the Caldecott Tunnel Fire Scenario," NUREG/CR-6894, Revision 1, PNNL-15346, Pacific Northwest National Laboratory, Richland, WA, January 2007.

American Society for Testing Materials, "Standard Practice for Thermal Qualification of Type B Packages for Radioactive Material," E2230-08, ASTM International, 2008.

Ammerman, D.J. and Gwinn, K.W., "Collapse of the Cypress Street Viaduct—Effect on a Postulated Spent Fuel Truck Cask," *Proceedings of the 45th Institute of Nuclear Materials Management Annual Meeting*, Orlando, FL, August 2004.

Ammerman, D.J., Stevens, D., and Barsotti, M., "Numerical Analyses of Locomotive Impacts on a Spent Fuel Truck Cask and Trailer," Proceedings of the American Society of Mechanical Engineers Pressure Vessels and Piping Conference, Denver, CO, July 2005.

Are, N., Greiner, M. and Suo-Anttila, A., "Benchmark of a Fast-Running Computational Tool for Analysis of Massive Radioactive Material Packages in Fire Environments," *Journal of Pressure Vessel Technology*, American Society of Mechanical Engineers, 127:508–514, November 2005.

Bajwa, C.S., Easton, E.P., Adkins, H., Cuta, J. Klymyshyn, N., and Suffield, S., "Effects of the MacArthur Maze Fire and Roadway Collapse on a Spent Nuclear Fuel Transportation Package," *Proceedings of the 2011 Waste Management Conference*, Phoenix, AZ, February 27–March 3, 2011.

Blandford, R.K., Morton, D.K., Snow, S.D., and Rahl, T.E., "Tensile Stress-Strain Results for 304L and 316L Stainless Steel Plate at Temperature," PVP2007-26096, *Proceedings of the American Society of Mechanical Engineers Pressure Vessels and Piping Conference*, San Antonio, TX, July 2007.

Bonzon, L.L. and Schamaun, J.T., "Container Damage Correlation with Impact Velocity and Target Hardness," IAEA-SR-10/21, "Transport Packaging for Radioactive Materials," International Atomic Energy Agency, Vienna, Austria, January 1976.

Committee on Transportation of Radioactive Waste, National Research Council, "Going the Distance? The Safe Transport of Spent Nuclear Fuel and High-Level Radioactive Waste in the United States," National Academies Press, Washington, DC, 2006.

Croff, A.G., "ORIGEN2—A Revised and Updated Version of the Oak Ridge Isotope Generation and Depletion Code," ORNL-5621, Oak Ridge National Laboratory, Oak Ridge, TN, July 1980.

del Valle, M.A., "Benchmark and Sensitivity Study of the Container Analysis Fire Environment (CAFE) Computer Code Using a Rail-Cask-Size Pipe Calorimeter in Large-Scale Pool Fires," MAI 47/03, University of Nevada, Reno, NV, 2008.

del Valle, M.A., Kramer, M.A., Lopez, C., Suo-Anttila, A., and Greiner, M., "Temperature Response of a Rail-Cask-Size Pipe Calorimeter in Large-Scale Pool Fires," *Proceedings of the 15th International Symposium on the Packaging and Transportation of Radioactive Materials*, Miami, FL, October 2007.

Dennis, M.L., Osborn, D.O., Weiner, R.F., and Heames, T.J., "Verification and Validation of RADTRAN 6.0," SAND2008-4556, Sandia National Laboratories, Albuquerque, NM, 2008.

Dennis, M.L., Weiner, R.F., Osborn, D.M., and Heames, T.J., "Dose Estimates in a Loss of Lead Shielding Truck Accident," SAND2009-5107, Sandia National Laboratories, Albuquerque, NM, August 2009.

Einziger, R.E., "Source Term for Spent Fuel Transportation and Storage Cask Evaluation," *Proceedings of the 15th International Symposium on the Packaging and Transportation of Radioactive Materials*, Miami, FL, October 2007.

Einziger, R.E. and Beyer, C.E., "Characteristics and Behaviour of High Burnup Fuel that May Affect the Containment Source Terms for Cask Accidents," *Nuclear Technology*, 159(2): 134–146, 2007.

Federal Register, Vol. 46, p. 21629, April 13, 1981.

Figueroa, V.G. and Lopez, C., "8ft Diameter Calorimeter Fire Test Series," SAND2011-8349, Sandia National Laboratories, Albuquerque, NM, 2012.

Fischer, L.E., Chou, C.K., Gerhard, M.A., Kimura, C.Y., Martin, R.W., Mensing, R.W., Mount, M.E., and Witte, M.C., "Shipping Container Response to Severe Highway and Railway Accident Conditions," NUREG/CR-4829, Lawrence Livermore National Laboratory, Livermore, CA, February 1987.

General Atomics, "GA-4 Legal Weight Truck Spent Fuel Shipping Cask," Safety Analysis Report for Packaging, General Atomics Project 4439, San Diego, CA, 1998.

Gonzales, A., "Target Effects on Package Response: An Experimental and Analytical Evaluation," SAND-86-2275, Sandia National Laboratories, Albuquerque, NM, May 1987.

Greiner, M., del Valle, M., Lopez, C., Figueroa, V., and Abu-Irshaid, E., "Thermal Measurements of a Rail-Cask-Size Pipe-Calorimeter in Jet Fuel Fires, American Society of Mechanical Engineers, 2009 Heat Transfer Summer Conference, HT2009-88520, San Francisco, CA, July 2009.

Griego, N.R., Smith, J.D., and Neuhauser, K.S., "Investigation of RADTRAN Stop Model Input Parameters for Truck Stops," SAND96-0714C, Sandia National Laboratories, Albuquerque, NM, March 1996.

Haire, M.J. and Swaney, P.M., "Cask Size and Weight Reduction Through the Use of DUO_2-Steel Cermet Material," 2005 Waste Management Symposium, Tucson, AZ, 2005.

Hanson, B.D., Daniel, R.D., Casella, A.M., Wittman, R.S., Wu, W., MacFarlan, P.J., and Shimskey, R.W. "Fuel-in-Air FY07 Summary Report," Revision 1, PNNL-17275, Pacific Northwest National Laboratory, Richland, WA, 2008.

Hibbit, Karlsson and Sorensen, Inc., "ABAQUS Standard User's Manual, Version 5.8, Pawtucket, RI, 1998.

Hinnerichs, T.D., Carne, T.G., Lu, W.Y., Stasiunas, E.C., Neilsen, M.K., Scherzinger, W. and Rogillio, B.R., "Characterization of Aluminum Honeycomb and Experimentation for Model Development and Validation," SAND2006-4455, Sandia National Laboratories, Albuquerque, NM, August 2006.

Hoffman, E.L. and Attaway, S.W., "Structural Analysis of the Source Term Transportation Cask," SAND91-1543, Sandia National Laboratories, Albuquerque, NM, 1991.

Holtec International. "Safety Analysis Report for the Holtec International Storage, Transport, and Repository Cask System (HI-STAR 100 Cask System)", Holtec Report HI-951251, Rev. 9, 2000.

Husek, H.J., "Structural Alloys Handbook," Metals and Ceramics Information Center, Battelle Columbus Laboratories, Columbus, OH, 1986.

Incropera, F.P. and Dewitt, D.P., *Fundamentals of Heat and Mass Transfer*, John Wiley & Sons, New York, NY, 1996.

Johnson, P.E. and Michelhaugh, R.D., "Transportation Routing Analysis Geographic Information System (TRAGIS) User Manual," ORNL/NTRC-006, Oak Ridge National Laboratory, Oak Ridge, TN, June 2003.

Kalan, R.J., Clutz, C.J.R., and Ammerman, D.J., "Analysis of a 17x17 Pressurized Water Reactor (PWR) Fuel Assembly," Letter report to the U.S. Department of Energy, August 2005.

Kelley, K.K., "Enthalpy Plots," DWG K38745, In *Contributions to the Data on Theoretical Metallurgy*, Bureau of Mines Bulletin 584, 1960.

Klamerus, E.W., Bohn, M.P., Wesley, D.A., and Krishnaswamy, C.N., "Containment Performance of Prototypical Reactor Containment Subjected to Severe Accident

Conditions," NUREG/CR-6433, U.S. Nuclear Regulatory Commission, Washington, DC, 1996.

Koski, J.R., "Measurement of Temperature Distributions in Large Pool Fires with the Use of Directional Flame Thermometers," PVP-Vol. 408, *Proceedings of the American Society of Mechanical Engineers Pressure Vessels and Piping Conference*, Seattle, WA, July 2000.

Kramer, M.A., del Valle, M., and Greiner, M., "Measurement and Uncertainty of Heat Flux to a Rail-Cask Size Pipe Calorimeter in a Pool Fire," PVP2008-61600, *Proceedings of the American Society of Mechanical Engineers Pressure Vessels and Piping Conference*, Chicago, IL, July 2008.

Livermore Software Technology Corporation, "LS-DYNA User's Manual," Livermore, CA, 1999.

Lopez, A.R., Gritzo, L.A., and Sherman, M.P., "Risk Assessment Compatible Fire Models," SAND-97-1562, Sandia National Laboratories, Albuquerque, NM, July 1998.

Lopez, C., Koski, J., and Suo-Anttila, A., "Development and Use of the CAFE-3D Code for Analysis of Radioactive Material Packages in Fire Environments," Institute of Nuclear Materials Management Conference, Phoenix, AZ, 2003.

Lorenz, R.A., Collins, J.L., Malinauskas, A.P., Kirkland, O.L., and Towns, R.L., "Fission Product Release from Highly Irradiated LWR Fuel," NUREG/CR-0722, Oak Ridge National Laboratory, Oak Ridge, TN, February 1980.

Lorenz, R.A., Collins, J.L., and Manning, S.R., "Fission Product Release from Simulated LWR Fuel," NUREG/CR-0274, Oak Ridge National Laboratory, Oak Ridge, TN, July 1978.

McAdams, W.H., *Heat Transmission*, 3rd Ed., McGraw-Hill, Inc., New York, NY, 1954.

Mills, G.S., Sprung, J.L., and Osborn, D.M., "Tractor/Trailer Accident Statistics," SAND2006-7723, Sandia National Laboratories, Albuquerque, NM, 2006.

MSC.Software Corporation, "MSC PATRAN/Thermal," Version 2008r2, MSC.Software Corporation, Santa Ana, CA, 2008.

Nakos, J.T., "Uncertainty Analysis of Steady State Incident Heat Flux Measurements in Hydrocarbon Fuel Fires," SAND2005-7144, Sandia National Laboratories, Albuquerque, NM, 2005.

Neuhauser, K.S., Kanipe, F.L., and Weiner, R.F., "RADTRAN 5, Technical Manual," Sandia National Laboratories, Albuquerque, NM, 2000.

Nicolette, V.F. and Larson, D.W., "Influence Of Large, Cold Objects On Engulfing Fire Environments," SAND89-2175C, Sandia National Laboratories, Albuquerque, NM, 1989

NAC International, "Safety Analysis Report for the NAC Storage Transport Cask," NRC Docket 71-9235, Atlanta, GA, 2004.

O'Donnell, B., Kearfott, K., James, S., and Weiner, R.F., "Calculating External Dose Increase from Partial Loss of Lead Shielding in a Spent Fuel Cask," Institute for Nuclear Materials Management's Annual Meeting, Orlando, FL, 2004.

Perry, J.H., *Chemical Engineering Handbook*, 4th Ed., McGraw-Hill, New York, NY, 1963.

Petersen, H., "The Properties of Helium," Riso Report No. 224, Danish Atomic Energy Commission, 1970.

Pierce, J.D., Gronewald, P.J., Mould, J., and Oneto, R., "Radiant Heat Test of Perforated Metal Air Transportable Package," SAND2003-2750, Sandia National Laboratories, Albuquerque, NM, 2003.

Pierron, O.N., Koss, D.A., and Motta, A.T., "Tensile Specimen Geometry and Constitutive Behavior of Zircaloy-4," *Journal of Nuclear Materials*, 312:257–261, 2003.

Quintiere, J.G., *Principles of Fire Behavior*, Delmar Publishers, Albany, NY, 1998.

Ross, S.S., Weiner, R.F., Best, R.E., Maheras, S., and McSweeney, T., "Transportation Health and Safety Calculation/Analysis Documentation in Support of the Final EIS for the Yucca Mountain Repository," CAL-HSS-ND-000003, U.S. Department of Energy, Office of Civilian Radioactive Waste Management, Las Vegas, NV, 2002.

Sanders, T.L., Seager, K.D., Rashid, Y.R., Barrett, P.R., Malinauskas, A.P., Einziger, R.E., Jordan, H., Duffey, T.A., Sutherland, S.H., and Reardon, P.C., "A Method for Determining the Spent-Fuel Contribution to Transport Cask Containment Requirements," SAND90-2406, Sandia National Laboratories, Albuquerque, NM, 1992.

Sandoval, R.P., Einziger, R.E., Jordan, H., Malinauskas, A.P., and Mings, W.J., "Estimate of CRUD Contribution to Shipping Cask Containment Requirements," SAND88-1358. Sandia National Laboratories, Albuquerque, NM, 1988.

Schorsch, R.H., "Engineering properties of selected metals," in *Modern Plastics Encyclopedia Issue*, McGraw-Hill, New York, 1966.

Shleien, B., Slaback, L.S., and Birky, B.K., *Handbook of Health Physics and Radiological Health*, Third Ed., Williams and Wilkins, Baltimore, MD, 1998.

SIERRA Solid Mechanics Team, "Presto 4.14 User's Guide," SAND2009-7401, Sandia National Laboratories, Albuquerque, NM, November 2009.

Society of Fire Protection Engineers (SFPE), "The SFPE Handbook of Fire Protection Engineering," 3rd Ed., National Fire Protection Association, Quincy, MA, 2002.

Soo-Haeng, C., Jae-Bum, D., Seung-Gy, R., and Chun-Ho, D., "Fabrication and Characteristics of Resin-Type Neutron Shielding Materials for Spent Fuel Shipping Cask," *Journal of Industrial and Engineering Chemistry*, 7(3):597–604, June 1996.

Sprung, J.L., Ammerman, D.J., Breivik, N.L., Dukart, R.J., Kanipe, F.L., Koski, J.A., Mills, G.S., Neuhaiuser, K.S., Radloff, H.D., Weiner, R.F., and Yoshimura, H.R., "Re-Examination

of Spent Fuel Risk Estimates," NUREG/CR-6672, Sandia National Laboratories, Albuquerque, NM, 2000.

Stabin, M.G., "Doses from Medical Radiation Sources," Health Physics Society Topical Articles, 2009.

Steinman, R.L., Weiner, R.F., and Kearfott, K., "Comparison of Transient Dose Model Predictions and Experimental Measurements," *Health Physics,* 83:504 et seq., 2002.

Suo-Anttilla, A., Lopez, C., and Khalil, I., "User Manual for CAFE-3D: A Computational Fluid Dynamics Fire Code," SAND2005-1469, Sandia National Laboratories, Albuquerque, NM, 2005.

Taylor, J.M. and Daniel, S.L., "RADTRAN: A Computer Code to Analyze Transportation of Radioactive Material," SAND76-0243, Sandia National Laboratories, Albuquerque, NM, 1977.

Thermophysical Properties Research Laboratory Inc., "Thermophysical Properties of Kaowool, Honeycomb, Foam and Cork," Report No. 2649, August 2001.

Tubiana, M. and Aurengo, A., "Dose-Effect Relationship and Estimation of the Carcinogenic Effects of Low Doses of Ionizing Radiation," Joint Report of the Académie des Sciences (Paris) and the Académie Nationale de Médecine, *International Journal of Low Radiation*, 2:1–19, 2005.

Turner, D.B., *Workbook of Atmospheric Dispersion Estimates*, Lewis Publishers, New York, NY, 1994.

U.S. Census Bureau, "The 2008 Statistical Abstract," 2008.

U.S. Code of Federal Regulations, "Standards for Protection against Radiation," Part 20, Chapter I, Title 10, "Energy."

U.S. Code of Federal Regulations, "Packaging and Transportation of Radioactive Material," Part 71, Chapter 1, Title 10, "Energy."

U.S. Code of Federal Regulations, "Shippers—General Requirements for Shipments and Packagings," Part 173, Subchapter C, Title 49, "Transportation."

U.S. Code of Federal Regulations, "Carriage by Rail," Part 174, Subchapter C, Title 49, "Transportation."

U.S. Code of Federal Regulations, "Carriage by Aircraft," Part 175, Subchapter C, Title 49, "Transportation."

U.S. Code of Federal Regulations, "Carriage by Vessel," Part 176, Subchapter C, Title 49, "Transportation."

U.S. Code of Federal Regulations, "Carriage by Public Highway," Part 177, Subchapter C, Title 49, "Transportation."

U.S. Code of Federal Regulations, "Specifications for Packagings," Part 178, "Specifications for Tank Cars," Part 179, Subchapter C, Title 49, "Transportation."

U.S. Department of Defense, "Aerospace Structural Metals Handbook," Code 4103, 1993.

U.S. Department of Energy, "Final Environmental Impact Statement for a Geologic Repository for the Disposal of Spent Nuclear Fuel and High-Level Radioactive Waste at Yucca Mountain, Nye County, Nevada," DOE/EIS-0250F, Washington, DC, Chapter 6 and Appendix J, 2002.

U.S. Department of Energy, "Environmental Assessment Yucca Mountain Site, Nevada Research and Development Area, Nevada," DOE/RW-0073, Office of Civilian Radioactive Waste Management, Washington, DC, 1986.

U.S. Department of Transportation, "Maximum Posted Speed Limits by Type of Road," Table 2-9, State Transportation Statistics, Bureau of Transportation Statistics Research and Innovative Technology Administration, Washington, DC, 2004(a).

U.S. Department of Transportation, "Rail Freight Average Speeds, Revenue Ton-Miles, and Terminal Dwell Times," Table D-4, Transportation Statistics Annual Report, Bureau of Transportation Statistics Research and Innovative Technology Administration, Washington, DC, 2006.

U.S. Department of Transportation, "State Transportation Statistics 2004," Bureau of Transportation Statistics, Research, and Innovative Technology Administration, Washington, DC, 2005.

U.S. Department of Transportation, "Traffic Safety Facts 2007," Tables 1-32, 2-03, 2-04, 2-09, 2-28, and 2-37, Bureau of Transportation Statistics, Research, and Innovative Technology Administration, Washington, DC, 2007.

U.S. Department of Transportation, "National Transportation Statistics 2008," Bureau of Transportation Statistics, Research, and Innovative Technology Administration, Washington, DC, 2008.

U.S. Department of Transportation, "Commodity Flow Survey: Shipment Characteristics by Mode of Transportation for the U.S.," Table 1, Bureau of Transportation Statistics, Research, and Innovative Technology Administration, Washington, DC, 2009.

U.S. Nuclear Regulatory Commission, "Reactor Safety Study," WASH-1400, Washington, DC, 1975.

U.S. Nuclear Regulatory Commission, "Final Environmental Statement on the Transportation of Radioactive Material by Air and Other Modes," NUREG-0170, Washington, DC, 1977.

U.S. Nuclear Regulatory Commission, "Safety Analysis Report for the Plutonium Air Transportable Package, Model PAT-1," NUREG-0361, Washington, DC, 1978.

U.S. Nuclear Regulatory Commission, "List of Approved Spent Fuel Storage Casks: NAC-UMS Addition (10 CFR Part 71)," *Federal Register,* Vol. 65, No. 203, October 19, 2000, pp. 62581-62599.

U.S. Nuclear Regulatory Commission, "Safety of Spent Fuel Transportation," NUREG/BR-0292, Washington, DC, 2003(a).

U.S. Nuclear Regulatory Commission, "United States Nuclear Regulatory Commission Package Performance Study Test Protocols," NUREG-1768, Washington, DC, 2003(b).

U.S. Nuclear Regulatory Commission, "State of the Art Reactor Consequence Analysis—Reporting Offsite Health Consequences," SECY-08-0029, and "Commission Voting Record on SECY-08-2009," Washington, DC, 2008.

Volpe Center, "Spent Nuclear Fuel Transportation Risk," Draft Report, Volpe National Transportation Systems Center, Cambridge, MA, 2006.

Waddoups, I.G., "Air Drop Test of Shielded Radioactive Material Containers," SAND75-0276, Sandia National Laboratories, Albuquerque, NM, 1975.

Wark, K. and Warner, C.F., *Air Pollution: Its Origin and Control*, Harper and Row, New York, NY, 1981.

Weast, R.C., *Handbook of Chemistry and Physics*, 47th Ed., The Chemical Rubber Company, Cleveland, Ohio, 1966.

Weiner, R.F. and Neuhauser, K.S., "Near-Field Radiation Doses from Spent Fuel Transportation," International High-Level Waste Management Conference, Las Vegas, NV, 1992.

Weiner, R.F., Dennis, M.L., Hinojosa, D., Heames, T.J., Penisten, J.J., Marincel, M.K., and Osborn, D.M., "RadCat 3.0 User Guide," SAND2009-5129P, Sandia National Laboratories, Albuquerque, NM, 2009.

Wellman, G,W. and Salzbrenner, R., "Quasistatic Modeling and Testing of Exclusion Region Barrier Mock-Ups," SAND92-0024, Sandia National Laboratories, Albuquerque, NM, 1992.

Wooden, D.G., "Railroad Transportation of Spent Nuclear Fuel," SAND86-7083, Sandia National Laboratories, Albuquerque, NM, 1986.

Yafei, S., Yongjun, T., Jing, S., and Dongjie, N., "Effect of Temperature and Composition on Thermal Properties of Carbon Steel," Chinese Control and Decision Conference, Guilin, China, 2009.